



UNIVERSITÉ
DE LORRAINE



Universität Stuttgart



École doctorale EMMA
College Sciences et Technologies

Institut für Grenzflächenverfahrenstechnik
und Plasmatechnologie

Experimental and numerical study of turbulence in fusion plasmas using reflectometry synthetic diagnostics

Made by

Georgiy Zadvitskiy

in IJL, Université de Lorraine and IGVP, University of Stuttgart, and CEA,
Cadarache.

A thesis submitted for the degree of
Doctor rerum naturalium (Dr. rer. nat.)

IJL - Université de Lorraine, IGVP - University of Stuttgart
2018

Experimental and numerical study of turbulence in fusion plasmas using reflectometry synthetic diagnostics

Von der Fakultät Energie-, Verfahrens- und Biotechnik der Universität Stuttgart
zur Erlangung der Würde eines Doktors der
Naturwissenschaften (Dr. rer. nat) genehmigte Abhandlung

Vorgelegt von

Georgiy Zadvitskiy

aus Almaty

Hauptberichter: apl. Prof. Dr. rer. nat. Günter Tovar
Mitberichter Prof. Dr. Ulrich Stroth

Tag der mündlichen Prüfung: 07.06.2018

Institut für Grenzflächenverfahrenstechnik und Plasmatechnologie
der Universität Stuttgart
2018

Declaration

I declare that this thesis was composed by myself and that the work contained therein is my own, except where explicitly stated otherwise in the text.

(Georgiy Zadvitskiy)

*To my daughter Olivia, who was born during second year of
my Ph.D. studies*

Abstract

Anomalous energy and particle transport is closely related to micro-turbulence. Therefore plasma turbulence studies are essential for successful operation of magnetic confinement fusion devices. This thesis deals with the development of interpretative models for Ultra-Fast Swept Reflectometry (USFR), a diagnostic used for the measurement of turbulence radial wave-number spectra in fusion devices. While the interpretation of reflectometry data is quite straightforward for small levels of turbulence, it becomes much trickier for larger levels as the reflectometer answer is no longer linear with the turbulence level. It has been shown for instance that resonances due to probing field trapping can appear in turbulent plasma and produce jumps of the signal phase. In the plasma edge region the turbulence level is usually high and can lead to a non-linear regime of the reflectometer response. The loss of probing beam coherency and beam widening when the probing beam crosses the edge turbulence layer can affect USFR core measurements. Edge turbulence with a long correlation length leads to small beam widening and strong distortion of the probing wave phase. However backscattering effects from turbulence with short correlation lengths are also able to cause reflectometer signal change.

To study turbulence wave-number spectra as well as reflectometer signal phase variations, signal amplitude variations can be analyzed. Unlike signal phase variation, amplitude does not suffer from resonant jumps, and can give more clear qualitative evaluation of turbulence structure. In the case when the turbulence amplitude peaked in the edge region, it can be detected as spectral peak near local Bragg resonance wave-number. USFR with a set of receiving antennas arranged poloidally was proposed to obtain more information on the edge turbulence properties. A displacement of the spectral peak appears when the receiving antenna is misaligned with the emitting one. Peak displacement measurements could provide additional information on probing beam shaping and turbulence properties and help in coherent mode observation as well.

A 2D full wave code was applied as a synthetic diagnostic to Gysela gyro-kinetic code data to study Tore-Supra tokamak core turbulence. Radial correlation lengths computed from the amplitude of multi-channel fixed frequency reflectometry signals

have shown good agreement with the turbulence correlation length directly computed from the simulation. The synthetic diagnostic was then applied to analyse the correlation length and wave-number spectra obtained by USFR in the ASDEX-Upgrade tokamak. A comparison between 1D and 2D results have shown different behaviour. However correlation lengths measured with UFSR signals are in the same order with turbulence ones.

Contents

| | |
|--|-----------|
| List of used variables | 10 |
| 1 Introduction | 17 |
| 1.1 Sources of the energy | 18 |
| 1.2 Nuclear fusion | 20 |
| 1.2.1 Introduction to nuclear fusion | 20 |
| 1.2.2 Ignition criterion | 21 |
| 1.2.3 Magnetic confinement fusion | 23 |
| 1.2.4 Tokamak magnetic configuration | 24 |
| 1.2.5 Parameters of the tokamaks used in this work | 26 |
| 1.3 Plasma turbulence | 27 |
| 1.3.1 Heat and particle transport in tokamak plasmas | 27 |
| 1.3.2 Tokamak turbulence wave-number spectrum | 29 |
| 1.3.3 Drift wave turbulence | 30 |
| 1.3.4 Core plasma instabilities | 31 |
| 1.3.5 Geodesic acoustic mode (GAM) | 32 |
| 1.3.6 Scope of the work | 33 |
| 2 Ultra fast sweeping reflectometry | 35 |
| 2.1 Waves in magnetized plasmas | 35 |
| 2.1.1 Plasma dielectric tensor | 35 |
| 2.1.2 Ordinary mode (O-mode) | 37 |
| 2.1.3 Extraordinary mode (X-mode) | 37 |
| 2.1.4 Electromagnetic wave cut-off and resonances | 38 |
| 2.1.5 Wave propagation trough inhomogeneous plasmas | 39 |
| 2.1.6 Approximation of Wentzel-Kramer-Brillouin | 40 |
| 2.1.7 Wave propagation through a turbulent medium | 41 |
| 2.1.8 Mathieu equation | 41 |
| 2.2 Reflectometer description | 43 |

| | | |
|----------|---|-----------|
| 2.2.1 | Reflectometry basic principle | 43 |
| 2.2.2 | Homodyne IQ detection | 45 |
| 2.2.3 | Heterodyne IQ detection | 45 |
| 2.2.4 | Other reflectometry types | 46 |
| 2.3 | Closed loop algorithm | 47 |
| 3 | Reflectometer response computation methods | 49 |
| 3.1 | Helmholtz equation | 49 |
| 3.2 | Solution of 1D Helmholtz equation | 50 |
| 3.2.1 | 4th Order Numerov's method for Helmholtz equation | 50 |
| 3.2.2 | Electric field amplification phenomena | 51 |
| 3.2.3 | Numerical precision of the Numerov's method in the case of strong electric field amplification | 54 |
| 3.2.4 | Numerical precision of the Numerov's method with noisy density profile | 57 |
| 3.3 | Time dependent wave-equation numerical solution | 60 |
| 3.3.1 | 1D Wave equation solver IQ detection technique | 61 |
| 3.4 | Comparison between 1D Helmholtz equation solver and time dependant 1D wave equation solver | 62 |
| 3.4.1 | 2D FDTD algorithm | 68 |
| 3.5 | Reciprocity theorem approach | 71 |
| 3.5.1 | Reciprocity theorem in application to reflectometry modeling . . | 73 |
| 3.5.2 | Reduced reciprocity theorem approach | 74 |
| 3.5.3 | Reduced reciprocity theorem application example | 75 |
| 3.6 | Discussions | 78 |
| 4 | Strong edge turbulence effects on reflectometer plasma core measure- ments | 79 |
| 4.1 | Probing beam propagation through turbulent plasma | 79 |
| 4.1.1 | Beam properties change in turbulent plasma. Modeling examples | 80 |
| 4.2 | Study of edge turbulence effects on reflectometer signal | 88 |
| 4.2.1 | Edge turbulence effects on reflectometer phase spectra using edge- core k-spectra separation | 88 |
| 4.2.2 | Edge turbulence effects on reflectometer signal in slab geometry | 91 |
| 4.2.3 | Mono wave-number mode observation through strong turbulence level | 95 |
| 4.2.4 | Edge turbulence effects on reflectometer signal for Tore-Supra 2D profile | 98 |

| | | |
|----------|---|------------|
| 4.3 | Discussions | 102 |
| 5 | Application to gyro-kinetic simulations data and experimental measurements | 103 |
| 5.1 | Synthetic diagnostic application to GYSELA gyro-kinetic simulation . . | 103 |
| 5.2 | ASDEX-Upgrade UFSR synthetic diagnostic | 107 |
| 5.2.1 | Phase fluctuation and amplitude fluctuation spectra | 109 |
| 5.2.2 | Turbulence correlation length measurements | 113 |
| 5.2.3 | Conclusions and discussion | 116 |
| | Summary | 117 |
| | Zusammenfassung | 121 |
| | Bibliography | 126 |
| A | Isotropic turbulence generation | 137 |
| B | Miller equilibrium for shaped turbulence | 143 |
| C | Edge turbulence influence on the reflectometer phase | 147 |

List of used characters

| Character | Description | units |
|--------------|---|---------------------|
| A | amplitude of reflectometer signal | [V] |
| A_0 | amplitude of reflectometer emitted signal | [V] |
| a_f | refraction index perturbation envelop | [-] |
| A_i | Helmholtz equation differential scheme coefficient in chapter 3 | [-] |
| A_i | RMS turbulence amplitude envelop in Appendix B | [-] |
| a_i | Mathieu equation stable solution function | [-] |
| A_r | amplitude of reflectometer received signal | [V] |
| A_{ref} | amplitude of reference signal | [V] |
| A_ω | reciprocity theorem complex coefficient | [-] |
| a | turbulence RMS amplitude fit coefficient | [-] |
| B | magnetic field strength | [T] |
| b | turbulence RMS value fit coefficient | [-] |
| b_i | Mathieu equation stable solution function | [-] |
| B_i | Helmholtz equation differential scheme coefficient in chapter 3 | [-] |
| β | trapped particle banana orbit width | [m] |
| c | speed of light | [m/s] |
| C_i | Helmholtz equation differential scheme coefficient in chapter 3 | [-] |
| D_n | density gradient transport coefficient | [m ² /s] |
| D_T | temperature gradient transport coefficient | [1/m/s/K] |
| d_f | refractive index perturbation envelop width | [m] |
| D_ω | electric displacement field of frequency ω | [V/m] |
| δE | electric field perturbation | [V/m] |
| δB | magnetic field strength perturbation | [T] |
| δT | temperature perturbation | [K] |
| δn | density perturbation | [m ³] |
| $\delta\phi$ | phase variation | [rad] |
| E | electric field | [V/m] |

| | | |
|-------------------|---|---------------|
| e | electron index | [-] |
| E_α | alpha particle energy | [J] |
| E^G | GAM electric field | [V] |
| E_ω | electric field harmonic with circular frequency ω | [V/m] |
| E_{out} | electric field of reflected wave | [V/m] |
| E_{wg} | electric field fundamental mode of the wave-guide | [V/m] |
| ϵ_0 | vacuum dielectric permittivity | [F/m] |
| F | frequency | [Hz] |
| f_0 | frequency sweep start frequency | [Hz] |
| f_r | neutron yield | [$1/m^3/c$] |
| F_m | low frequency reflectometer oscillator frequency | [Hz] |
| F_b | beat frequency | [Hz] |
| Γ_j | particle flux of specie "j" | [$1/m^2/s$] |
| Γ_j^δ | particle flux of specie "j" associated with turbulence | [$1/m^2/s$] |
| H_ω | magnetic field strength harmonic with circular frequency ω | [V/m] |
| h | numerical scheme resolution | [-] |
| H_{wg} | magnetic field of the fundamental mode of the wave-guide | [T] |
| h_e | X-mode correction coefficient | [-] |
| i | imaginary unit | [-] |
| I^s | sin part of complex reference reflectometer signal | [V] |
| I^c | cos part of complex reference reflectometer signal | [V] |
| I | complex reflectometer signal | [V] |
| I_{ref}^s | sin part of complex received reflectometer signal | [V] |
| I_{ref}^c | cos part of complex received reflectometer signal | [V] |
| I_{in} | unperturbed reflectometer signal | [V] |
| I_s | turbulence related reflectometer signal | [V] |
| J | current density | [$C/s/m^2$] |
| k | electromagnetic wave wave-number | [m^{-2}] |
| k_0 | electromagnetic wave vacuum wave-number (except section 1.2.2) | [m^{-2}] |
| k_b | Boltzmann constant (only in section 1.2.2) | [m^{-2}] |
| k_{scat} | scattered field wave-number | [rad/m] |
| k_{turb} | turbulence wave-number | [rad/m] |
| k_{inc} | incident beam wave-number | [rad/m] |
| k_f | refractive index perturbation wave-number | [rad/m] |
| κ | coherent field attenuation coefficient | [-] |
| L_n | density gradient length | [m] |

| | | |
|-------------------------|--|----------------------|
| l_{nc} | density fluctuation correlation length across the magnetic field | [m] |
| Λ | Numerov's method operator | [-] |
| λ | wave-length | [m] |
| m_α | particle mass of specie " α " | [kg] |
| μ_0 | The magnetic constant | [N/A ²] |
| N | refractive index | [-] |
| n | electron plasma density (except section 3.3) | [1/m ³] |
| n | time-step index (only in section 3.3) | [1/m ³] |
| n_i | plasma density of specie "i" | [1/m ³] |
| n^G | GAM density fluctuation | [m ³] |
| n_0^G | GAM density fluctuation amplitude | [m ³] |
| n_c | electromagnetic wave critical electron density | [m ⁻³] |
| N_0 | refractive index of unperturbed plasmas | [-] |
| P_{Hex} | external heating power | [W] |
| $P_{H\alpha}$ | power received from fusion alpha-particles | [W] |
| $P_{neutron}$ | power produced by fusion neutrons | [W] |
| P_{losses} | power losses from the plasma | [W] |
| p | Mathieu equation parameter | [-] |
| ϕ | phase (except chapter 1) | [rad] |
| Φ | electric potential | [V] |
| Φ^G | GAM electric potential | [V] |
| ϕ | poloidal angle (only in chapte 1) | [rad] |
| ϕ_r | phase of reference signal | [rad] |
| ϕ_{ref} | phase of reflected signal | [rad] |
| ϕ_{vacuum} | phase of reflected wave obtained in the vacuum region | [rad] |
| ϕ_0 | initial beam phase | [rad] |
| π | pi constant | [-] |
| Q | fusion reactor efficiency coefficient | [-] |
| q | charge (except 2.1.8) | [C] |
| q | Mathieu equation parameter (only in section 2.1.8) | [-] |
| q_α | charge of specie " α " | [C] |
| r_i | radial position of computational grid-point "i" | [m] |
| R | radial position | [m] |
| ρ | Larmor radius | [m] |
| $S_{\delta n}^{pow}$ | density perturbation wave-number power spectrum | [m ⁻⁶] |
| $S_{\delta \phi}^{pow}$ | phase variation wave-number power spectrum | [rad ² m] |

| | | |
|----------------------------|--|-------------|
| $S_{\delta\phi_0}^{pow}$ | experimental phase variation power wave-number spectrum | $[rad^2m]$ |
| S_{wg} | wave-guide surface | $[m^2]$ |
| S_A | modulus of signal amplitude variation wave-number spectrum | $[V]$ |
| S_c | modulus of complex reflectometer signal wave-number spectrum | $[V]$ |
| $S_{\delta\phi}$ | modulus of reflectometer signal phase variation wave-number spectrum | $[rad]$ |
| $\hat{\sigma}$ | plasma conductivity tensor | $[C/s/m/V]$ |
| σ | fusion reaction cross-section | $[m^2]$ |
| Tr | transfer function | $[rad^2m]$ |
| T_i | temperature of specie "i" | $[K]$ |
| T | temperature | $[K]$ |
| t | time | $[s]$ |
| τ_{nc} | density fluctuation correlation time | $[m]$ |
| τ_E | energy confinement time | $[s]$ |
| θ | toroidal angle | $[rad]$ |
| V | plasma volume | $[m^3]$ |
| v | particle velocity | $[m/s]$ |
| $\vec{v}_{B \times F}$ | $B \times F$ drift velocity in presence of external force | $[m/s]$ |
| $\vec{v}_{B \times gradB}$ | $B \times gradB$ drift velocity in presence of magnetic field gradient | $[m/s]$ |
| $\vec{v}_{E \times B}$ | $E \times B$ drift velocity in presence of electric field | $[m/s]$ |
| v_c | sound velocity | $[m/s]$ |
| v^G | GAM particles velocity | $[m/s]$ |
| v_f | frequency sweeping rate | $[Hz/s]$ |
| W | weighting function | $[V^2]$ |
| ω | circular frequency | $[rad/s]$ |
| ω_c | electron cyclotron frequency | $[rad/s]$ |
| ω_p | plasma osculation circular frequency | $[rad/s]$ |
| ω_{UH} | upper hybrid resonance circular frequency | $[rad/s]$ |
| ω_H | X-mode high cut-off circular frequency | $[rad/s]$ |
| ω_L | X-mode low cut-off circular frequency | $[rad/s]$ |
| ω_{scat} | scattered field circular frequency | $[rad/s]$ |
| ω_{inc} | incident beam circular frequency | $[rad/s]$ |
| ω_{turb} | turbulence circular frequency | $[rad/s]$ |
| x | coordinate | $[m]$ |
| x_f | refraction index perturbation envelop position | $[m]$ |
| ξ | Mathieu equation space variable | $[-]$ |

| | | |
|---------|--|---------|
| ξ_1 | turbulence RMS value fit coefficient | [-] |
| ξ_2 | turbulence RMS value fit coefficient | [-] |
| y | poloidal coordinate | [m] |
| z | coordinate collinear with magnetic field | [m] |

Chapter 1

Introduction

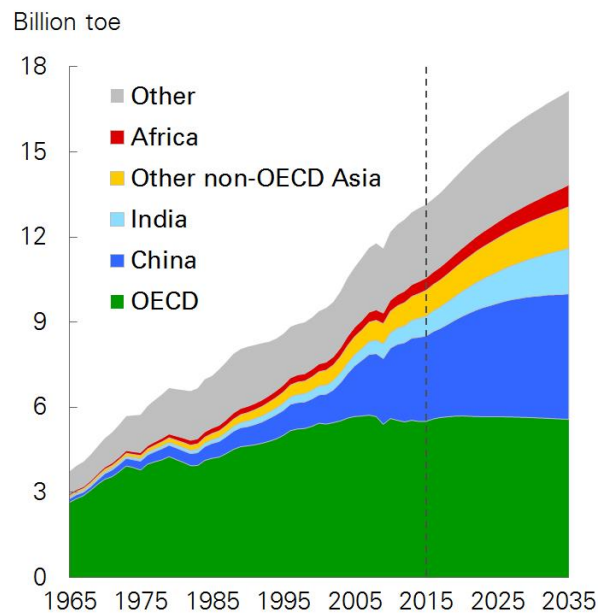


Figure 1.1: Primary energy consumption by different regions in the last 50 years with time extrapolation. Sourced from [1]

Nowadays growing world demands for energy and ecological restrictions applied on classic energy sources make us look for new renewable sources of energy. Renewable energy sources are sources which could be renewed on the human time-scale or Inexhaustible during much longer time than human time-scale. For the last 30 years world energy consumption has grown by more than 2.5 times (figure 1.1). As we see on figure 1.1 in Europe and North America this consumption level growth has decreased in last years. This is due to growing cost of the energy, more efficient energy use due to developed technologies, advanced ecological norms and redistribution of factories in direction of Asian-Pacific regions. Conversely in Asia-Pacific regions including so called developing countries, due to the growth of population and fast industrial de-

velopments, energy consumption grows very fast. But as it happened in developed European countries, after some time this growth should slow down. However even at current consumption rate, the ecological situation requires new green energy sources.

1.1 Sources of the energy

It is possible to separate available energy sources in 3 groups [2].

- Chemical energy: coal, oil, gas, fossil fuels;
- Nuclear energy: fission of uranium or thorium, fusion of light elements(deuterium, tritium);
- Renewable energy: hydro, wind, solar, thermal, photo voltaic, geothermal [3], [4], [5]

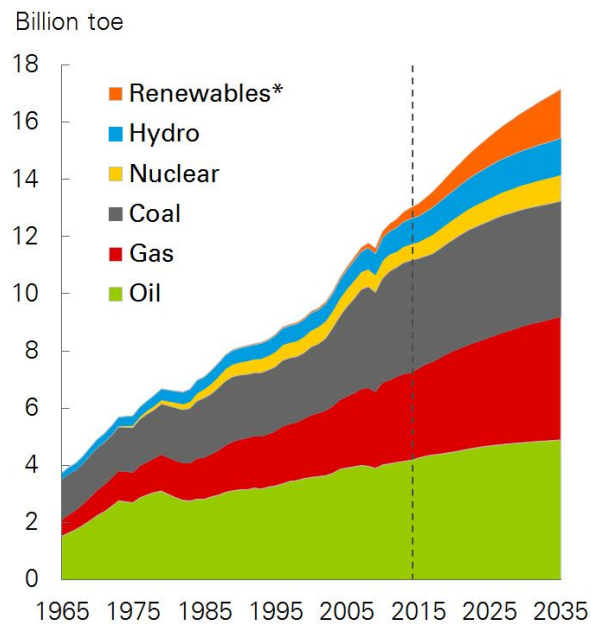


Figure 1.2: Primary energy consumption by fuel with extrapolation in time. Sourced from [1]

Electricity production from chemical energy usually connects with large CO_2 emission and air pollution with substances such as nitrogen oxides [6] which are very harmful for life nature. Figure 1.2 shows that in the past and at this moment the main part of the energy production comes from the first category, chemical energy. This has produced a big impact on the "global warming problem" [7]. Considering renewable energy sources (RES), wind and sun energy at the moment covers only 3% of the total

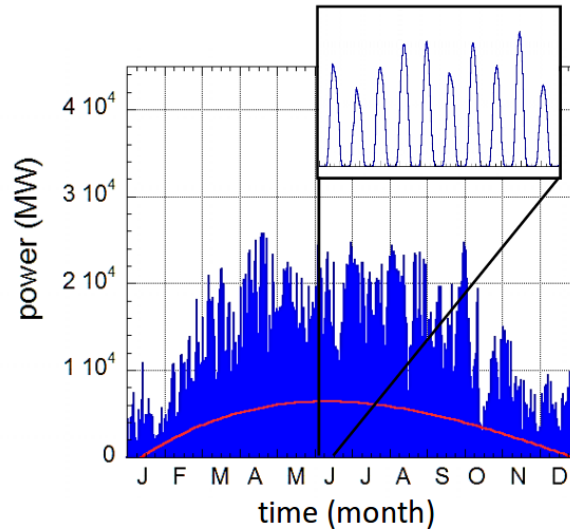


Figure 1.3: An example of produced solar power during one year in Germany. Figure taken from [8]

produced energy (see figure 1.2). These energy sources are not constant in time and require good backup and/or energy storage. Hydro power is less than 7% and the growth of this source is quite limited by irregular geographical location. Modern fission based on breeder reactor technology with fast neutrons could be a good candidate to replace old fission reactors and burning of fossil fuels. This technology can sufficiently reduce nuclear waste and increase safety. Unlike conventional reactors which uses uranium-234 it can use other isotopes of uranium and other heavy nucleus. This solves problem of limited amount of Uranium-234. Unfortunately distrust of fission in general from the civil society is too strong for these reactors to become widely used in recent future.

With limited use of nuclear power plants and burning of fossil, fuels countries should rely more on RES. Power generated by these sources vary much in time. An example of solar generated power variation is presented on figure 1.3. To provide power level able to support peaks of the power consumption, a wide network of different types of RES should be created [2]. This network should include backup systems in case there will be temporal decrease of RES output power, for instance backup gas power plant can be used. At the moment there is no technology to store big amounts of energy. It was shown that the entire RES network in Europe and the United States is not efficient unless some technological breakthroughs will happen [2, 9].

1.2 Nuclear fusion

Another solution which can become available in the end of the century is magnetic confinement nuclear fusion. In this section we will have a look on plasma tokamak confinement basics and highlight concepts needed for this thesis work presentation. However more precise information could be found in the following sources [10, 11].

1.2.1 Introduction to nuclear fusion

The idea behind nuclear fusion comes from the sun. Sun energy is produced by fusion of light atoms. But unlike the sun, earth fusion will use more effective in sense of energy yield deuterium-tritium (D-T) reaction and in perspective D-D reaction. In order to fuse atoms should first overcome an electric repulsion. This is possible only at very high energy ($10 - 20keV$). Ionized gas where particles have that energy should be confined to maintain the required high density. High densities are needed to have high fusion rate (1.1):

$$f_r = n_1 n_2 \langle \sigma v \rangle \quad (1.1)$$

where n_1 and n_2 are the density of fusion species, σ is the fusion reaction cross-section, and v is the relative velocity of fusing atoms. This expression gives information on how many reactions are produced per second in the volume unit. Because of a relatively larger cross-section for smaller energies, deuterium-tritium (D-T) plasma reaction was chosen to make earth fusion. Table 1.1 shows possible reactions and reaction product energy from D-T plasmas. Figure 1.4 represents cross-sections of these reactions. As

| fusing species | products and its energies |
|----------------|---------------------------------------|
| $D + T$ | $He_2^4(3.56MeV) + neutron(14.03MeV)$ |
| $D + D$ | $He_2^3(0.82MeV) + neutron(2.45MeV)$ |
| $D + D$ | $T(1.01MeV) + H(3.02MeV)$ |
| $D + He_2^3$ | $He_2^4(3.71MeV) + H(14.64MeV)$ |

Table 1.1: Fusion reactions and products

one can see from this figure, $D - T$ reaction has the highest rate with a maximum reached for temperatures near $100keV$. A $14.03MeV$ neutron is a product of this reaction. This fast neutron's energy is then to be transferred to electricity. Alpha particles resulting from the same reaction will be used to transfer its energy to the main plasma species. Hydrogen is the most distributed nuclei in universe. Its isotope deuterium is stable and distributed quite well on the Earth. In the ocean, for 6420 atoms of hydrogen there is one atom of deuterium. Tritium will be produced using lithium and fast

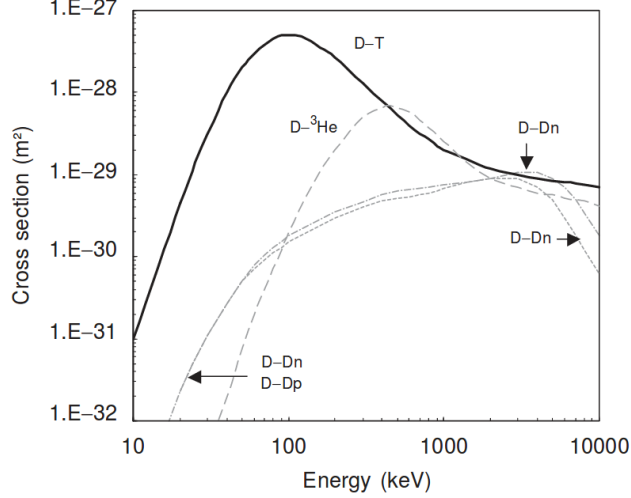


Figure 1.4: Cross-sections of possible nuclear reactions. Averaging is done using Maxwellian velocity distribution function. Figure source: "Encyclopedia of Energy", Volume 4. (Elsevier Inc., 2004)

neutrons from main fusion reaction (Table 1.2). Fusion can be considered as renewable

| fusing species | products |
|------------------|------------------------|
| $neutron + Li^6$ | $T + He_2^4$ |
| $neutron + Li^7$ | $T + He_2^4 + neutron$ |

Table 1.2: Tritium production reactions

energy source as amount of deuterium and tritium is enough to power humanity for millions of years [12]. Cross-sections of the two $D - D$ reactions are very close to each other, which gives a probability of 50% each. However these cross-sections are much smaller than the cross-section of $D - T$ and $D - He_2^3$ reactions.

1.2.2 Ignition criterion

As shown in figure 1.4, fusion requires very high temperatures. But to be used as energy source fusion reactors should fulfil a few other conditions. Hot plasmas have quite strong convection and diffusion of heat and particles, which means that in any case energy losses take place. They can be described by energy confinement time τ_E , which is the characteristic time of energy loss by the plasma without external heating. Fusion plasmas can be heated by fast fusion alpha particles and external heating. Now we can express the energy balance when the total plasma heating is equal to the plasma losses.

$$P_{Hex} + P_{H\alpha} = P_{losses} \quad (1.2)$$

Where P_{Hex} is an external heating power, $P_{H\alpha}$ is the plasma heating power received from alpha particles. Let's look on what plasma parameters are crucial for fusion device.

$$P_{H\alpha} = \frac{1}{4}n^2 \langle \sigma v \rangle E_\alpha V \quad (1.3)$$

Expression (1.3) is calculated for the most optimal case when the plasma consists only of deuterium and tritium in equal proportions. $E_\alpha = 3.56MeV$ is in the fusion α particle born energy, V is the plasma volume, and n is the plasma density.

$$P_{losses} \approx 3nk_bTV/\tau_E \quad (1.4)$$

$3nk_bTV$ is an estimating formulation of the plasma kinetic energy content, where T is the temperature and k_b - the Boltzmann constant. From formulas (1.2-1.4) one can express the needed external heating power to maintain burning plasma conditions:

$$P_{Hex} = \left(\frac{3nk_bT}{\tau_E} - \frac{1}{4}n^2 \langle \sigma v \rangle E_\alpha \right) V \quad (1.5)$$

Without external heating we will achieve the so-called ignition criterion when losses are fully compensated by fusion α particles power.

$$n\tau_E > \frac{12k_bT}{\langle \sigma v \rangle E_\alpha} \quad (1.6)$$

$\langle \sigma v \rangle$ of the $D - T$ reaction can be approximated with 10% accuracy in the range of 6-20 keV to:

$$\langle \sigma v \rangle \approx 1.1 \cdot 10^{-24} T^2 \quad (1.7)$$

This allows us to calculate the so-called triple product criterion.

$$n\tau_E T > 3 \cdot 10^{21} [m^{-3} keVs] \quad (1.8)$$

This simple estimation can give us an idea on the main parameters values which should be achieved for successful fusion reactor prototype construction. At the moment there are 2 main concepts: inertial fusion, and magnetic confinement fusion (MCF). In inertial fusion solid state fuel target is compressed and heated by multiple laser rays homogeneously distributed over its surface. With this method plasma density is very high while energy confinement time is short. On the contrary magnetic confinement fusion relies on energy confinement time of few seconds and small densities. Typical target values that MCF tries to achieve are: $n = 10^{20}m^{-3}$, $T = 10keV$, and $\tau_E = 3s$

To describe reactor efficiency when additional heating is applied to the plasma,

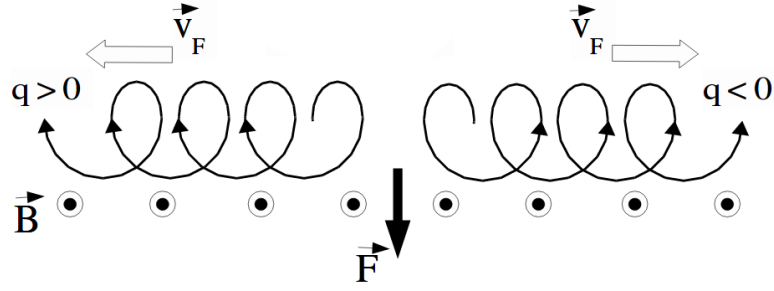


Figure 1.5: Charged particle drift in magnetic field with external force. Plasma ions and electrons are drifting in opposite directions. Picture has been taken from [13]

efficiency coefficient Q can be estimated as:

$$Q = P_{neutron}/P_{Hex} \quad (1.9)$$

Here we don't take into account the energy transfer efficiency from energetic neutrons to electricity. This will be done by transfer heat from the blanket wall which will be irradiated by fusion neutrons. Also it is important to mention that most neutron yield is coming from the high energy tail of ion velocity distribution function. Heating methods like neutral beam injection, ion cyclotron resonance heating (ICRH) or lower hybrid resonance heating and current drive (LHCD) enlarge the high energy tail of the velocity distribution function. These fast ions are expected to generate significant part of fusion neutrons.

1.2.3 Magnetic confinement fusion

The sun confines its fusion plasma using strong gravitation forces. On the Earth this mechanism is not applicable. As plasmas consist of charged particles they can be caged by magnetic field. With the magnetic field charged particles are moving as spirals, around magnetic lines with the Larmor radius $r_l = \frac{mv_{\perp}}{qB}$. Here v_{\perp} is the particle velocity projection on perpendicular direction to magnetic field. If an external force applied to the particles it creates a constant velocity motion called drift (1.10).

$$\vec{v}_{B \times F} = \frac{1}{q} \frac{[\vec{F} \times \vec{B}]}{B^2} \quad (1.10)$$

Here \vec{F} and \vec{B} are vectors of external force and magnetic field respectively. Figure 1.5 shows particle trajectories during drift motion. In MCF this force can be created by

gravitation, electric field, magnetic field gradient, temperature or pressure gradients and magnetic lines curvature. There are two main machine design concepts that are designed to limit this motion in a predefined volume. They are tokamaks and stellarators. Both are based on the similar idea to close magnetic lines in a circle. This will create a toroidal magnetic configuration in which particles are moving along magnetic lines. But such a configuration results in magnetic field that decreases with the major radius. This magnetic field gradient creates a drift of plasma ions and electrons (1.11).

$$\mathbf{v}_{\mathbf{B} \times \text{grad} \mathbf{B}} = \frac{K_{\perp}}{qB} \frac{[\vec{B} \times \text{grad} B]}{B^2} \quad (1.11)$$

Where K_{\perp} is perpendicular kinetic energy. This drift is directed in opposite directions for ions and electrons. It creates charge separation and vertical electric field. Vertical electric field will also create a drift (1.12) which will move the whole plasma outside the torus and limit energy confinement time by this movement.

$$\mathbf{v}_{\mathbf{E} \times \mathbf{B}} = \frac{[\vec{E} \times \vec{B}]}{B^2} \quad (1.12)$$

Simple toroidal magnetic configuration results in plasma self movement, the same way as did famous Baron Münchhausen.

Not far from the other side I fell into the bog. Here I would have undoubtedly died, if not the strength of my own arm, grabbing my own pigtail, had pulled me, including my horse—which I squeezed tightly between my legs—out of it (Baron Münchhausen)

The way how this problem is solved is the main difference between tokamaks and stellarators. More details will be given in next section.

1.2.4 Tokamak magnetic configuration

To avoid vertical electric field effect one can twist the magnetic lines around small cross-section of the torus (in poloidal direction). As ions and electrons move freely along the magnetic lines, in other words plasma conductivity along the magnetic lines is very high (see section 2.1.1), this poloidal magnetic lines transformation will connect upper and down sides of the machine with magnetic lines. Current along these magnetic lines will remove the electric field produced by vertical charge separation. The current which cancel this electric field is called Pfirsch-Schlüter current. The main difference between tokamaks and stellarators is that stellarators produce such a magnetic field poloidal rotation using complex shape of magnetic coils whereas tokamaks

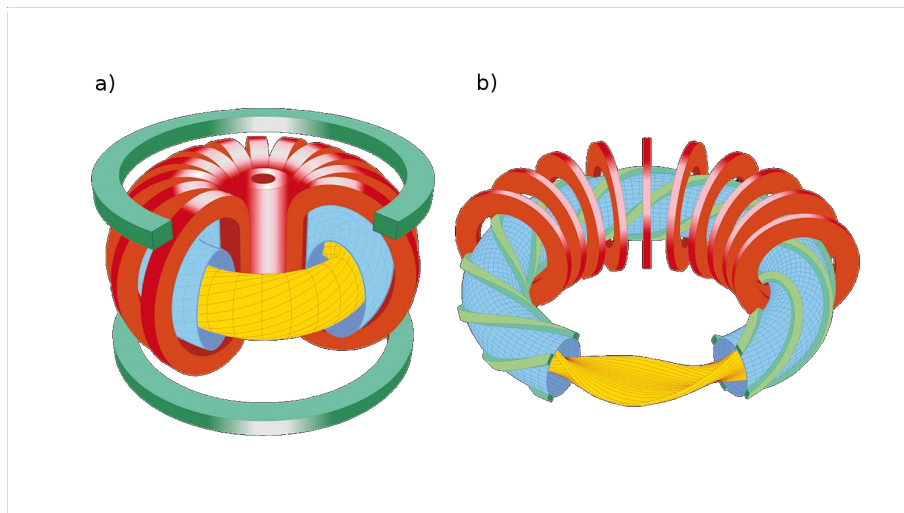


Figure 1.6: a) tokamak basic coil design and plasma shape b) stellarator coils with curved plasma, picture inspired by www.ideen2020.de/wpcontent/uploads/slideshow-gallery/5_tokamak_stellarator_a_RGB.jpg (entered 17.06.2018)

have a toroidal plasma current which creates a poloidal twist of the magnetic field lines (figure 1.6). In this work we will focus on the tokamak geometry. Readers can find more information about stellarators in [14]. In the tokamak configuration toroidal coils which create the toroidal magnetic field are combined with the central solenoid column. The column itself is a transformer core and the plasma loop is a secondary coil. This solenoid is made to drive the plasma toroidal current. Due to horizontal forces which try to expand the plasma loop, additional coils are required for the equilibrium. These forces are:

- 1) Pressure: Along the magnetic lines over one magnetic surface, the pressure stays constant. However the inner surface of the torus is smaller than the outer surface. This results in pressure force that is stronger on outer side than on inner one.
- 2) Toroidal current: the current loop always has an expanding force created by interaction with its own magnetic field.

To compensate these forces in the tokamak, vertical magnetic field coils are used. These coils create a vertical magnetic field which interacts with the plasma current, then creating a horizontal force directed towards the plasma current loop center. In modern tokamaks plasmas usually are shaped to be elliptically elongated and triangular. In divertor tokamaks [15] the last closed magnetic surface has a so-called X-point. This X-point directs plasma flow from the separatrix to a specially designed plate (divertor). This technology helps to decrease the power loads on the first wall. Additional shaping coils are used to obtain the desirable magnetic equilibrium. On figure 1.7 is represented the magnetic coil configuration of the ASDEX-upgrade tokamak.

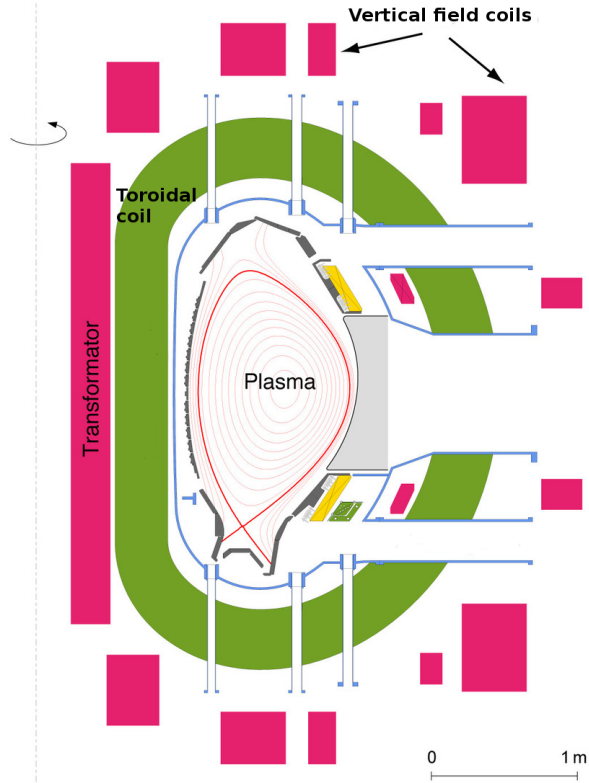


Figure 1.7: ASDEX-upgrade tokamak poloidal cross-section with magnetic coils configuration. Picture inspired by www.ipp.mpg.de/4324839/original-1517424707.jpg (entered 17.06.2018)

1.2.5 Parameters of the tokamaks used in this work

In my thesis work part of the reflectometry computations were done using real tokamak geometry and density profiles. These tokamaks are: Tore-Supra, JET (Joint European Torus), and ASDEX-Upgrade (Axially Symmetric Divertor EXperiment). In this section main parameters of these machines are introduced.

| Parameter max(typical) | JET | ASDEX-Upgrade | Tore-Supra |
|---------------------------------|---|-------------------|---------------------------------------|
| Location | Culham, UK | Garching, Germany | CEA Cadarache, France |
| Cross-section | D-shaped | D-shaped | Circular |
| minor radius [m] | 1.25-2.1 | 0.5-0.8 | 0.7 |
| major radius [m] | 3 | 1.65 | 2.4 |
| plasma volume [m ³] | 100 | 13 | 25 |
| B [T] | 3.45 (2.5-3.2) | 3.1 (2.5) | 4.2 (3.75) |
| I [MA] | 4.8 (2.5) | 1.6 (0.4-1.4) | 1.4 (0.5-1.2) |
| n_e [m ⁻³] | $2 \cdot 10^{19}$ - $1.1 \cdot 10^{20}$ | $< 10^{19}$ | $1 \cdot 10^{19}$ - $9 \cdot 10^{20}$ |
| pulse duration [s] | <30 | <10 | <400 |

Table 1.3: Parameters of some tokamaks

No experimental work was performed by the author. All data used in the simulations were used under collaboration with various groups: Tore-Supra (S. Hacquin, F. Clairet, G. Dif-pradalier, R. Sabot), ASDEX-Upgrade (F. Clairet, A. Medvedeva), and JET (F. Clairet).

1.3 Plasma turbulence

1.3.1 Heat and particle transport in tokamak plasmas

In tokamak plasmas density and temperature are not homogeneous. Due to the tokamak geometry and radial transport, particle density and temperature are peaked in the plasma core. Plasma density profile can vary with minor radius up to a few orders of magnitude. In section 1.2.2 we saw that for advanced performances of a fusion power plant, energy confinement time τ_E is a very critical parameter. This parameter is mostly defined by plasma instabilities and plasma turbulence as they drive heat and particle transport in a tokamak. Turbulence is usually present in tokamak discharges. Numerous experiments have shown fluctuations of many plasma parameters as plasma density δn , temperature δT , plasma potential $\delta\phi$, plasma current density δJ , electric and magnetic fields δE , δB . Further information can be found in N. Bretz's paper [16]. To express the connection between turbulence and anomalous transport let us look at the generalized form of the transport coefficients. Anomalous fluxes of bilinear correlations of perturbations can be written according to Ross [17]

$$\Gamma_j = -D_n \frac{\partial n_j}{\partial r} - D_T \frac{\partial T_j}{\partial r} + v n_j + \Gamma_j^\delta \quad (1.13)$$

$$Q_j = -\chi_{jT} n_j \frac{\partial T_j}{\partial r} - \chi_{jn} T_j \frac{\partial n_j}{\partial r} + v n_j T_j + \frac{5}{2} k_b T_j \Gamma_j + Q_j^\delta \quad (1.14)$$

Where Γ_j and Q_j are ambipolar particle and energy fluxes of species j . The total flux consists of a sum of terms defined by Coulomb collisions (neoclassical transport) and Γ^δ fluxes associated with turbulence (anomalous transport), D and χ are respectively transport coefficients of particle and temperature, v is the convective velocity. Anomalous particle and energy fluxes driven by $E \times B$ drift can be associated with variations of electric field δE as one expects the magnetic particle diffusion term to be negligible.

$$\Gamma_j^{\delta E} = \langle \delta n_j \delta v_r \rangle = \langle \delta E_\theta \delta n_j \rangle / B_\phi \quad (1.15)$$

Here θ is the poloidal angle, ϕ is the toroidal angle, r means radial coordinate, and \parallel and \perp signs are related to the magnetic field direction. Drift turbulence energy flux

can be expressed the same way.

$$Q_j^{\delta E} = -\frac{3}{2}k_b n_j \langle \delta E_\theta \delta T_j \rangle / B_\phi + \frac{3}{2}k_b T_j \langle \delta E_\theta \delta n_j \rangle / B_\phi \quad (1.16)$$

Convictional flux $Q_{conv}^{\delta E} = \frac{5}{2} \frac{k_b T_e}{B_\phi} \langle \delta E_\theta \delta n_e \rangle$ can be calculated if both δn_e and δE_ϕ are measured simultaneously. However by means of wave scattering, reflectometry, electron cyclotron emission, and beam emission spectroscopy only δn of δT can be measured and additional assumptions should be added to compute energy and particle fluxes.

Assuming a specific type of turbulence, one can simplify the task. Electrostatic drift waves are driven by plasma pressure gradient and could appear in many regions of tokamak plasmas. For all electrostatic modes a general expression can be written.

$$\frac{\delta n_e}{n_e} \sin(\psi) = \frac{e \delta \Phi}{k_b T_e}; k_\phi \delta \Phi = -\delta E_\phi \quad (1.17)$$

In this expression ψ is the phase between δn_e and $\delta \Phi$ - the plasma potential. The particle flux in this case can be expressed as:

$$\Gamma_j^{\delta E} = n_e v_{Te} \rho_{ce} \left\langle \frac{\delta n_e^2}{n_e^2} k_\theta \sin(\psi) \right\rangle \quad (1.18)$$

Here $v_{Te} \rho_{ce} = c \frac{T_e}{e B_\phi}$ and $v_{Te} = \sqrt{k_b T_e / m_e}$ is the thermal speed, and $\rho_{ce} = v_{Te} / \omega_{ce}$ is the electron cyclotron radius. There is a theory [18] as well as experimental observations [19] to express the phase ψ . However in this subsection, for simplicity we will consider limiting the expression under conditions of strong turbulence which is called mixing length limit, when $\delta n_e / n_e \approx 1 / k_r L_n \ll 1$, $\sin(\psi) \approx 1$ where L_n is the density gradient length $1 / L_n = -d(\ln(n_e)) / dr$. Under isotropy assumption $k_r \approx k_\theta$ we can find:

$$D_n^{\delta E}(\text{strongturbulence}) \approx v_{Te} \rho_{ce} \frac{\delta n_e}{n_e} \quad (1.19)$$

Such conditions are typical for plasma core where density fluctuation $\delta n_e / n_e < 1\%$

Another way to estimate the particle diffusion coefficient is based on the general random walk using averaged space step across the magnetic field and correlation time.

$$D_n^{\delta E}(\text{randomwalk}) \approx l_{nc}^2 / \tau_{nc} \quad (1.20)$$

where l_{nc} and τ_{nc} are correlation length and time of density fluctuations across the magnetic field.

Using these expressions one can conclude that to experimentally investigate particle and energy transport nature one has to measure fluctuations of density δn , temper-

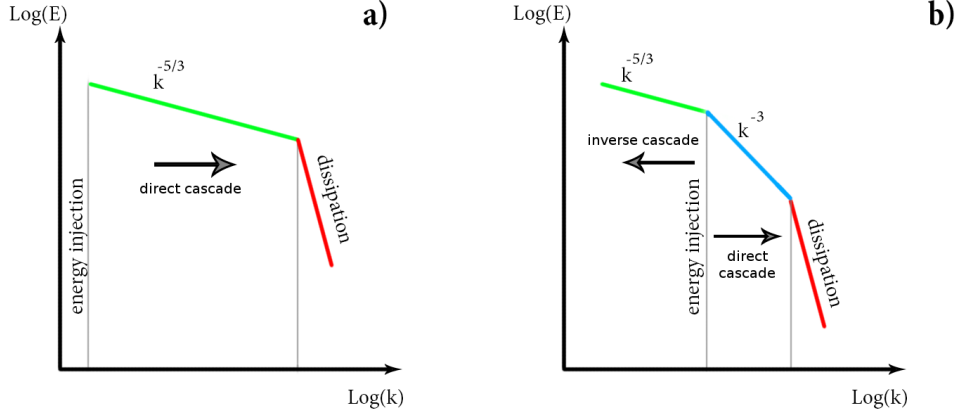


Figure 1.8: (a) Turbulence energy spectrum by Kolmogorov's theory. Direct cascades with $k^{-5/3}$ dependence; (b) Turbulence energy spectrum predicted by Kraichnan-Leith-Batchelor's model, with direct cascade k^{-3} and inverse cascade $k^{-5/3}$

ature δE , plasma potential $\delta\Phi$, electric and magnetic fields δE and δB . This thesis work will be focused on density perturbations properties measurements with microwave reflectometry.

1.3.2 Tokamak turbulence wave-number spectrum

Aside from electrostatic drift wave turbulence which was considered in previous section 1.3.1 other electrostatic modes were found to be source of anomalous transport: MHD-like modes driven by magnetic field curvature, ripple losses, viscosity, plasma current, electromagnetic skin depth modes [20], and thermal instabilities in plasma edge [21]. MHD-like modes have significantly longer wavelength comparing to skin depth mode and drift wave modes are sitting in between them.

In a tokamak, the turbulence energy obtained from free energy of pressure gradient can be transferred between turbulent modes with different wavelengths and frequencies. Moreover this energy can be exchanged with zonal flows and geodesic acoustic modes (GAM). GAM will be discussed in section 1.3.5. Frequency and wave-number spectra contain very important information, which allow us to verify theoretical models used in numerical modelling.

Numerous theoretical works were done to describe the turbulence behaviour. Kolmogorov's well-known work [22] describes homogeneous isotropic turbulence in 3D fluid. This model gives turbulence energy cascades in the direction of small scale turbulence (so called direct cascade) with spectral behaviour $k^{-5/3}$ figure 1.8(a). Energy propagates to smaller scale turbulence where viscosity plays a major role and leads to energy dissipation.

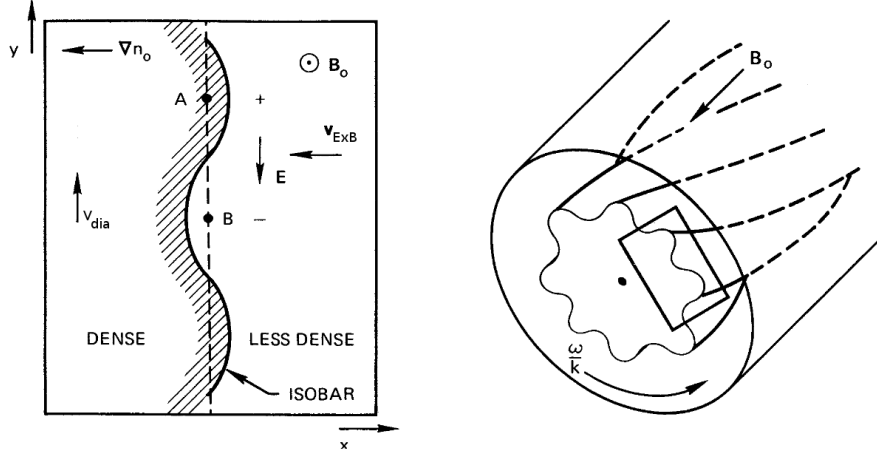


Figure 1.9: illustration of drift wave developing mechanism for adiabatic electrons. Reproduced from [11]

As tokamak plasmas are not isotropic due to the magnetic field 2D description is more natural. Under such conditions Kraichnan-Leith-Batchelor's (KLB) model was developed [23]. This model predicts direct energy cascade with typical k^{-3} dependence towards high wave-number direction from energy injection region (scale where energy is received by turbulence from kinetic instabilities), and energy cascade in the direction of smaller wave-number (inversed cascade) with $k^{-5/3}$ (figure 1.8(b)).

1.3.3 Drift wave turbulence

Drift wave instability is a basic linear instability. It could appear in plasmas with homogeneous magnetic field and density gradient. Periodic perturbation of electric field potential $\delta\Phi$ perpendicular to the direction of density gradient is assumed. Because of the electrons low mass they react fast on these perturbations. This results in charge separation in the direction perpendicular to the density gradient. The electric field appearing during this charge separation together with the magnetic field produces a particle drift. Under the approximation of adiabatic electrons ($\delta n_e = \frac{e\delta\Phi}{T_e} n_e$) the phase relation between potential variation phase and density perturbation doesn't make this perturbation unstable but leads to vertical drift with diamagnetic velocity (see figure 1.9). But in the case of collisions (plasma resistivity) this phase difference changes and the density perturbation becomes unstable and particles from higher density regions moves to smaller density regions.

1.3.4 Core plasma instabilities

In the plasma core region the density gradient doesn't reach high values as in the plasma edge region. However temperature profile is peaked closer to the plasma center. In this region ITG (ion temperature gradient), which is believed to be a major reason of anomalous ion temperature transport [24, 25], dominates ETG (electron temperature gradient) [26], trapped electron mode (TEM) [27], and trapped ion mode (TIM) [28, 29, 30]. These turbulent modes have different typical scale lengths. The scale is connected to Larmor radius ρ for passing particles and banana orbit width β for trapped particles. In the case of typical tokamak setup:

$$\beta_i > \rho_i \geq \beta_e > \rho_e \quad (1.21)$$

where indexes e and i mean electrons and ions.

Ion temperature gradient modes: small wave-number turbulence. Usually the most important modes in tokamak in terms of transport. It is driven by ion temperature gradient and can be stabilized by density gradient. They can also be stabilized by increase of impurities concentration. However impurities can have their own ITG instability with different frequencies due to their mass.

Trapped ion modes: the largest scale instabilities. Because of their scale they can induce strong transport. But these instabilities generally make small contribution to total transport. However when ITG are suppressed TIM should be taken into account for good turbulence representation [28].

Electron temperature gradient modes: Large wave-number instabilities. Because of their small scale they don't contribute much to transport. In the case of electron heating they can give large contribution to electron transport [31].

Trapped electron modes: Rising from temperature or density gradient, from interaction between electromagnetic waves and trapped electrons. They can be damped by collisionality as it vanishes velocity distribution function and decreases the number of trapped electrons. Also the magnetic shear can cause a stabilizing effect [32].

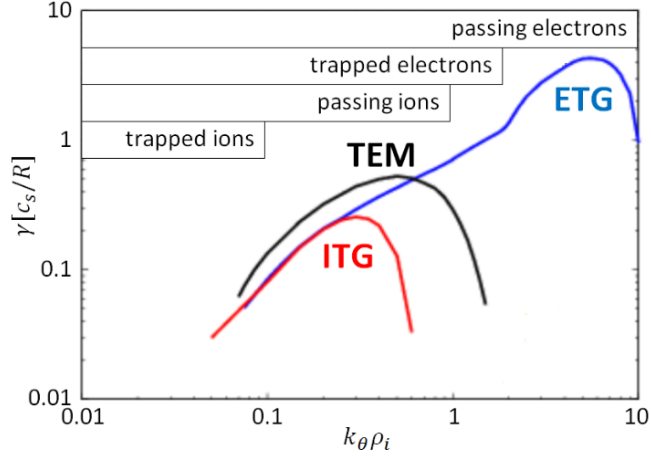


Figure 1.10: Instability growth rate γ as a function of normalized wave-number $k_\theta \rho_i$. Where k_θ is poloidal wave-number. Picture inspired by [33]

1.3.5 Geodesic acoustic mode (GAM)

Geodesic acoustic modes were named after similar phenomena in the planet atmosphere and were first discovered by N. Winsor [35]. Local (zonal) flows oscillate proportionally to the sound velocity v_c divided by the major radius. These flows are caused by radial potential variations. In the round cross-section toroidal tokamak shape these potential perturbations can be expressed as:

$$\Phi^G(r) = A^G(r) \exp(-i\omega t) \quad (1.22)$$

And the electric field which is associated with this potential can be found as $E^G = -d\Phi^G/dr$. This electric field leads to a poloidal plasma drift in addition to the main rotation caused by not perturbed radial field (see figure 1.11).

$$v^G = -cE^G/B \quad (1.23)$$

Particle flows created by this velocity are called zonal flows. In inhomogeneous magnetic field divergence of such fluxes does not equal to zero. It should be compensated by particle flows along magnetic field lines. These flows will change their direction with initial potential variations. Amplitude of these flows is proportional to $\cos(\theta)$, where θ is the poloidal angle. Parallel velocity is equal to:

$$v_{\parallel}^G(\theta) = v_{\parallel 0}^G \cos(\theta) \quad (1.24)$$

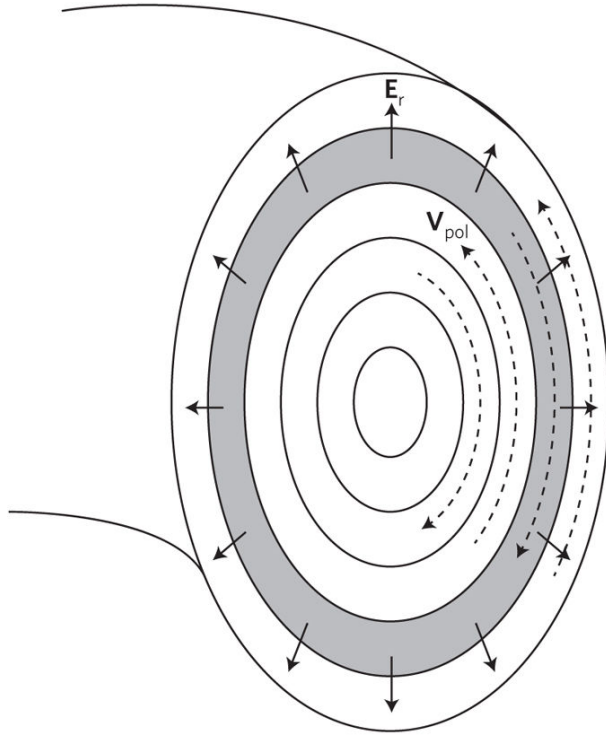


Figure 1.11: Toroidal tokamak cross-section with zonal GAM flows and radial electric field variation. Picture source - [36]

Parallel velocity also oscillates in time with cycle frequency ω . These fluxes should be created by pressure gradient along the magnetic lines, created by periodic density modulation:

$$n^G = n_0^G \sin(\theta) \quad (1.25)$$

To summarize, radial electric potential fluctuations give birth to poloidal and toroidal zonal flows, which lead to electric field perturbation modes with poloidal wave number $m = 0$, and density perturbation mode with $m = 1$. GAMs correspond to coherent structure which we will try to detect using reflectometry in the next chapters.

1.3.6 Scope of the work

Good understanding of turbulent transport and its prediction possibilities are essential for thermonuclear reactor design and operation. Diagnostic of plasma turbulence demands high temporal and spatial resolution. In the case of thermonuclear reactor there are limited number of diagnostics available. Plasma region situated close to the first wall can be investigated using Langmuir probes which is limited to operation in relatively cold plasmas [37]. Turbulence in the tokamak plasma core can be studied using technique called beam emission spectroscopy (BES) [38]. A very well-established technique that is expected to be the main turbulence diagnostic in ITER [39] is reflec-

tometry [40]. It is very flexible and can measure different turbulent modes as well as MHD instabilities, it has minimal excess requirements and can be used under strong neutron yield from plasma.

In this work applicability of the ultra-fast swept reflectometry (UFSR) will be investigated using 2D full wave code. The plan of the report is as follows:

Chapter 2: Electromagnetic waves in plasma physics basics will be introduced. Principle of reflectometer work will be explained.

Chapter 3: Numerical methods for reflectometry synthetic diagnostic will be highlighted.

Chapter 4: Reflectometer signal change by strong edge turbulence layer will be studied.

Chapter 5: Synthetic diagnostic will be applied to gyro-kinetic code data in Tore-Supra tokamak and based on experimental data in ASDEX-Upgrade tokamak.

Chapter 2

Ultra fast sweeping reflectometry

In this chapter I will highlight the theory behind wave propagation in magnetized plasmas. Also reflectometer principles and basic signal analysis will be presented.

2.1 Waves in magnetized plasmas

Next we will highlight basic physics behind reflectometer electromagnetic wave propagation into magnetized tokamak plasmas.

2.1.1 Plasma dielectric tensor

Now let us look on plasma particles motion in high frequency electromagnetic waves. Plasmas consist of ions and free electrons. Motion equations for these species look like:

$$\begin{cases} dv_{(\alpha)x}/dt = q_{\alpha}E_x/m_{\alpha} + q_{\alpha}v_{(\alpha)y}B_z/m_{\alpha} \\ dv_{(\alpha)y}/dt = q_{\alpha}E_y/m_{\alpha} - q_{\alpha}v_xB_z/m_{\alpha} \\ dv_{(\alpha)z}/dt = q_{\alpha}E_z/m_{\alpha} \end{cases} \quad (2.1)$$

This expression is written for strongly magnetized plasmas. This is to say collision frequency $\nu < \omega_c$. Magnetic field is directed parallel to z direction. There are no relativistic terms. This approximation is called cold plasma approximation. We will look for oscillating field solution with circular frequency ω - $E, v, B \propto e^{-i\omega t}$. Next in this section by E, B, v we will mean amplitude of complex fields. Then (2.1) becomes:

$$\begin{cases} -i\omega v_{(\alpha)x} = q_{\alpha}E_x/m_{\alpha} + q_{\alpha}v_{(\alpha)y}B_z/m_{\alpha} \\ -i\omega v_{(\alpha)y} = q_{\alpha}E_y/m_{\alpha} - q_{\alpha}v_xB_z/m_{\alpha} \\ -i\omega v_{(\alpha)z} = q_{\alpha}E_z/m_{\alpha} \end{cases} \quad (2.2)$$

From the first two equations one can express x and y velocities.

$$\begin{cases} v_{(\alpha)x} = -\frac{q_\alpha}{m_\alpha} \frac{w_c}{w^2 - w_{(\alpha)c}^2} E_y + i \frac{q_\alpha}{m_\alpha} \frac{w}{w^2 - w_{(\alpha)c}^2} E_x \\ v_{(\alpha)y} = \frac{q_\alpha}{m_\alpha} \frac{w_{(\alpha)c}}{w^2 - w_{(\alpha)c}^2} E_x + i \frac{q_\alpha}{m_\alpha} \frac{w}{w^2 - w_{(\alpha)c}^2} E_y \\ v_{(\alpha)z} = \frac{i q_\alpha E_z}{\omega m_\alpha} \end{cases} \quad (2.3)$$

With cyclotron frequency $w_c = qB/m$. Knowing particles velocities the current density can be calculated $\vec{J} = \sum_\alpha q_\alpha n_\alpha \vec{v}_\alpha$, where n_α is the plasma species density.

$$\begin{cases} J_x = \sum -\frac{n_\alpha q_\alpha^2}{m_\alpha} \frac{w_c}{w^2 - w_{(\alpha)c}^2} E_y + \sum i \frac{n_\alpha q_\alpha^2}{m_\alpha} \frac{w}{w^2 - w_{(\alpha)c}^2} E_x \\ J_y = \sum \frac{n_\alpha q_\alpha^2}{m_\alpha} \frac{w_{(\alpha)c}}{w^2 - w_{(\alpha)c}^2} E_x + \sum i \frac{n_\alpha q_\alpha^2}{m_\alpha} \frac{w}{w^2 - w_{(\alpha)c}^2} E_y \\ j J_z = \sum \frac{i n_\alpha q_\alpha^2 E_z}{\omega m_\alpha} \end{cases} \quad (2.4)$$

From these expressions using Ohm's law $\vec{J} = \hat{\sigma} \vec{E}$ one can calculate the plasma conductivity tensor $\hat{\sigma}$:

$$\hat{\sigma}_\alpha = \begin{bmatrix} \omega \epsilon_0 \frac{\omega_{(\alpha)p}^2}{\omega^2 - \omega_{(\alpha)c}^2} & i \omega_{(\alpha)c}^2 \epsilon_0 \frac{\omega_{(\alpha)p}^2}{\omega^2 - \omega_{(\alpha)c}^2} & 0 \\ -i \omega_{(\alpha)c}^2 \epsilon_0 \frac{\omega_{(\alpha)p}^2}{\omega^2 - \omega_{(\alpha)c}^2} & \omega \epsilon_0 \frac{\omega_{(\alpha)p}^2}{\omega^2 - \omega_{(\alpha)c}^2} & 0 \\ 0 & 0 & i \omega \epsilon_0 \omega_{(\alpha)p}^2 / \omega^2 \end{bmatrix} \quad (2.5)$$

Where $\omega_p^2 = \frac{n_\alpha q_\alpha^2}{m_\alpha \epsilon_0}$, ϵ_0 is the vacuum dielectric permittivity. With the help of conductivity tensor one can calculate the plasma dielectric permittivity tensor given by following expression:

$$\epsilon_{xy} = \delta_{xy} - \sum_\alpha \frac{\sigma_{(\alpha)xy}}{i \omega \epsilon_0} \quad (2.6)$$

Where δ_{xy} is Kronecker delta, $\delta_{xy} = 1$ if $x = y$, $\delta_{xy} = 0$ if $x \neq y$. From (2.4) and (2.6) one can express components of the dielectric tensor. As $\omega_{pe} \gg \omega_{pi}$ here ion contribution can be neglected.

$$\hat{\epsilon} = \begin{bmatrix} 1 - \frac{\omega_{pe}^2}{\omega^2 - \omega_{ce}^2} & i \frac{\omega_{ce}}{\omega} \frac{\omega_{pe}^2}{\omega^2 - \omega_{ce}^2} & 0 \\ -i \frac{\omega_{ce}}{\omega} \frac{\omega_{pe}^2}{\omega^2 - \omega_{ce}^2} & 1 - \frac{\omega_{pe}^2}{\omega^2 - \omega_{ce}^2} & 0 \\ 0 & 0 & 1 - \frac{\omega_{pe}^2}{\omega^2} \end{bmatrix} \quad (2.7)$$

For tokamak plasmas the probing electromagnetic wave of reflectometer is directed usually perpendicular to magnetic field line direction. There are two polarization options (modes). First is ordinary mode (O-mode) with electric field parallel to the magnetic field direction and extraordinary mode (X-mode) with electric field directed

perpendicular to the magnetic field.

2.1.2 Ordinary mode (O-mode)

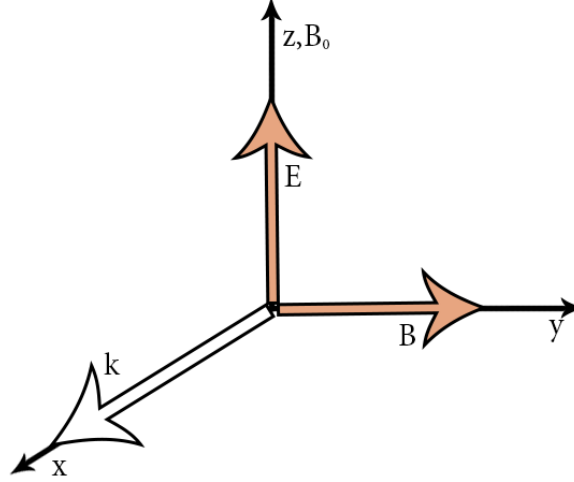


Figure 2.1: Ordinary mode wave components orientation, $E \parallel B_0$

In the case of ordinary mode, square of the refractive index is given by expression:

$$N^2 = 1 - \left(\frac{\omega_{pe}}{\omega}\right)^2 \quad (2.8)$$

This expression is the same as for plasmas without external magnetic field. It does not depend on magnetic field. This wave is linearly polarized with its electric field parallel to the external magnetic field and its magnetic field perpendicular to the external magnetic field. Such waves propagate inside the plasma when $\omega > \omega_{pe}$. With higher density when ω_{pe} reaches ω plasma wave encounters a cut-off and reflects. The density at which it happens is called the critical density or cut-off density:

$$n_c = \frac{m_e \epsilon_0 \omega^2}{e^2} \quad (2.9)$$

Using this expression, the refraction index formula can be rewritten:

$$N^2 = 1 - \frac{n}{n_c} \quad (2.10)$$

2.1.3 Extraordinary mode (X-mode)

Extraordinary mode has elliptical polarization with wave electric field vector \vec{E} directed in perpendicular direction to external magnetic field. Neglecting ion mobility, the

refraction index is given by next expression:

$$N_x^2 = 1 - \frac{\frac{\omega_{pe}^2}{\omega^2} \left(1 - \frac{\omega_{pe}^2}{\omega^2}\right)}{1 - \frac{\omega_{pe}^2}{\omega^2} - \frac{\omega_{ce}^2}{\omega^2}} \quad (2.11)$$

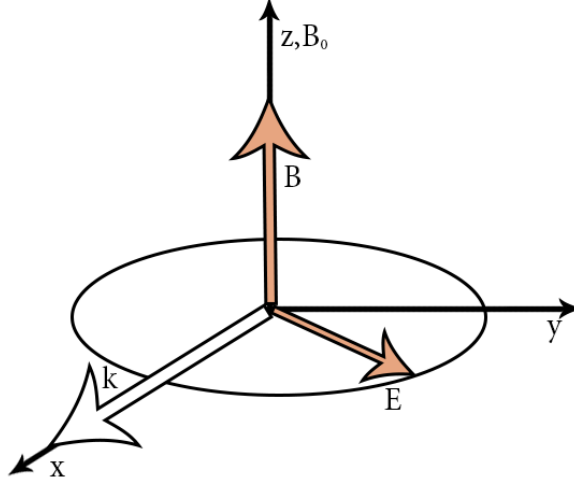


Figure 2.2: Extraordinary mode wave components orientation, $\vec{E} \perp \vec{B}_0$

As one can see propagation of extraordinary wave depends on both plasma density and magnetic field.

2.1.4 Electromagnetic wave cut-off and resonances

Cut-off positions:

When on the way, the wave refraction index approaches to zero, the wave slows down and reflects or makes a turn. For O-mode the cut-off position is where the wave frequency is equal to the plasma oscillation frequency.

$$\omega = \omega_{pe} \quad (2.12)$$

There is no energy loss during wave propagation when $\omega < \omega_{pe}$. Reflection or turn of the wave near $\omega \approx \omega_{pe}$ also occurs with energy conservation. Extraordinary wave has two cut-off frequencies which correspond to solutions of equation $N^2 = 0$.

$$\omega_L = \frac{1}{2} \left[\sqrt{\omega_{ce}^2 + 4\omega_{pe}^2} - \omega_{ce} \right] \quad (2.13)$$

$$\omega_H = \frac{1}{2} \left[\sqrt{\omega_{ce}^2 + 4\omega_{pe}^2} + \omega_{ce} \right] \quad (2.14)$$

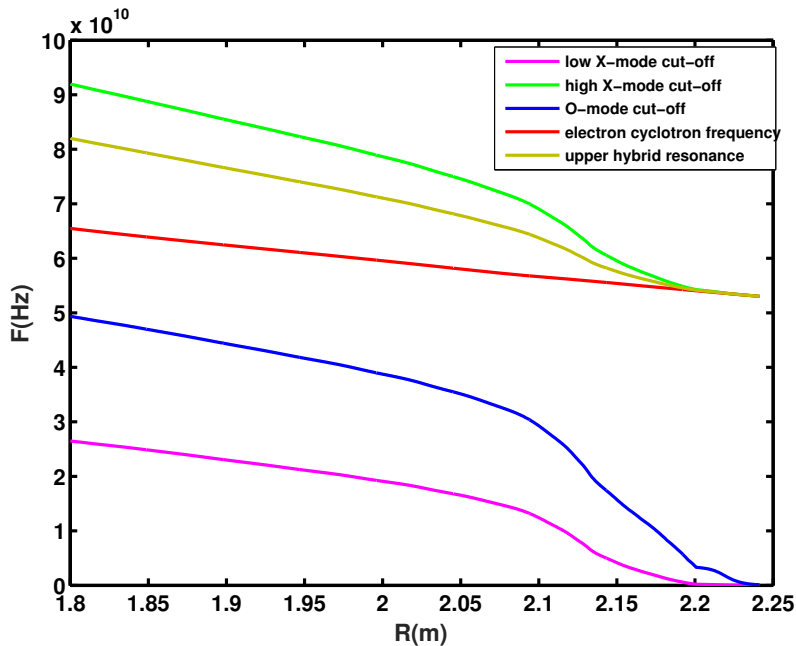


Figure 2.3: Magenta - low X-mode cut-off frequency; Green - high X-mode cut-off frequency; Blue - O-mode cut-off frequency; Red - electron cyclotron frequency; Yellow - upper hybrid resonance frequency. For ASDEX tokamak profiles ($B_{axes} = 2.5T$, $MAX(n_e) = 3 \cdot 10^{19}m^{-3}$), discharge number 31287

Resonance positions:

In some special conditions the denominator of the refractive index can become zero and its value can go to infinity. In this case phase velocity of the wave becomes close to zero and wave energy absorption takes place. Ordinary mode does not have resonances. However X-mode refractive index can become infinite and wave can be absorbed by upper hybrid resonance.

$$\omega_{UH}^2 = \omega_{pe}^2 + \omega_{ce}^2 \quad (2.15)$$

On figure 2.3 one can see an example of cut-off and resonance frequencies. These frequencies were computed for ASDEX tokamak L-mode profiles.

2.1.5 Wave propagation through inhomogeneous plasmas

In experimental setup such as tokamak, plasma density and magnetic field are not homogeneous along the electromagnetic beam trajectory. Toroidal magnetic field component is much stronger than the poloidal one. This field is produced by central solenoid and decreases with major radius as $1/R$. The plasma density and temperature are peaked in the plasma core and decrease towards the plasma edge [10]. As it is mentioned in section 1.2.3, often the toroidal plasma cross-section is not circular, but has elongation and triangularity. Such a configuration can lead to probing beam

deviation and reflection. As phase velocity of the beam is connected to the magnetic field and the plasma density, phase of the beam changes when it crosses the plasma. In next sections we will have a look on the basic principles of these processes.

2.1.6 Approximation of Wentzel-Kramer-Brillouin

In inhomogeneous plasmas the refraction index N depends on the position.

$$k^2 = w^2/c^2 \cdot N^2 = k_0^2 N^2 \quad (2.16)$$

If the variation of the refractive index is small over the wavelength Wentzel-Kramer-Brillouin (WKB) approximation can be applied. We will look for solution of the Helmholtz equation (2.18) in form of

$$E = E_0(r)e^{i\phi(r)}e^{i\omega t}. \quad (2.17)$$

More details about the Helmholtz equation can be found in further chapter (section 3.1).

$$\nabla^2 E + k^2(r)E = 0 \quad (2.18)$$

Using solution (2.17) equation (2.18) can be expressed as:

$$E_0'' - iE_0\phi'' - 2iE_0'\phi' + (k^2 - \phi'^2)E_0 = 0 \quad (2.19)$$

Under the assumption (2.17), the phase ϕ changes much faster than the amplitude E_0 and we can neglect second derivative of the amplitude E_0'' . To fulfil equation (2.19) imaginary and real part of left side should be equal to 0.

$$k^2 - \phi'^2 = 0 \Rightarrow \phi = \pm \int k(r)dr \quad (2.20)$$

$$E_0\phi'' - 2E_0'\phi' = 0 \Rightarrow E_0(r) = E_v/\sqrt{\phi'(r)} = E_v/\sqrt{k(r)} \quad (2.21)$$

Where E_v is the wave amplitude in the vacuum. Using last results together with expression (2.16) the total electric field can be expressed as

$$E = \frac{E_v}{\sqrt{N(r)}} e^{\pm ik_0 \int N(r)dr} e^{i\omega t} \quad (2.22)$$

Such expression is valid when $\|E_0''\|$ is much smaller than other components of equation (2.19). This is the case of geometrical optics approximation where the amplitude of the wave does not change much on the length of one local wave-length.

2.1.7 Wave propagation through a turbulent medium

Tokamak plasmas usually are very turbulent media. Density perturbations along the plasma profile cause wave scattering and change wave properties such as amplitude, phase and propagation direction. Scattering of the probing wave follows conservation law of energy and momentum:

$$\vec{k}_{scat} = \vec{k}_{inc} + \vec{k}_{turb} \quad (2.23)$$

$$\vec{\omega}_{scat} = \vec{\omega}_{inc} + \vec{\omega}_{turb} \quad (2.24)$$

Here subscription *scat* refers to scattered wave, *inc* - to incident wave, *turb* to turbulence wave. k is the wave-length and ω is the wave circular frequency. Relations (2.23,2.24) are called Bragg resonance rule. In stationary case $|k_{inc}| = |k_{scat}|$, we can find a relation for the scattering angle figure 2.4.

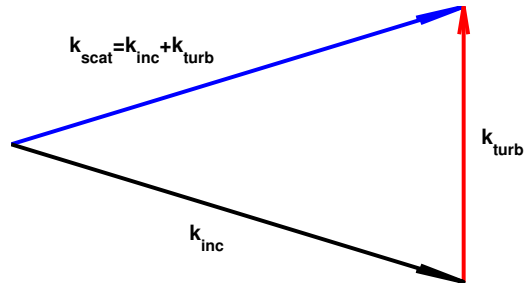


Figure 2.4: Bragg scattering rule illustration. k_{scat} - wave-number of the scattered wave, k_{inc} - wave-number of the incident wave, k_{turb} - wave-number of the turbulence

Usually most of the reflectometer signal comes from backscattering when vectors \vec{k}_{scat} and \vec{k}_{inc} are collinear. In this case expression 2.23 can be simplified as $k_{scat} = \frac{1}{2}k_{turb}$

2.1.8 Mathieu equation

To explain the observations done during the simulations presented in next chapters especially second peak in the wave number spectrum, now we will briefly present basics of Mathieu equation formalism. Let us consider one dimensional stationary wave which follows solution of Helmholtz equation (3.4). If fluctuations of plasma density or magnetic field are present, the wave refractive index is also perturbed. To investigate how each wave-number of the turbulence interacts with the probing wave, we will

consider monochromatic perturbation with amplitude envelop centred in x_f .

$$N^2 = 1 - \frac{\omega_{pe}^2}{\omega^2} = 1 - \frac{n_0}{n_c} - \frac{\delta n}{n_c} \cos(k_f(x - x_f - d_f)) \quad (2.25)$$

Where d_f is the semi length of the envelop and a_f is the envelop amplitude. We will make the assumption that inside turbulence amplitude envelop $[x \in [x_f - d_f, x_f + d_f]]$ the plasma is homogeneous. This assumption is justified by Floquet theorem. Now Helmholtz equation can be reduced to Mathieu equation [42, 43]:

$$\frac{d^2 E}{d\xi^2} + (p - 2q \cos 2\xi)E = 0 \quad (2.26)$$

Where $\xi = \frac{\pi}{4} - \frac{1}{2}k_f(x - x_f - d_f)$, p describes position and in some sense the relation between local wave-number and turbulence wave number, q represents perturbation amplitude. Solution stability of Mathieu equation in a plane of p, q can be expressed by infinite progression of functions $a_i(q)$ and $b_i(q)$. This functions can be expressed in different ways [44] [45]. $a_i < p < b_{i+1}$:stable solution

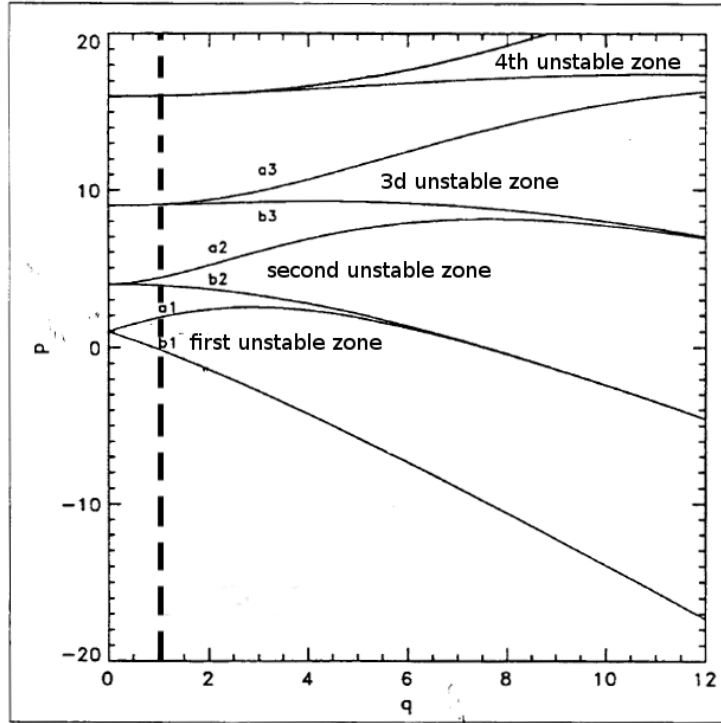


Figure 2.5: Mathieu equation solution stability areas. $a_i < p < b_{i+1}$:stable solution, $b_i < p < a_i$:unstable solution. Figure source [42]

$b_i < p < a_i$:unstable solution

Unstable solution zones are able to trigger Bragg back-scattering process. On figure 2.5

one can find stable and unstable zones of Mathieu equation. Expressions for variables p and q for ordinary and extraordinary modes can be found in [42]. Small turbulence level corresponds to $q \approx 0$, in this case only one unstable solution can be reached it represents normal Bragg scattering condition. With higher turbulence amplitude (increase of q value) more high q unstable zones start to be active.

2.2 Reflectometer description

2.2.1 Reflectometry basic principle

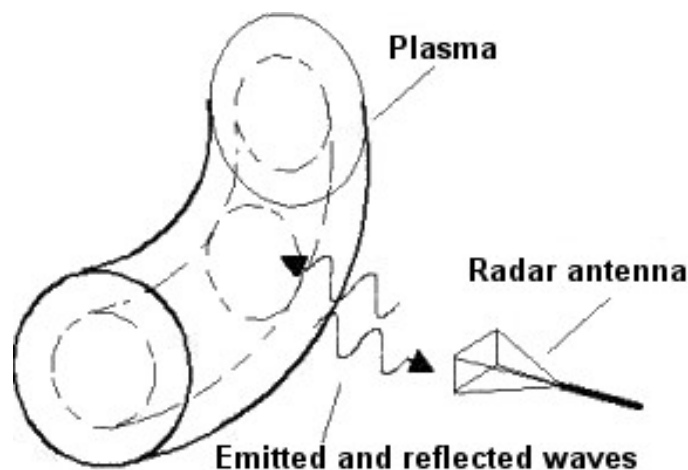


Figure 2.6: Basic reflectometer radar principle technique. Image source [46]

In the reality of complex geometry which leads to limited space for diagnostics, it is very important to have good plasma density profile and plasma position measurement tools as well as a plasma turbulence diagnostic tool which is compact and accurate. Plasma microwave reflectometry uses very small vacuum chamber port with one or two small antennas. This diagnostic is based on a radar technique where ordinary or extraordinary electromagnetic wave is launched into the plasma with a frequency that permits to have a cut-off layer with a reflection like from a mirror [47] [48]. It uses ultra fast frequency swept signal which allows to scan the density profile with a time scale which is much smaller than the plasma turbulence correlation time. After the reflection, the wave goes out of the plasma and gets received by a receiving antenna. Along the way through the plasma the electromagnetic wave gain an additional phase ϕ and time delay. Based on WKB (see section 2.1.6) approximation, Bottollier-Curtet technique [49, 50] allows us to rebuild density profile. However plasma turbulence perturbs density profile and to measure plasma density profile one have to make an average of the UFSR phase, which is assumed to be WKB phase. Moreover reflectometer phase fluctuations after

removal of the phase average can give an information about turbulence wave-number spectrum (see equation(2.27)).

$$\phi = \langle \phi \rangle + \delta\phi \quad (2.27)$$

Measurements can be done from the low field side(LFS) and high field side(HFS) with both "X" and "O" modes. Almost zero cut-off frequencies near the plasma edge make O-mode reflectometry inapplicable for plasma edge density measurements. If magnetic field is very high especially on HFS X-mode cut off frequency can become very high, and measurements are difficult due to reflectometry hardware limitations. Depending on magnetic field strength, small density region in HFS can not be reachable because of upper hybrid resonance.

In Ultra-Fast Swept Frequency Reflectometry(USFR) the phase that the probing beam gains due to the plasma density and magnetic field is not measured directly. To give an example of beam phase calculation let us assume that probing wave frequency is changing in time as:

$$F(t) = f_0 + v_f \cdot t \quad (2.28)$$

Where $v_f[GHz/ms]$ is the frequency sweep speed. In this case the initial signal phase looks like:

$$\phi_0(t) = 2\pi f_0 t + \frac{2\pi v_f t^2}{2} \quad (2.29)$$

Then reflected from the plasma, the signal phase can be expressed as:

$$\phi_r(t) = 2\pi f_0 t + \frac{2\pi v_f t^2}{2} + \phi_{vacuum}(t) + \phi(t) \quad (2.30)$$

Here ϕ_{vacuum} is the phase gained in the vacuum region and transmission lines. In a basic experimental setup initial signal $A_0 \cos(\phi_0)$ is split and part of it is transited avoiding plasma. Then this signal goes to a multiplier and is mixed with reflected signal $I_0 = A_r \cos(\phi_r)$

$$A_0 A_r \cos(\phi_0) \cos(\phi_r) = \frac{A_0 A_r}{2} [\cos(4\pi f_0 t + 2\pi v_f t^2 + 2\phi_{vacuum}(t) + \phi(t)) + \cos(\phi + \phi_{vacuum})] \quad (2.31)$$

Filtering out high frequency signal one can obtain $A_0 A_r \cos(\phi + \phi_{vacuum})$ where A_r is a received beam amplitude and ϕ is a phase obtained due to propagation through the plasma. This phase observed as beating frequency signal $\phi = F_b t$, where F_b is a beating frequency.

Such a system with single frequency is called homodyne detection. Using this method it is impossible to calculate simultaneously amplitude and phase of the reflectometer

signal without certain assumptions.

2.2.2 Homodyne IQ detection

To determine signal phase and amplitude separately, IQ detection technique can be used. Reflectometer reference signal split on 2 parts and $\pi/2$ phase is introduced to one of the parts. These reference parts can be expressed as:

$$I^s = A_0 \sin(\phi_{ref}) \quad (2.32)$$

$$I^c = A_0 \cos(\phi_{ref}) \quad (2.33)$$

The signal reflected from the plasma (I_{ref}) is then multiplied with both I^s and I^c .

$$I_{ref}^s \cdot I_0 = \frac{1}{2} A_{ref} A_0 [\sin(\phi_{ref} + \phi_0) + \sin(\phi_{ref} - \phi_0)] \quad (2.34)$$

$$I_{ref}^c \cdot I_0 = \frac{1}{2} A_{ref} A_0 [\cos(\phi_{ref} + \phi_0) + \cos(\phi_{ref} - \phi_0)] \quad (2.35)$$

Both resulting signals can be processed to filter high frequency part($\phi_{ref} + \phi_0$). This permits to get real and complex parts of the signal(IQ):

$$\frac{1}{2} A_0 \Re(I) = \frac{1}{2} A_{ref} A_0 \cos(\phi) \quad (2.36)$$

$$\frac{1}{2} A_0 \Im(I) = \frac{1}{2} A_{ref} A_0 \sin(\phi) \quad (2.37)$$

Signal amplitude and phase can be calculated as:

$$A_{ref} = \sqrt{\Re^2(I) + \Im^2(I)} \quad (2.38)$$

$$\phi = \arctan(\Im(I)/\Re(I))$$

This method allows us to calculate amplitude and phase separately. Homodyne swept frequency reflectometry was widely used in the past on various tokamaks such as JET [51], ASDEX [52], TFTR [53] and others.

Swept signal sources always have relatively strong phase noise. Because of this, to extract phase from small beating frequency one will face low signal-noise ratio.

2.2.3 Heterodyne IQ detection

Signal to noise ratio can be improved using heterodyne system. Heterodyne system was first applied to Russian T-10 tokamak [54]. This system is based on 2 signal

sources with different frequencies. The probing signal is modulated with low frequency oscillator (F_m). Then the same procedure which was highlighted in previous section is applied and the resulting signal has frequency $F_b + F_m$. With the increase of frequency, the signal to noise ratio improves [55]. At a final step, modulation frequency used to get imaginary and real parts of IQ signal.

Usually in tokamak, turbulence is stronger near the edge. This turbulence can lead to back scattering on the probing wave. With a frequency sweeping this backscattered part of the probing wave can be received earlier than the part reflected at the cut-off position. Part of the wave also can be trapped between cut-off and edge turbulence. These fields mix together with noise make IQ detection method inapplicable without special filtering [56]. Example of time of flight spectrogram is shown on figure 2.7. Filtering of the signal can change the reflectometer phase response which is crucial for turbulent wave-number spectra reconstruction.

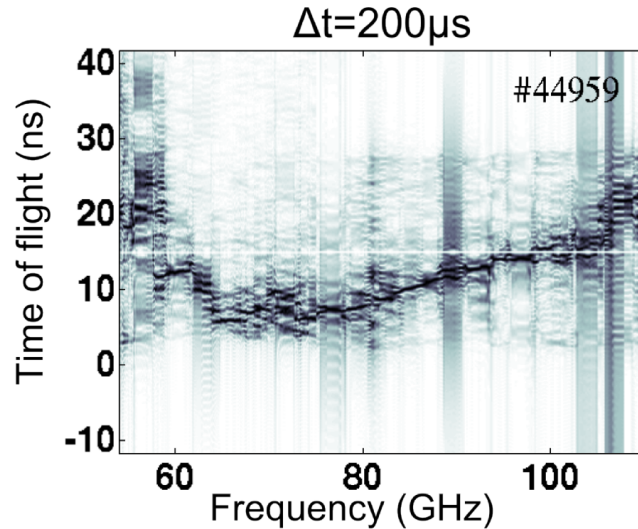


Figure 2.7: time of flight spectrogram for Tore-Supra discharge (shot 44959) with strong backscattering. Source of the picture: [57]

2.2.4 Other reflectometry types

Beside UFSR there are other types of reflectometry able to provide information on plasma turbulence and plasma density profile [47, 58].

Short pulse reflectometry: instead of fast frequency sweep it uses short pulse ($t \approx 1 ns$) [59, 60]. Using such a technique one can avoid phase description of reflectometer signal. Time of flight is measured directly. However reflection before cut-off and multi-reflection in this case are also able to affect of measurements.

Fixed frequency normal incidence reflectometry: uses fixed frequency to measure signal variation in time. With frequency one can fix the cut-off position. Under the assumption that the reflectometer signal relies on cut-off vicinity frequency spectra and signal time coherency can be measured [61]. Using multiple frequencies simultaneously one can also extract turbulence radial correlation length [62].

Doppler reflectometry: beam directed not perpendicular to the cut-off layer, resulting in ray makes turn instead of cut-off [63,64]. Using ray-tracing codes it is possible to evaluate position of turning point and local probing wave-number. Assuming that the main part of the signal comes from the turning point it is possible to measure frequency spectra, which can be used to calculate poloidal plasma rotation of certain wave-number. Tilting the antenna angle it is possible to change probing wave-number at the turning point and by doing this scan turbulence wave-number spectra. [65].

Poloidal correlation reflectometry: This type of reflectometer uses several poloidally displaced receiving antennas and single emitting antenna. This enables to associate the signal received by each antenna with a certain poloidal angle. Correlation between signals of different antennas can give an information on poloidal plasma rotation and turbulence correlation time [66,67].

Imaging reflectometry: instead of receiving antenna one can use an array of antennas closely distributed in a relatively small area [68,69]. Each receiving antenna from this array is associated with a certain position in the plasma. With such a configuration one can get 2D turbulence profile. However due to poor signal localization and non-linear effects, resolution of such a system is not very high.

2.3 Closed loop algorithm

Reflectometer signal processing to extract plasma properties is very tricky. With help of synthetic diagnostics such as full-wave codes or reduced models it is possible to calculate reflectometer response for given plasma parameters. However to link reflectometer phase variation power spectrum to density variation power spectrum inverse problem should be solved. To introduce algorithm to solve this problem let's make the assumption that reflectometer signal phase power spectra obtained from area near coordinate R_0 depends only on turbulence near R_0 . Under this assumption we can introduce power spectra transfer function:

$$S_{\delta n}^{pow}(\vec{r}, t) = S_{\delta \phi}^{pow}(\vec{r}, t) \cdot Tr(S_{\delta n}^{pow}(\vec{r}, t)) \quad (2.39)$$

Where $S_{\delta n}^{pow}$ is the density perturbations power spectrum, $S_{\delta \phi}^{pow}$ - is the swept reflectometer phase power spectrum, and Tr is the transfer function. In case of Born approx-

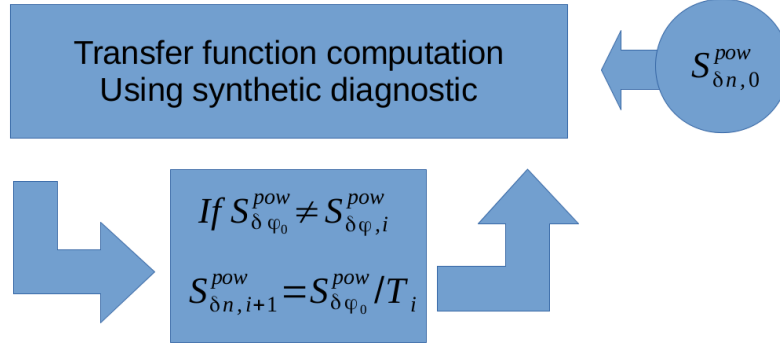


Figure 2.8: Closed loop algorithm diagram. Experimental parameters together with assumed turbulence power spectrum $S_{\delta n,0}^{pow} = |S_{\delta n,0}|^2$ processed with synthetic diagnostic. Transfer function $Tr_i = S_{\delta n,i}^{pow} / S_{\delta \phi,i}^{pow}$ is computed and applied to experimental phase power spectrum $S_{\delta n,i+1}^{pow} = S_{\delta \phi_0}^{pow} \cdot Tr_i$. Then synthetic diagnostic is used again and full circle repeats until $S_{\delta \phi,i}^{pow} = S_{\delta \phi_0}^{pow}$

imation which is valid when turbulence is weak, transfer function Tr does not depend on turbulence spectrum and can be expressed with analytical expression [70]. However when turbulence root mean square level reaches a few % from cut-off density, phase behaviour becomes not linear and in this case transfer function Tr should depend also on turbulence power spectrum. Transfer function can be found using so called closed loop algorithm [71]. Algorithm diagram is illustrated on figure 2.8. Closed loop algorithm uses synthetic diagnostic for direct problem solution. Experimental density profile and assumed density turbulence with power spectrum $S_{\delta n,0}^{pow}$ are used in synthetic diagnostic computation. Then using computation result and experimental data transfer function can be computed $Tr_0 = S_{\delta n,0}^{pow} / S_{\delta \phi,0}^{pow}$. After it can be applied to experimental data to generate new turbulence $S_{\delta n,i+1}^{pow} = S_{\delta \phi_0}^{pow} \cdot Tr_i$. This action should be repeated until computation result will match experimental data. As synthetic diagnostic 1D [41, 42], 2D or 3D [65, 72] full wave codes can be used as well as simplified models [73]. Under our current assumption we can replace real inhomogeneous turbulence by turbulence with same spectrum and amplitude all over the density profile. This assumption gives very good convergence of the method [71]. However it is not very realistic in fusion plasmas. For more realistic description of the turbulence one can make turbulence level inhomogeneous. Moreover recent studies were made using fully inhomogeneous turbulence [56]. Method does not guaranty good convergence and unique stable solution. In this work we will focus on synthetic diagnostics and we will study in more details different turbulence observation regimes and look on changes of the reflectometer signal due to strong turbulence that possibly will affect closed loop interpretation results.

Chapter 3

Reflectometer response computation methods

In this section I will highlight the computation methods which will be used in the rest of the thesis work. Here we will speak about numerical and analytical solutions.

3.1 Helmholtz equation

Let us look on Maxwellian equations for the harmonic solution $E = E_\omega(x, \omega)e^{-i\omega t}$

$$\begin{cases} \text{rot}\vec{E}_\omega = i\omega\mu_0\vec{H}_\omega \\ \text{rot}\vec{H}_\omega = \vec{J}_\omega - i\omega\epsilon_0\vec{E}_\omega \end{cases} \quad (3.1)$$

We will apply *rot* on the first equations (3.1).

$$\text{rot}(\text{rot}\vec{E}_\omega) = i\omega\mu_0\text{rot}\vec{H}_\omega \quad (3.2)$$

Plasma current \vec{J}_ω can be expressed through conductivity $\vec{J}_\omega = \hat{\sigma}\vec{E}_\omega$. Using expression " $\text{rot}(\text{rot}X) = \text{grad}(\text{div}X) - \Delta X$ " and replacing $\text{rot}\vec{H}_\omega$ in the right parts of the original Maxwell's expression we get:

$$-\Delta\vec{E}_\omega = \frac{\omega^2}{c^2}\left(1 - \frac{\hat{\sigma}}{i\omega\epsilon_0}\right)\vec{E}_\omega \quad (3.3)$$

In this expression we use only the diagonal components of the tensor σ (2.5). Using expression (2.6) we obtain:

$$\Delta\vec{E}_\omega + \vec{k}\vec{E}_\omega = 0 \quad (3.4)$$

This expression is called Helmholtz equation. Using this expression it is possible to calculate the reflectometer probing beam stationary field distribution. However to calculate reflectometer phase responses, the incident field should be removed (see section 2.2.1). To make it in 2D, special boundary condition method should be used [74]. In 1D, the solution becomes much simpler. In the case of full reflection, the incident and the reflected waves have the same amplitude and the solution takes the form of a standing wave.

$$\cos(\omega t + kx) + \cos(-\omega t + kx + \phi_0 + \delta\phi) = 2 \cos(kx + \frac{\phi_0}{2} + \frac{\delta\phi}{2}) \cos(\omega t + \frac{\phi_0}{2} + \frac{\delta\phi}{2}) \quad (3.5)$$

Here ϕ_0 is the received field phase obtained without turbulence, $\delta\phi$ is defined by turbulence. As we see in expression (3.5) phase computed from standing wave zero position using Helmholtz equation equals to half of the phase measured in an experiment. As we will show in section 3.4 the stationary solution can be different from the time dependent one. Moreover in experimental data analysis (section 2.2.3) for one to be able to track the phase beating frequency, the spectrum should be filtered to have only the main reflection taken into account (no multi-reflections) [75,76]. And after filtering also wave scattering from the edge does not have direct influence on the received signal. But in some cases, for example when the edge turbulence level is much higher than the core one, scattering from the plasma edge can dominate. We will look more closely on this problem in next sections.

3.2 Solution of 1D Helmholtz equation

One dimensional form of this equation is widely used for reflectometry simulation and data analysis. Developed numerical methods allow to compute the electric field distribution very fast and with very good accuracy. Next we will closer look on the precision on the Numerov's method (3.4).

3.2.1 4th Order Numerov's method for Helmholtz equation

Using Numerov's method [41] it is possible to rewrite one dimensional Helmholtz equation (3.4) as a 4th order discretized differential scheme.

$$\Lambda = (1 + \frac{h^2}{12} \frac{d^2}{dx^2}) \quad (3.6)$$

With Numerov's method, operator Λ (3.6) will be applied on the Helmholtz equation (3.4).

$$\left(1 + \frac{h^2}{12} \frac{d^2}{dr^2}\right) \frac{d_z^E(r)}{dr^2} + 4\pi N_0^2(r) E_z(r) + \frac{h^2}{12} \frac{d^2}{dx^2} (4\pi N_0^2(r) E_z(r)) = 0 \quad (3.7)$$

Here we got discrete differential scheme of 4th order.

$$E_z(r_i + h)C_i + E_z(r_i - h)A_i + E_z(r_i)B_i = 0 \quad (3.8)$$

Where $A_i = (1 + 4\pi^2 \frac{h^2}{12} N_0^2(r_i - h))$, $B_i = (2 - 4\pi^2 \frac{5h^2}{6} N_0^2(r_i))$, and $C_i = (1 + 4\pi^2 \frac{h^2}{12} N_0^2(r_i + h))$ 1D Helmholtz equation can be rewritten as system of linear equations

$$\begin{bmatrix} B_1 & C_1 & 0 & \dots & 0 \\ A_2 & B_2 & C_2 & \dots & \vdots \\ 0 & \ddots & \ddots & \ddots & 0 \\ \vdots & \dots & A_{N-1} & B_{N-1} & C_{N-1} \\ 0 & \dots & 0 & A_N & B_N \end{bmatrix} \begin{bmatrix} E_1 \\ E_2 \\ \vdots \\ E_{N-1} \\ E_N \end{bmatrix} = \begin{bmatrix} D_1 \\ D_2 \\ \vdots \\ D_{N-1} \\ D_N \end{bmatrix} \quad (3.9)$$

Where vector D is defined by boundary conditions.

3.2.2 Electric field amplification phenomena

To find limitations of the Numerov's numerical scheme for Helmholtz equation we will use special electron density profile with several cut-off positions, for which exact solutions can be written. In these special conditions big amplification of the electric field can take place, as illustrated in the following example. Although such a density profile is not very realistic, this example is very good for verification of the computation method.

Refractive index of the ordinary wave is given by:

$$N^2 = 1 - \frac{n(x)}{n_c} \quad (3.10)$$

Where $n(x)$ is the plasma electron density, and n_c is the critical density. To analyze resonance solution with extreme field amplification we will look at the simplest case with analytical solution of the 1D Helmholtz equation.

$$\begin{cases} n(x) = \frac{L-x}{L} n_c + n_0 : & x < x_0 \\ n(x) = \frac{L-x}{L} n_c : & x \geq x_0 \end{cases} \quad (3.11)$$

Here L is the distance from cut-off position to plasma edge. This density profile is

not very realistic. Square of refractive index is depicted on figure 3.2. One can find information on wave amplitude amplification in more realistic cases [77]. In this case to get exact solution we need to divide the space in two areas. First $x < x_0$ and $x > x_0$. Amplitude of electric field in these regions can be expressed as

$$\begin{cases} E = A_1 Ai(\tilde{\eta}) + B_1 Bi(\tilde{\eta}) : & x < x_0 \\ E = A_2 Ai(\eta) : & x \geq x_0 \end{cases} \quad (3.12)$$

Where Ai and Bi are first and second Airy functions, and η is a normalized radius:

$$\eta = (k_0 L)^{2/3} x / L; \tilde{\eta} = (k_0 L)^{2/3} (x + \frac{L n_0}{n}) / L \quad (3.13)$$

To find constants A_1 and A_2 we will use properties of the electromagnetic wave structure such as continuity of the electric field value and its derivative. These values should be connected near x_{max} .

$$\begin{cases} A_1 Ai(\tilde{\eta}_0) + B_1 Bi(\tilde{\eta}_0) = A_2 Ai(\eta_0) \\ A_2 Ai'(\tilde{\eta}_0) + B_1 Bi'(\tilde{\eta}_0) = A_2 Ai'(\eta_0) \\ A_2 = 1 \end{cases} \quad (3.14)$$

With $\eta_0 = \eta(x_0)$, $\tilde{\eta}_0 = \tilde{\eta}(x_0)$, and $Ai' = \frac{dAi}{dx}$. In order to find analytical solution we have fixed parameter $A_2 = 1$. From system (3.14) we can express coefficient A_1 and B_1 .

$$\begin{cases} A_1 = \frac{Ai'(\eta_0) Bi(\tilde{\eta}_0) - Ai(\eta_0) Bi'(\tilde{\eta}_0)}{Ai'(\tilde{\eta}_0) Bi(\tilde{\eta}_0) - Ai(\tilde{\eta}_0) Bi'(\tilde{\eta}_0)} \\ B_1 = \frac{Ai'(\eta_0) Ai(\tilde{\eta}_0) - Ai(\eta_0) Ai'(\tilde{\eta}_0)}{Bi'(\tilde{\eta}_0) Ai(\tilde{\eta}_0) - Bi(\tilde{\eta}_0) Ai'(\tilde{\eta}_0)} \end{cases} \quad (3.15)$$

In the vacuum region the total field can be expressed through incident and reflected waves similar to expression (3.16).

$$E_{tot} = E_{in} \cos(kx) + E_{out} \cos(kx + \phi_0 + \delta\phi) \quad (3.16)$$

As we do not have any wave energy absorption, then E_{in} here is equal to E_{out} .

$$E_{tot} = E_{in} \cos(kx + \phi_0/2 + \delta\phi/2) \cos(\phi_0/2 + \delta\phi/2) \quad (3.17)$$

This means that solving Helmholtz equation does not allow to separate incident and reflected waves. But phase difference can be calculated from the total field distribution. To study field amplification effect we will use field amplification coefficient computed as ratio of the electric field amplitude coefficient A_2 and amplitude of the total field in

the vacuum region. Far from the cut-off area ($\eta < -1$) the Airy function solution can be expressed with asymptotic formula:

$$Ai(\eta) = \frac{1}{\sqrt{\pi}z^{1/4}} \sin\left(\frac{3}{2}\eta^{3/2} + \pi/4\right); Bi(\eta) = \frac{1}{\sqrt{\pi}z^{1/4}} \cos\left(\frac{3}{2}\eta^{3/2} + \pi/4\right) \quad (3.18)$$

Using this (3.18) expression we can find the total field in the vacuum region.

$$A_1 Ai(\eta) + B_1 Bi(\eta) = \frac{\sqrt{A_1^2 + B_1^2}}{\sqrt{\pi}(k_0 L)^{1/6}} \cos\left(\arctan(A_1/B_1) - \frac{3}{2}\eta^{3/2} - \pi/4\right) \quad (3.19)$$

One can see that field amplitude in the vacuum region is equal to $A_0 = \frac{\sqrt{A_1^2 + B_1^2}}{\sqrt{\pi}(k_0 L)^{1/6}}$. And the amplification factor:

$$\gamma = A_2/A_0 = \left(\frac{\sqrt{A_1^2 + B_1^2}}{\sqrt{\pi}(k_0 L)^{1/6}}\right)^{-1} \quad (3.20)$$

Figure 3.1 shows an example of the amplification factor variation (blue line) with the density discontinuity position. This example was computed using $L = 200\lambda$ and $n_0/n_c = 5\%$. One can notice that the amplification factor has a few resonance peaks. First one is very narrow fundamental resonance peak. On figure 3.1 it does not reach its maximum due to insufficient numerical resolution. With the increase of resonance cavity, the size peaks become smaller and wider. After $x_0 < -10\lambda$ there is no second cut-off any more and amplification factor fluctuations comes only from the interplay between ongoing and outgoing waves with changing phase relation between them. On the same figure 3.1 the resonance phase variation term $\arctan(A_1/B_1)$ is depicted. One can see that when resonance is reached phase jumps of π take place. With increase on resonance peak order, the phase jump become smoother. After $x_0 < -10\lambda$ the phase jump amplitude start to decrease. On figure 3.2 one can see an example of the electric field structure together with the used N^2 profile. Here $x_0 = -6.16\lambda$. This corresponds to positions in the second resonance peak vicinity.

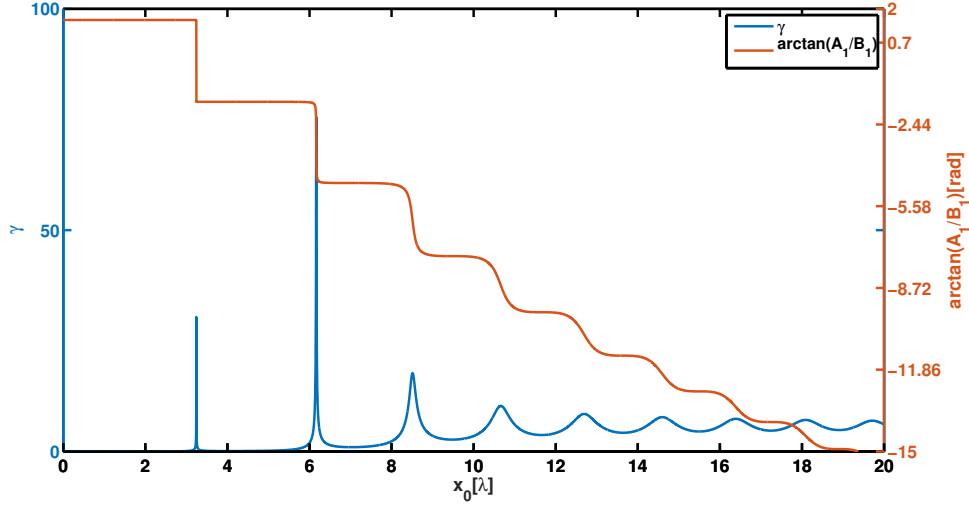


Figure 3.1: Electric field amplification factor γ as a function of density discontinuity position (blue), resonance phase variation term $\arctan(A_1/B_1)$ (orange)

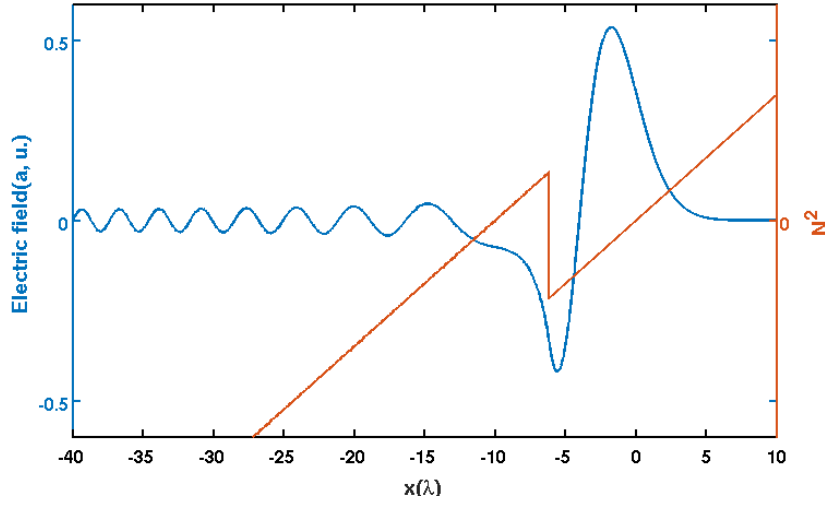


Figure 3.2: Electric field (blue), Square of the refractive index (orange)

3.2.3 Numerical precision of the Numerov's method in the case of strong electric field amplification

The case with single cavity represents an easy explanation of the field amplification phenomena. However for comparison with numerical solution we will use a plasma density profile with square gap near the cut-off region.

$$\begin{cases} n(x) = \frac{L-x}{L}n_c + n_0 : & x \in [x_{min}; x_{max}] \\ n(x) = \frac{L-x}{L}n_c : & x \in (-\infty; x_{min}) \cup (x_{max}; +\infty) \end{cases} \quad (3.21)$$

Here x_{min} and x_{max} are start and end positions of the density jump and n_0 is amplitude of the jump. Solution of this equation is the superposition of Airy functions. If we divide the space into 3 areas, each of them will have analytical solution with unknown coefficients.

$$\begin{cases} E = A_1 Ai(\eta) + B_1 Ai(\eta) : & x < x_{min} \\ E = A_2 Ai(\tilde{\eta}) + B_2 Bi(\tilde{\eta}) : & x \in [x_{min}; x_{max}] \\ E = A_3 Ai(\eta) : & x > x_{max} \end{cases} \quad (3.22)$$

η and $\tilde{\eta}$ can be found in expression (3.13). By solving the system of equations (3.22) which connects values and derivatives of electric field E near x_{min} and x_{max} one can calculate coefficients A_1, B_1, A_2, B_2 . And in order to find a solution, we will fix $A_3 = 1$. For electric field amplification factor we will use same expression (3.20) as in previous section. For comparison this coefficient can be also computed using numerical Helmholtz equation solution with Numerov's method.

Comparing exact and numerical solutions, we have found that near the resonance, amplification factors behave differently. Resonance positions are also not the same (Figure 3.3). These peaks correspond to the resonance at the fundamental cavity

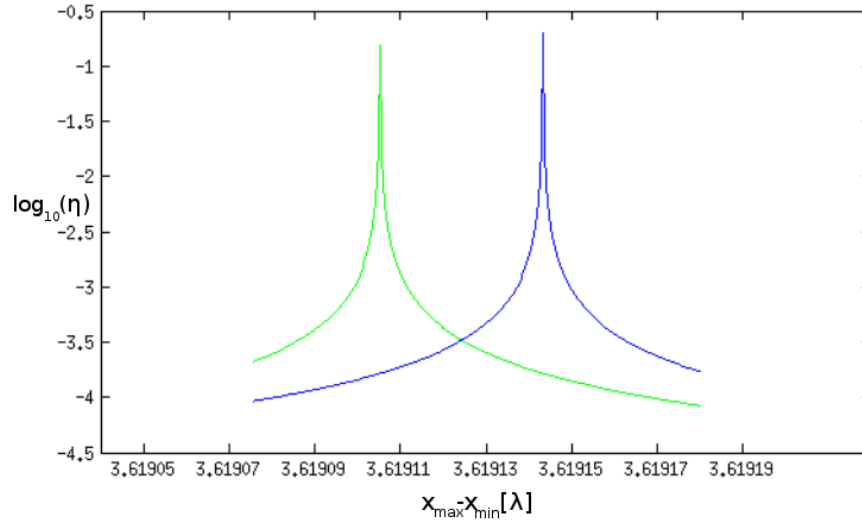


Figure 3.3: Amplification factor computed with numerical solution (blue), and exact solution (green)

mode. To avoid difference in computation while moving density jump we have fixed the discontinuity positions in the computation grid. After that we can change the length of the resonator (resonant cavity) by moving the cut-off position without moving the jump over the computational grid. That process is equivalent to changing the wave frequency. Difference in resonance positions is connected to the discontinuity in N^2 , while solving Helmholtz equation with Numerov's method. To avoid these kinds of

errors additional methods like domain decomposition method [78] can be applied, but this is beyond the scope of this work. It was found that one can minimize this resonant peak shift by adding extra points on density jump and put x_{min} and x_{max} between computational points, see figure 3.4. In this computation we will have a look and

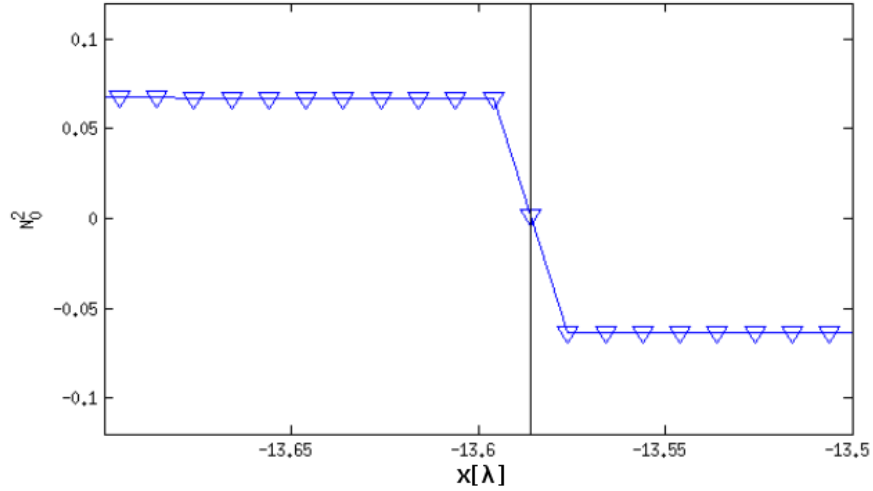


Figure 3.4: Square of the refractive index in the discontinuity vicinity. Blue triangles are computational points

compare maximum of the field amplification factor in fundamental resonance state as function of n_0 . Figure 3.5 shows the result of such computation for $n_0/n_c = 0.15$. Here the difference in resonance positions is $4 \cdot 10^{-5}\lambda$. Unfortunately, at very high electric

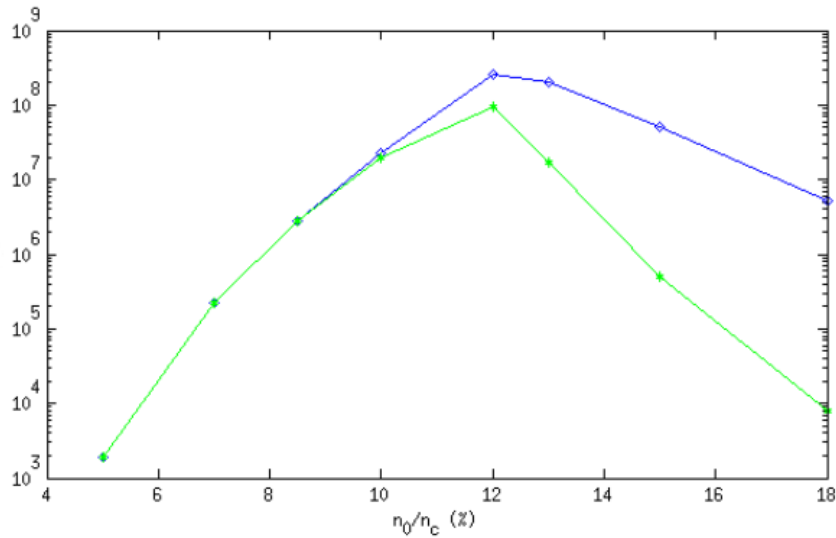


Figure 3.5: Amplification factor γ as function of density jump amplitude n_0 . Blue is the numerical solution and green is the exact one

field amplification level both numerical and exact solution saturate (stop growing).

With growth of density jump amplitude, the fundamental resonance peak becomes more narrow. And double precision for the cavity position is not enough to reach maximum of the electric field amplification factor (see figure 3.6). However we see

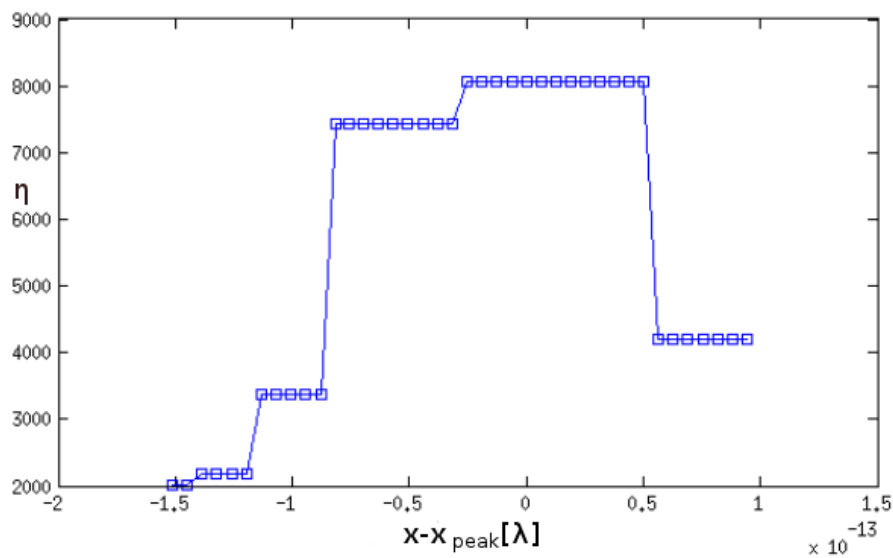


Figure 3.6: Amplification factor γ as function of cavity size close to fundamental resonance

that numerical and exact solutions are in very good agreement when $n_0/n_c < 6 - 7\%$. This value corresponds to electric field amplification factor $\gamma \approx 3 \cdot 10^6$. This means that even in extreme conditions Helmholtz equation solution has very good precision. On the figure 3.6 one can see detailed picture of the peak. Due to very small step of the density cavity size which is close to computational precision it is not possible to reproduce accurately the resonance peak. As one can see on figure 3.5 the exact solution for amplification factor saturates even faster than the numerical solution. Here we can conclude that 1D Numerov's Helmholtz solver has a very good precision even in very extreme conditions.

3.2.4 Numerical precision of the Numerov's method with noisy density profile

The same field amplification phenomena can be seen when noise is added onto the density profile. With noise, the resonance does not disappear but becomes stronger. Figure 3.7 represents the electric field propagating in a steady state noisy (white noise) plasma fulfilling resonant conditions, which are extremely narrow. A numerical precision of 13 digits is required to requires to determine 13 digits to reach these resonant conditions. To avoid negative densities the noise is contained in an appropriate enve-

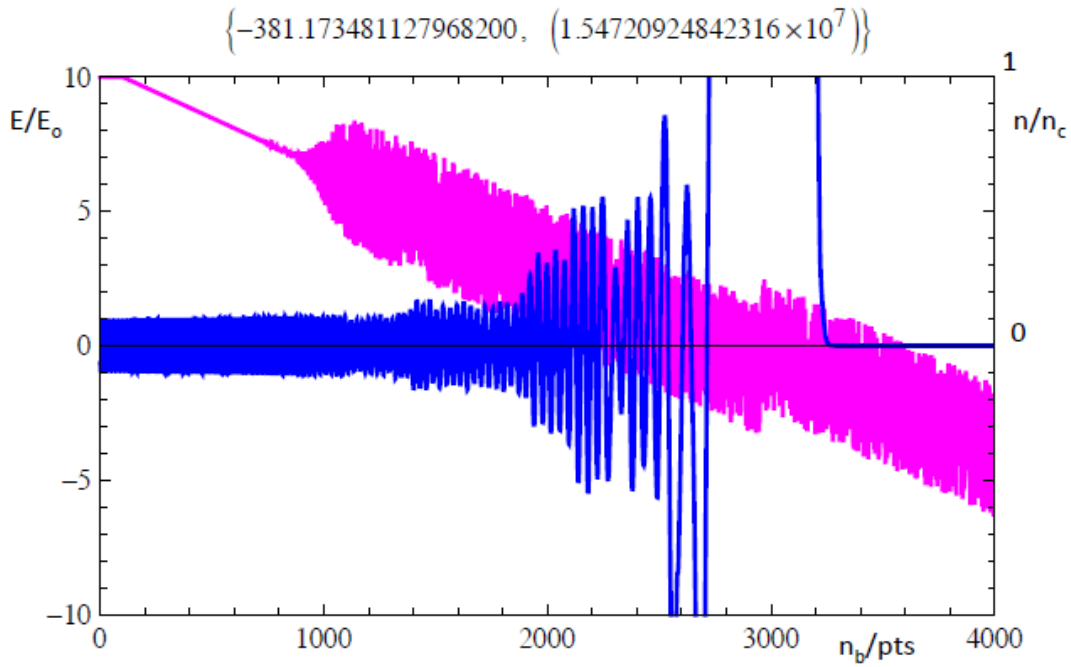


Figure 3.7: Spatial evolution of the plasma density and electric field when the maximum of the resonance is reached. The spatial coordinate is expressed in points where 20 points corresponds to a vacuum wavelength. The density gradient length is equal to 145 vacuum wavelengths and the amplification factor of the electric field is $1.55 \cdot 10^7$

lope. Amplification of the resonance peak due to the noise is depicted on figure 3.8. One can see on figure 3.8 that starting from amplitude of noise near 17% and amplification factor above $1.55 \cdot 10^7$ numerical error starts to play a big role. For accurate calculations in this region extended precision is needed. Role of the extended precision is illustrated in figure 3.9 for which the amplification factor is normalized. Effects of the lack of numerical accuracy due to the finite precision (here double precision) are shown on figure 3.10 and compared to 50 digits precision results figure 3.11. There is an exponential behaviour of the amplification factor with noise level under 20%, and after saturation starts to play a role. With further increase of the noise level, strong Bragg backscattering makes wave resonator less transparent and this factor increases resonance, but above 50% the density jump is destroyed by white noise and amplification factor decreases. However these resonance behaviour is enhanced in Helmholtz equation solution due to the fact that the resonance cavity is fully filled and in the reality it takes time to fill it. During this time the density profile changes and kills the resonant condition. However this mechanism can generate phase jumps.

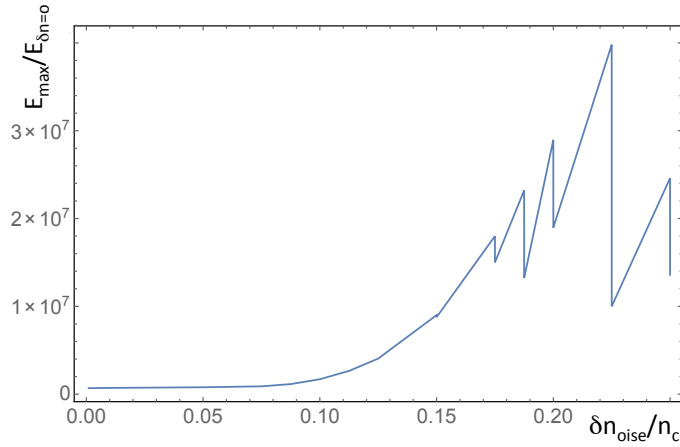


Figure 3.8: Evolution of the field amplification due to the noise as a function of the noise level normalized by the cut-off density. Same conditions as figure 3.7

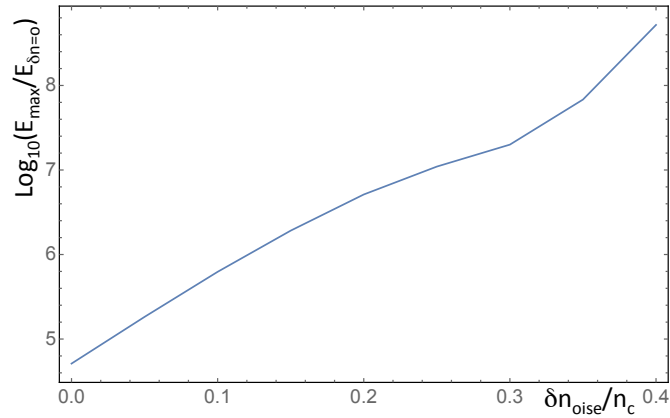


Figure 3.9: Evolution of the field amplification due to the noise as a function of the noise level using extended precision

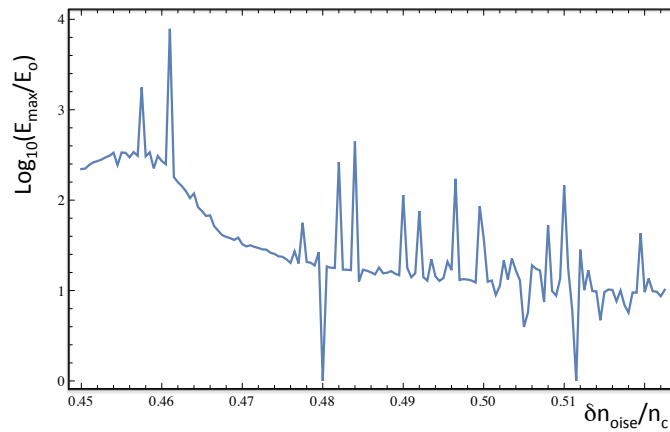


Figure 3.10: Evolution of the amplification factor as a function of the noise level using double precision. The trapping regimes change when the density fluctuations are truncated. Peaks are present when the double precision is used.

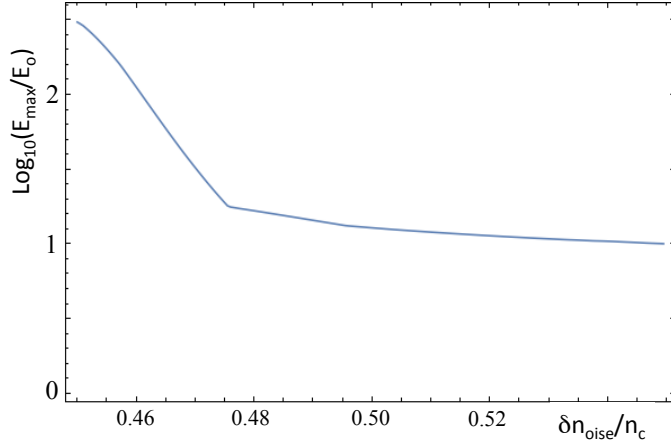


Figure 3.11: Evolution of the amplification factor as a function of the noise level using extended precision. The trapping regimes change when the density fluctuations are truncated. Peaks are present when the extended precision is used.

3.3 Time dependent wave-equation numerical solution

Usually tokamak turbulence studied by UFSR is very strong especially at the edge. Wave multi-reflections, reflection far from cut off position, wave trapping can take place during measurements. In this case signals from different positions will be mixed together in the antenna at some moment of time. However these signals will have different beat frequency. To separate signal from the cut-off reflection sliding window filtering of the spectrogram should be done. It is not possible to simulate such a problem using Helmholtz equation. In this section we will have a look on comparison of 1D Helmholtz equation solver results versus 1D wave equation solver in the case of O-mode wave.

Going from Maxwell's equations

$$\begin{cases} \text{rot}\vec{E} = -\partial B/\partial t \\ \text{rot}\vec{B} = \mu_0[\vec{J} + \epsilon_0\partial\vec{E}/\partial t] \end{cases} \quad (3.23)$$

Where \vec{J} is a plasma current density. Applying *rot* to the first equation, in the case of independence of time and position coordinates, and using again relation $\text{rot}(\text{rot}\vec{A}) = \text{grad}(\text{div}\vec{A}) - \Delta\vec{A}$ we get:

$$\text{grad}(\text{div}\vec{E}) - \Delta\vec{E} = -\frac{\partial}{\partial t}\text{rot}\vec{B} \quad (3.24)$$

Replacing $\text{rot}\vec{B}$ by second equation from (3.23) taking into account plasma quasi-

neutrality $\text{div}\vec{E} = \rho/\epsilon_0 = 0$ we obtain the wave equation for a plasma:

$$c^2 \Delta \vec{E} = \frac{1}{\epsilon_0} \frac{\partial}{\partial t} \vec{J} + \frac{\partial^2 \vec{E}}{\partial t^2} \quad (3.25)$$

In this section for comparison with Helmholtz solver we will consider O-mode probing beam. Under collisionless cold plasma approximation, using electron motion equation (2.1) one can express the current time derivative as $\partial J_z / \partial t = \epsilon_0 \omega_p^2 E_z$. Here the magnetic field is directed along z axes. 1D O-mode wave equation can be written as:

$$c^2 \frac{\partial^2 E_z}{\partial x^2} = \omega_p^2 E_z + \frac{\partial^2 E_z}{\partial t^2} \quad (3.26)$$

Where x is the direction of wave propagation.

For a numerical solution we will use the second order finite difference time domain method.

$$E_i^{n+1} = -\omega_p^2 E_i^n dt^2 + 2E_i^{n-1} \left(1 - \left(\frac{cdt}{dx}\right)^2\right) + \left(\frac{cdt}{dx}\right)^2 (E_{i+1}^n + E_{i-1}^n) - E_i^{n-1} \quad (3.27)$$

In this finite difference time domain scheme, i is the space coordinate index, n - time step index, dx and dt are space and time discretization steps values. The numerical solution is stable when $dx/dt > c$. For our computations we have fixed $dx/dt = 2c$. In this case it is very convenient to express vacuum perfectly match layer on the boundaries of computation domain.

$$E_1^{n+1} = E_2^{n-1} \quad (3.28)$$

$$E_N^{n+1} = E_{N-1}^{n-1} \quad (3.29)$$

Here N is a number of spacial points on the computation grid.

3.3.1 1D Wave equation solver IQ detection technique

To simulate IQ detection technique in the frame of wave equation solver, 2 computations were done. These two computations had source signals with an initial phase difference of $\pi/2$. Source signals can be expressed as:

$$I_0^s = A_0 \sin(\phi_0) \quad (3.30)$$

$$I_0^c = A_0 \cos(\phi_0) \quad (3.31)$$

And the received signal:

$$I_{ref}^s = A_{ref} \sin(\phi_{ref} + \phi_{vacuum}) \quad (3.32)$$

$$I_{ref}^c = A_{ref} \cos(\phi_{ref} + \phi_{vacuum}) \quad (3.33)$$

Using these signals real complex part of complex signal $I = A_{ref} \exp(\phi)$ can be calculated.

$$\begin{aligned} \Re(I) &= A_{ref} \cos(\phi_{ref} - \phi_0 - \phi_{vacuum}) = \\ &A_{ref} [\cos(\phi_{ref}) \cos(\phi_0 + \phi_{vacuum}) + \sin(\phi_{ref}) \sin(\phi_0 + \phi_{vacuum})] = \\ &\frac{1}{A_0} [I_{ref}^c I_0^c + I_{ref}^s I_0^s] \end{aligned} \quad (3.34)$$

$$\begin{aligned} \Im(I) &= A_{ref} \sin(\phi_{ref} - \phi_0 - \phi_{vacuum}) = \\ &A_{ref} [\sin(\phi_{ref}) \cos(\phi_0 + \phi_{vacuum}) - \cos(\phi_{ref}) \sin(\phi_0 + \phi_{vacuum})] = \\ &\frac{1}{A_0} [I_{ref}^s I_0^c - I_{ref}^c I_0^s] \end{aligned} \quad (3.35)$$

Signal amplitude and phase can be calculated as:

$$\begin{aligned} A_{ref} &= \sqrt{\Re^2(I) + \Im^2(I)} \\ \phi &= \arctan(\Im(I)/\Re(I)) \end{aligned} \quad (3.36)$$

In the reality due to fast frequency sweeping, sin and cos beam waves behave differently in the plasma and signals can have different phase and amplitude.

$$I_{tot} = I + \tilde{I} \quad (3.37)$$

And as a result signal I also contains fast oscillating part \tilde{I} . This content can be filtered out.

3.4 Comparison between 1D Helmholtz equation solver and time dependant 1D wave equation solver

In this section we will highlight few examples of turbulence on a linear plasma density profile. First we will show a small level homogeneous turbulence, then example with weak core turbulence with long correlation length and strong edge turbulence with short correlation length will be considered.

For our first example we have chosen a linear density profile with plasma density

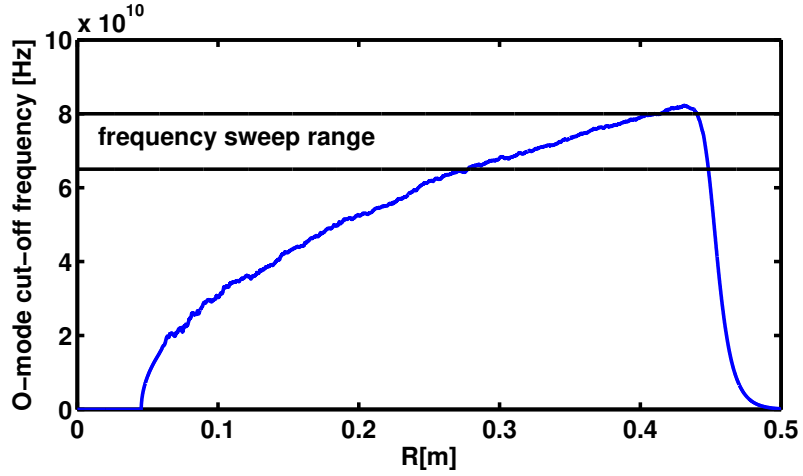


Figure 3.12: O-mode cut-off frequency (blue) computed from density with homogeneous, isotropic turbulence

up to $10^{20}m^{-3}$ and length of $45cm$ (see figure 3.12). Frequency sweeping was done with constant frequency sweeping speed of $20GHz/us$. To simulate IQ detection technique we compute reflectometry signal 2 times using sources with $\pi/2$ phase delay. Turbulence here is homogeneous and isotropic with amplitude equal to 1% of the maximum cut-off density. Turbulence spectrum is defined the same way as presented on figure 1.8. Dissipation region starts from $k = 10^3m^{-1}$. According to chapter 3.3 signal from FDTD computation was processed to filter out initial frequency oscillation. Figure

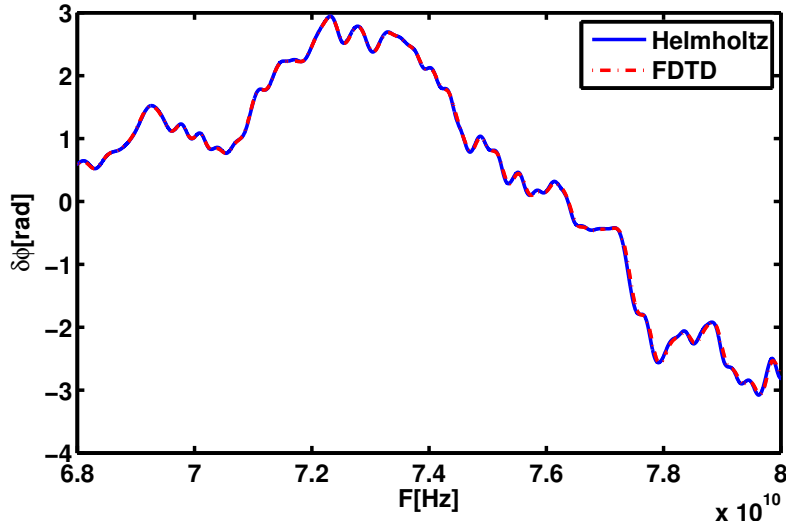


Figure 3.13: Phase variations, computed for the same density fluctuation realization using Helmholtz solver (blue) and finite difference time domain (FDTD) wave equation solver (red)

3.13 shows the phase variation. Phase variation was computed as a difference between computations obtained using unperturbed and perturbed density profiles. As one can

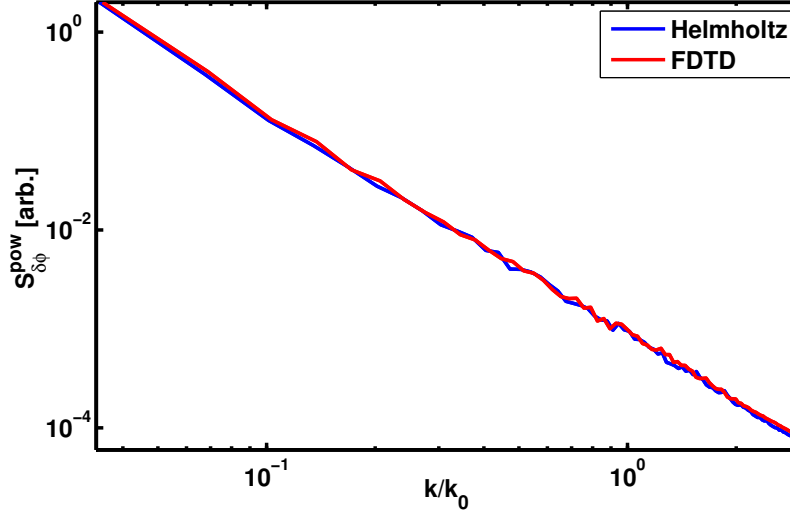


Figure 3.14: Phase variations power spectra computed with Helmholtz solver (blue) and finite difference time domain (FDTD) wave equation solver (red). Result was obtained by averaging over 100 different turbulence realizations

see from the figure 3.13 phase variations that we get using these 2 methods for a given case are very similar. Figure 3.14 shows the phase variation power spectrum which was achieved by averaging of 100 computations with different turbulence realizations. However even in presence of weak edge turbulence scattering before cut-off position and wave trapping can take place (especially in the case of short correlation length) and interacting with signal from main reflection it can cause significant change of phase variation. IQ signal spectrogram on figure 3.16 shows many multi-reflections as lines above the main reflection line. These reflections are not seen on the spectrogram from computation without turbulence (see figure 3.15). k_0 is the maximum probing frequency vacuum wave-number.

In tokamak plasmas typically plasma turbulence is not homogeneous. Turbulence is stronger near plasma edge (see figure 3.17). Near the plasma boundary turbulence can reach levels up to 20-30% root mean square value (RMS) of the local density [79]. Such a turbulence leads to nonlinear phase variation behaviour which complicates wave-number spectra measurements with USFR. Usually core turbulence is much weaker compared to the edge one. But to measure it, the probing beam should first cross strong edge turbulence layer. It will be shown and studied more carefully in the next chapter that strong edge turbulence can cause enhanced scattering of the probing beam and trap part of the beam between cut off and edge turbulence. In the next example we are using the same homogeneous turbulence as in previous computation, except that we have added another turbulence map with Gaussian shape amplitude envelop centred near the plasma edge. Example of cut off frequency profile is depicted on

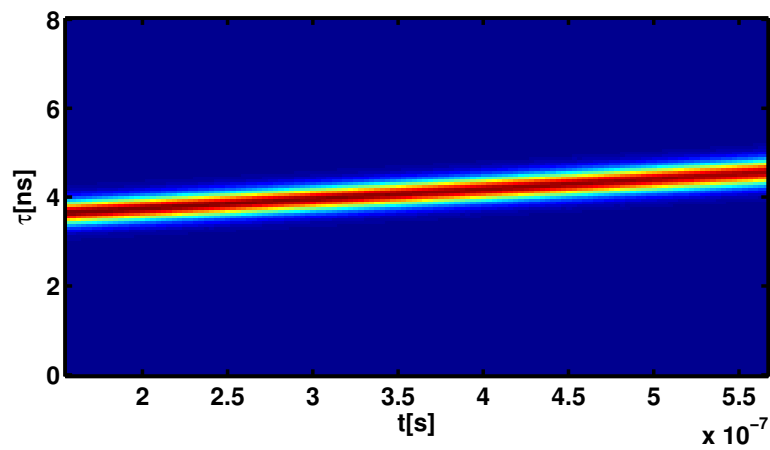


Figure 3.15: time of flight spectrogram computed by FDTD algorithm without turbulence

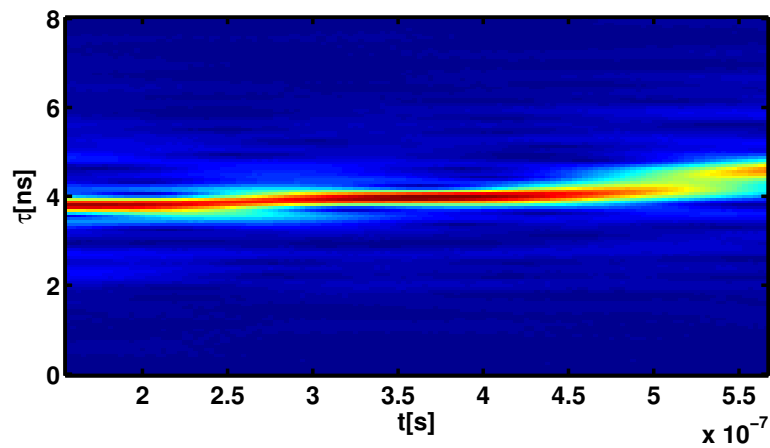


Figure 3.16: time of flight spectrogram computed by FDTD algorithm. Computation is done for chosen turbulence realization

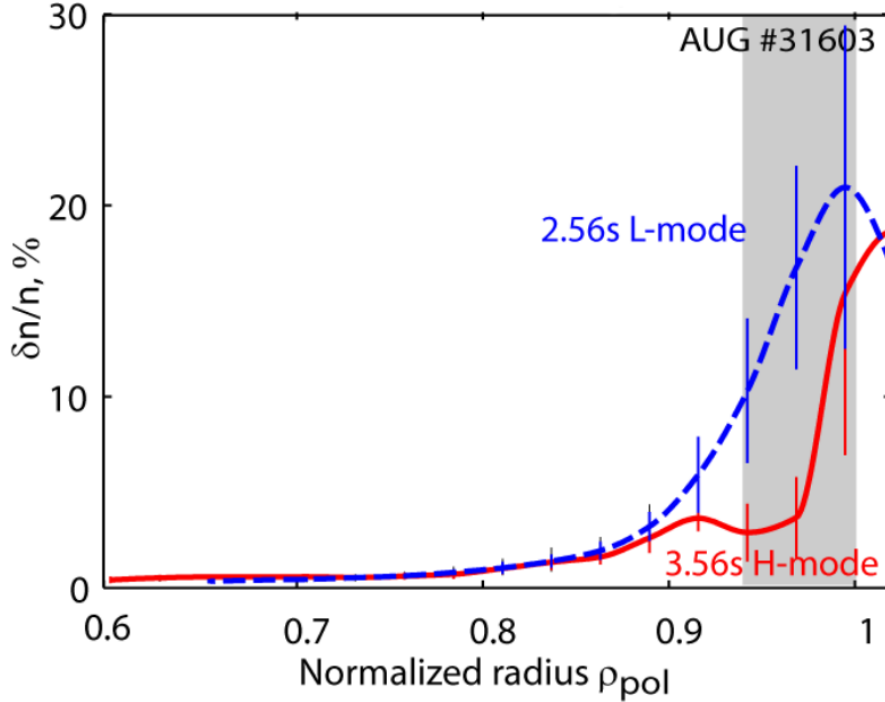


Figure 3.17: Turbulence root mean square amplitude profile in Asdex-U tokamak [79]

figure 3.18. Here we are looking on 2 computations: with maximum edge turbulence RMS value of 5% and 10% of cut-off density. 5% edge turbulence does not introduce a big difference between FDTD and Helmholtz computations. Spectrogram on figure 3.20 shows some multi-scattering (longer time of flight) and part of the beam scattered before the reflection (shorter time of flight) signal stays small. In the case of 10% edge turbulence level of multi-reflections of the probing wave are well pronounced (see figure 3.20). Enhanced reflection from strong edge turbulence layer can be seen on the time of flight spectrogram around $\tau = 0.5ns - 1ns$. Strong bragg reflection from inhomogeneous turbulence was studied in paper [88]. Moreover according to Mathieu equation (see section 2.1.8) high turbulence level triggers Bragg back-scattering of higher wave-number orders. The peak frequency guiding line differs much from the case without turbulence. This means that the effective time of flight has been changed. Difference between stationary solution provided by Helmholtz solver and time dependent FDTD computation corresponds to different interpretation of wave trapping resonances. Same resonance processes were highlighted in section 3.2.4. In the resonance case, to reach stationary solution, electromagnetic wave energy should be pumped continually in the trapping area, which is not the case when frequency sweeps are performed in FDTD computations. This can be seen on figure 3.19 where phase variations computed with FDTD and Helmholtz solver are compared. Beam multi-reflections increase the effective time of flight and signal from such a area usually is received at different time and

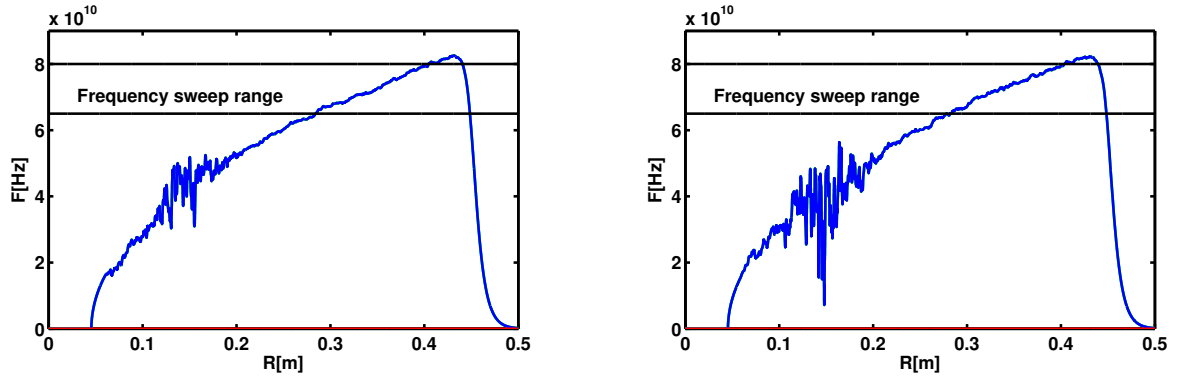


Figure 3.18: O-mode cut-off frequency (blue) computed from density with homogeneous, isotropic turbulence for edge turbulence maximum RMS values of 5%(left) and 10%(right)

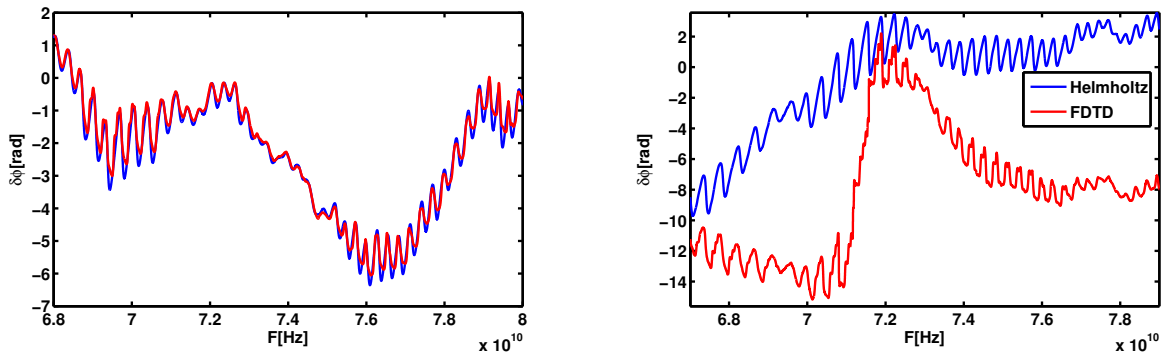


Figure 3.19: Phase variation obtained with FDTD(red) and Helmholtz(blue) for edge turbulence maximum RMS values of 5%(left) and 10%(right)

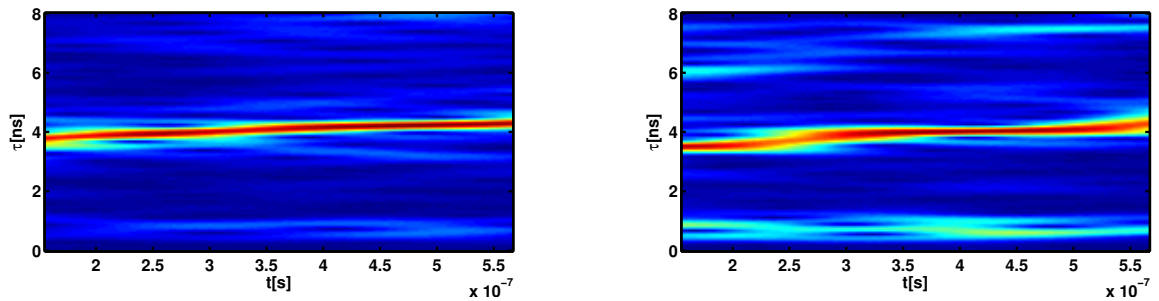


Figure 3.20: Time of flight spectrogram computed with FDTD for edge turbulence maximum RMS values of 5%(left) and 10%(right)

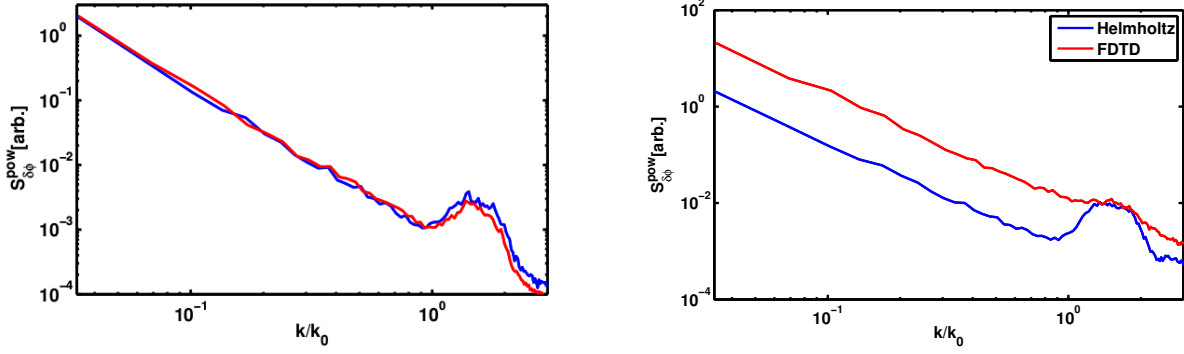


Figure 3.21: Phase variation spectrum obtained with FDTD(red) and Helmholtz(blue) for edge turbulence maximum RMS values of 5%(left) and 10%(right). k_0 is a maximum probing frequency vacuum wave-number.

can be associated with wrong position or filtered out depending on signal processing. In both cases signal amplitude can reach very small values and phase jump can take place. These phase jumps can change drastically the signal spectra (figure 3.21). From these 3 computations it is possible to conclude that for 1D computation, edge turbulence can change computed signal and interpretation of the experimental data under assumption of local measurements can be wrong. However FDTD computations performed in this section are only one dimensional, which means that energy loss in poloidal direction from a resonant area is impossible and wave trapping is very efficient. 2 dimensional computation can improve this point. In next section we will have a look on 2D full wave computations.

3.4.1 2D FDTD algorithm

2D effects are very important in reflectometer signals both in linear and nonlinear regimes. Poloidal turbulence spectra, finite beam size, 2D plasma profile, all these parameters can change reflectometer responses. Another important thing is the possibility to receive less beam energy than what was launched to the plasma. This changes the phase fluctuation spectrum and amplitude relation between scattered and unperturbed (computation without turbulence) fields in Born approximation (see section 3.5) which compose the total reflectometer signal. In my thesis I use IPF-FD3D - a finite difference time domain code developed at IGVP, Stuttgart, Germany [65]. Numerical schemes principle can be found in [65]. The code solves Maxwell's equations and electron motion equation in cold plasma approximation. The code can make computations in 1,2 and 3 dimensional space for ordinary, extraordinary and mixed modes. As receiving and emitting antenna patterns the code use Gaussian beams. This allows to easily extract incident field on the receiver antenna for reflectometer signal computation. Instead

of real frequency sweeping in the code set of frequencies within the probing band are launched into the plasma simultaneously. After stationary solution is reached signal on the antenna can be recorded, then processed with Fourier transform to separate signals by frequencies. This makes the code be very fast comparing with real frequency sweep codes [72]. Such a type of solution is similar to Helmholtz equation solver in 2D as it also searches for stationary solution. An advantage is that no artificial boundary conditions and processing methods are needed to separate incident and reflected beams. On the other hand this method in some situations, as shown in previous section 3.4, can change the results comparing to real IQ detection modelling [72].

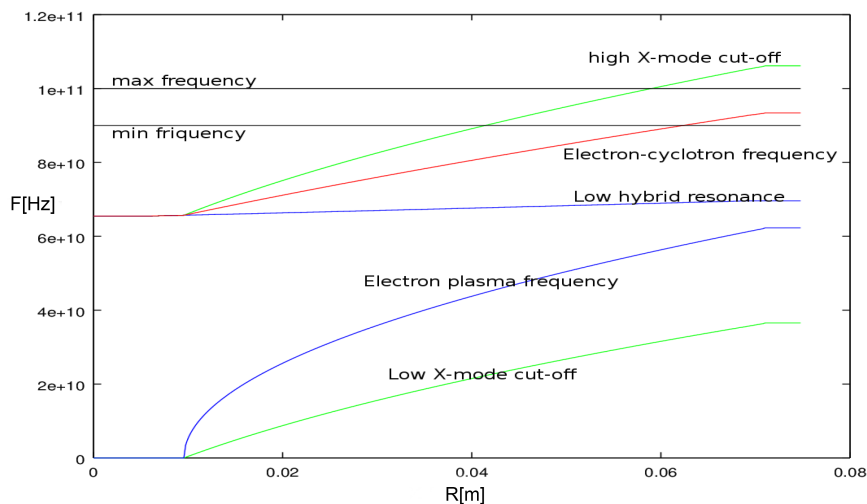


Figure 3.22: Electromagnetic wave cut-off frequency

Now we will show comparison results between IPF-FD3D code and 1D Helmholtz solver. For this comparison we will use X-mode wave in linear density profile plasmas (figure 3.22) in slab geometry and with poloidal plasma curvature. Turbulence here is homogeneous, and isotropic. In this chapter and everywhere further in this work turbulence is made using inverse Fourier transform. To create 2D spectral map from which 2D Fourier transform will be performed, an iterative algorithm to match desired 1D (or projected) spectrum was used (see Appendix A). The projected spectrum is presented on figure 3.23. Turbulence RMS amplitude is equal to 1%. It is homogeneous and isotropic. These computations can give an idea about poloidal wave-number and poloidal plasma curvature effects on reflectometry measurements. On figure 3.24 one can see the probing beam electric field distribution in case of poloidally curved plasma ($R_{curv} = 10cm$) and slab geometry plasmas ($R_{curv} = 3m$). Figure 3.24 represents interference images between different frequencies from the sweeping band. It should be admitted that curved plasmas spread much more the reflected beam than

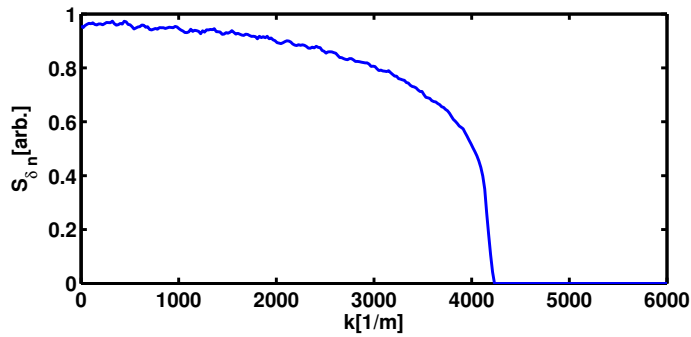


Figure 3.23: Turbulence wave-number spectrum

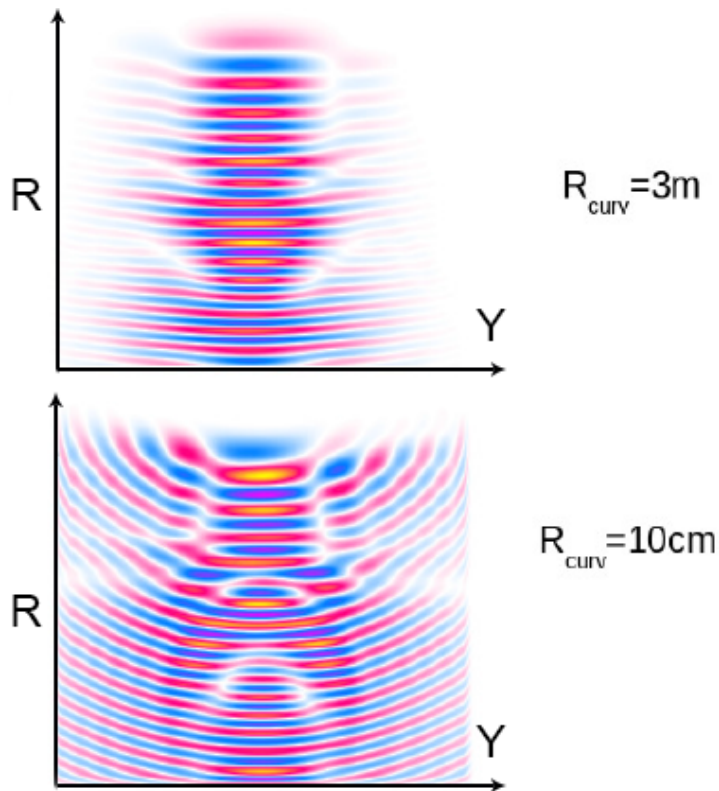


Figure 3.24: Electric field distribution. All swept frequencies are launched together to plasma

slab ones do. On picture 3.25 we compare 1D Helmholtz code phase variation spectra computation result with IPF-FD3D computations. Because of turbulence poloidal wave-numbers spectrum phase blurring takes place and phase response for 2D computations is weaker. However the poloidally curved plasma spreads the probing beam and only small part of the beam from straight radial direction reaches the receiving antenna. This makes this computation result be closer to 1D computation. It should be admitted that even 2D computations can't provide right phase variation spectrum. Due to the finite beam size and toroidal plasma curvature 3D probing beam will lose its

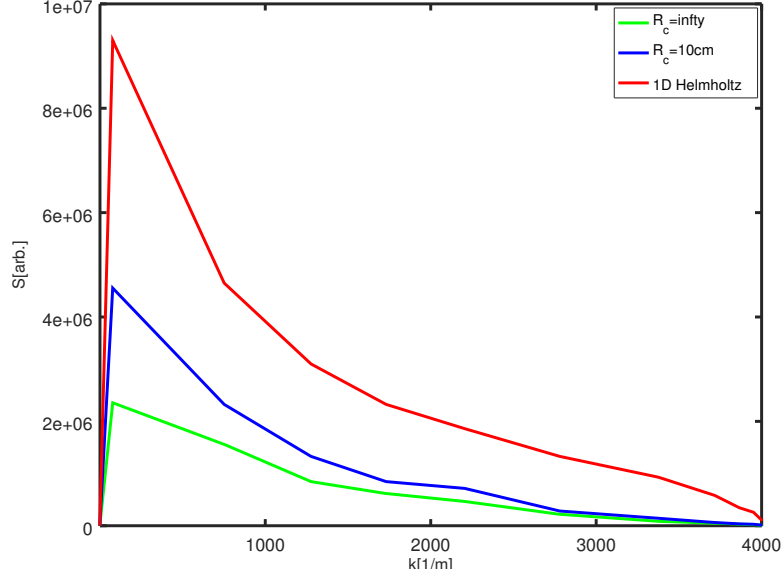


Figure 3.25: Phase fluctuation spectrum. Obtained by averaging of computations from 40 turbulence samples

power faster than the 2D one. This will redistribute scattered power (see next section) and change the resulting signal. Additionally decrease of phase variation can be caused by phase blurring from the beam toroidal size.

3.5 Reciprocity theorem approach

Let us consider a monochromatic radiation from the plasma resulting from current density $J(\vec{r})$.

$$\vec{E} = \vec{E}_\omega e^{-i\omega t} \quad (3.38)$$

$$\vec{H} = \vec{H}_\omega e^{-i\omega t} \quad (3.39)$$

Such electric and magnetic field can be described using further equations:

$$rot \vec{E}_\omega - i\omega \vec{B}_\omega = 0 \quad (3.40)$$

$$rot \vec{H}_\omega + i\omega \vec{D}_\omega = \vec{J} \quad (3.41)$$

Let us consider the same plasma but with transposed dielectric tensor and without source currents. This field distribution will describe the receiving antenna pattern:

$$rot \vec{E}_\omega^{(+)} - i\omega \vec{B}_\omega^{(+)} = 0 \quad (3.42)$$

$$rot \vec{H}_\omega^{(+)} + i\omega \vec{D}_\omega^{(+)} = 0 \quad (3.43)$$

Where $(+)$ refers to transposed dielectric tensor. The microwave radiation received by this antenna can be expressed through complex coefficient A_ω .

$$\vec{E}_{out} = A_\omega \vec{E}_{wg} \quad (3.44)$$

$$\vec{H}_{out} = A_\omega \vec{H}_{wg} \quad (3.45)$$

Where \vec{E}_{out} and \vec{H}_{out} are electric and magnetic fields inside the receiving waveguide and \vec{E}_{wg} and \vec{H}_{wg} are fundamental waveguide mode electric and magnetic field normalized as:

$$\frac{1}{2} \int [\vec{E}_{wg} \times \vec{H}_{wg}^*] d\vec{S} = 1 \quad (3.46)$$

Where S is a surface inside the waveguide. Field sources E and $E^{(+)}$ are normalized the same way. We will multiply equation (3.40) by $\vec{H}^{(+)}$, equation (3.41) by $\vec{E}^{(+)}$, and equation (3.42) by $-\vec{H}$, equation (3.41) by $-\vec{E}$ and sum the results.

$$div[\vec{E}_\omega \times \vec{H}_\omega^{(+)} + \vec{H}_\omega \times \vec{E}_\omega^{(+)}] + i\omega[\vec{E}_\omega^{(+)} \vec{D}_\omega - \vec{D}_\omega^{(+)} \vec{E}_\omega] = \vec{J} \vec{E}_\omega^{(+)} \quad (3.47)$$

Let us integrate the whole expression over an infinite volume.

$$\int div[\vec{E}_\omega \times \vec{H}_\omega^{(+)} + \vec{H}_\omega \times \vec{E}_\omega^{(+)}] dV + i\omega \int [\vec{E}_\omega^{(+)} \vec{D}_\omega - \vec{D}_\omega^{(+)} \vec{E}_\omega] dV = \int \vec{J} \vec{E}_\omega^{(+)} dV \quad (3.48)$$

According to [80, 81], expression $\int [\vec{E}_\omega^{(+)} \vec{D}_\omega - \vec{D}_\omega^{(+)} \vec{E}_\omega] dV$ vanishes with integration and can be neglected. Volume integral in the left part of the equation (3.48) can be transformed to a surface integral. Outside the waveguide, the integral will be zero as all contributions under it will cancel each other.

$$\int [\vec{E}_\omega \times \vec{H}_\omega^{(+)} + \vec{H}_\omega \times \vec{E}_\omega^{(+)}] dS_{wg} = \int \vec{J} \vec{E}_\omega^{(+)} dV \quad (3.49)$$

Using properties of the fundamental mode of the waveguide and equation (3.46) it is possible to admit that:

$$\frac{1}{2} \int [\vec{E}_\omega \times \vec{H}_\omega^{(+)} + \vec{H}_\omega \times \vec{E}_\omega^{(+)}] dS_{wg} = 2A_\omega \quad (3.50)$$

Finally we can achieve expression for A_ω .

$$A_\omega = \frac{1}{4} \int \vec{J} \vec{E}_\omega^{(+)} dV \quad (3.51)$$

In next section we will have a look on the application of this result to reflectometer signal computation.

3.5.1 Reciprocity theorem in application to reflectometry modeling

In the Born approximation, the received signal in the reflectometer waveguide can be expressed as superposition of unperturbed signal (from a plasma without turbulence) and the fluctuating signal associated with turbulence.

$$I(\omega) = I_{in}(\omega) + I_s(\omega) \quad (3.52)$$

Here $I(\omega)$ is the total signal with angular probing beam frequency ω which is composed of I_{in} is the unperturbed reflected signal (computed without turbulence) and I_s - the field scattered from the turbulence received by the antenna. In a tokamak the turbulent modes are elongated along the magnetic field lines in the toroidal direction. Neglecting the toroidal curvature effects, which is often assumed in a tokamak, computations in the 2D poloidal plane can be considered. We will use Cartesian coordinates system with tokamak magnetic field $\vec{B}_0 \parallel x$, z is a radial direction, and $y \perp \vec{B}_0$ is a poloidal direction.

$$I_{in}(\omega) = \int G(z_a, y) E_{in}(z_a, y) dy \quad (3.53)$$

Where z_a is the antenna position in the radial direction, G is the antenna pattern, and E_{in} is the unperturbed field of the reflected wave. A probing beam field scattered by the turbulence and received by the antenna can then be expressed as:

$$I_s(\omega) = \frac{1}{4} \int dy' \int dz dy \vec{J} \vec{E}_\omega^{(+)} \cdot \vec{E}_{wg}(y') \quad (3.54)$$

Depending on the polarization, the radiating current \vec{J} can be expressed through conductivity tensor σ . Relation for O-mode is very simple and will be presented here.

Radiation current in the case of reflectometry is the current associated with turbulence. For O-mode this current can be expressed as:

$$J_z = \frac{i\omega\epsilon_0}{n_c} E_z(\omega) \cdot \delta n \quad (3.55)$$

Where n_c is the so-called critical density for the probing frequency. And a final formula

for the scattered signal received by the reflectometer antenna can be written as:

$$I_s(\omega) = \frac{i\omega\epsilon_0}{4n_c} \int dy' \int dz dy \delta n E_{z(\omega)} E_{z(\omega)}^{(+)} \cdot \vec{E}_{wg}(y') \quad (3.56)$$

To use this expression one should first calculate the unperturbed electric field distribution resulting from the launched electromagnetic beam by emitting and receiving antennas. This can be done using full-wave codes [65, 72] and analytical models [73] taking in account the exact phase relation between the total field and the received unperturbed signal. Very similar expression can be found in so called weighting function method [82]. In this method, the reflectometer phase response to turbulence density fluctuations δn are integrated with weighting function W .

$$W = E_{z(\omega)} E_{z(\omega)}^{(+)} \quad (3.57)$$

This expression together with (3.44) gives possibility to extract scattered by turbulence field received antenna. In next section we will look more closely on the application of this formula for USFR.

3.5.2 Reduced reciprocity theorem approach

For ultra fast swept reflectometry one should calculate around 1000 points for different frequencies to follow the phase variation. Big amount of data should be processed each time the phase response is computed. To reduce the amount of data and make the method more applicable let us consider the mono static antenna case with both the received and the emitted waves assumed to be plan waves. This is possible in the slab geometry with smooth plasma profile. Under such conditions we will express the incident electric field in the vacuum region.

$$| E_{z(\omega)} | e^{i(\omega t + \phi_0)} = | E_{in} | e^{i(k_z + \omega t + \phi_1)} + | E_{out} | e^{i(k_z - \omega t + \phi_2)} \quad (3.58)$$

Where k is the probing beam vacuum wave number, E_{in} and E_{out} are incident and reflected waves. Receiving antenna field $E_{z(\omega)}^{(+)}$ can be expressed the same way. Under current assumptions $| E_{out} | = | E_{in} |$. Consequently the total field will have a form of standing wave $E_{z(\omega)} = \sin(k_z + \phi_k) \cos(\omega t + \phi_0)$. In this case the weighting function will look like:

$$W = E_{z(\omega)} \cdot E_{z(\omega)}^{(+)} = | E_i |^2 \exp(i2\phi_0) \quad (3.59)$$

The phase ϕ_1 is defined by initial conditions. However the difference between weighting function phase ϕ_0 and received field phase ϕ_1 is not fixed and should be taken into

account when the phase variation is computed. To simplify the computation we will use expression for the phase variation written assuming $\phi_0 = \phi_1 = 0$ but to compensate effects of different phases between scattered field and unperturbed field as well as beam wave-front curvature we have introduced the parameter $\eta(\omega)$. This leads to:

$$\delta\phi = \arctan(\eta(\omega)I_s/I_{in}) \quad (3.60)$$

Where η is a normalization coefficient which has to be computed for each density profile. For the UFSR phase response it was found that the coefficient η is proportional to the square root of the unperturbed reflected signal amplitude received by the reflectometer antenna.

$$\eta(w) \propto |I_{in}|^{1/2} \quad (3.61)$$

3.5.3 Reduced reciprocity theorem application example

The reduced reciprocity theorem model which was introduced in previous section can be successfully applied in the case of slab geometry plasmas and small divergence probing beams. In this section we will apply it on JET tokamak experimental data. Density profile is depicted on figure 3.26. Probing area is located in the core region. For the

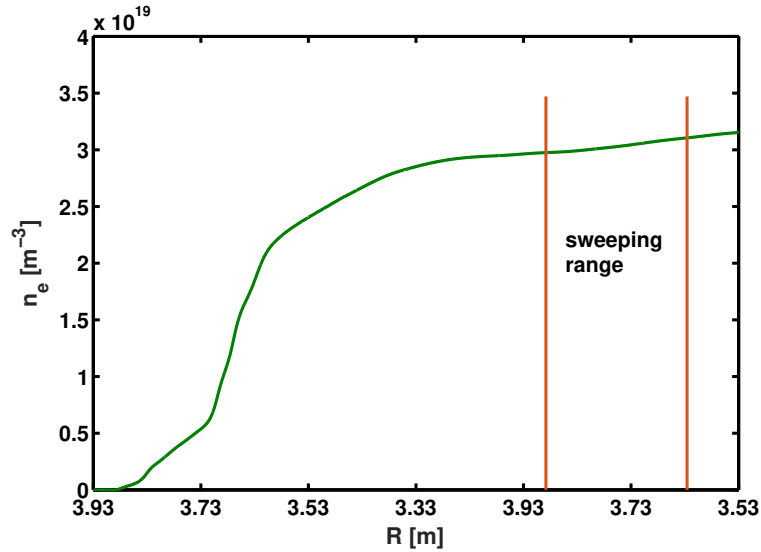


Figure 3.26: JET tokamak density profile with minimal and maximal cut-off positions

computation we are using slab geometry plasmas with inhomogeneous turbulence. The inhomogeneous turbulence is created by superimposing 20 homogeneous turbulence maps, each of which was multiplied by localization envelop (see figure 3.28). Envelops have overlap which allows to have smooth transition between homogeneous turbulence maps. Spectra that were used in computation are typical spectra which can be used as

first step assumption for closed loop algorithm. Some of these spectra are depicted on figure 3.29. In the final step of turbulence creation it was multiplied with the turbulence amplitude envelope (figure 3.27).

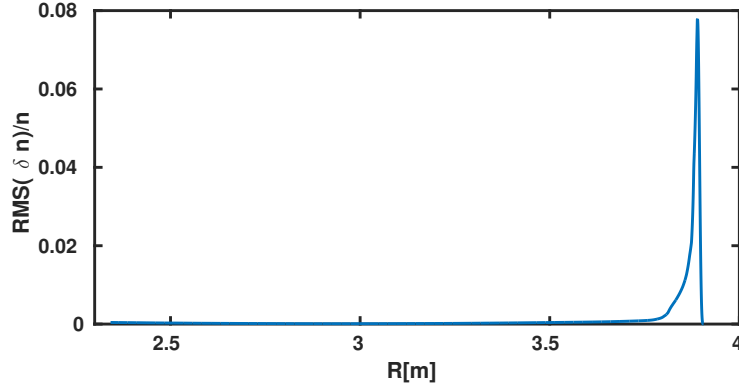


Figure 3.27: Turbulence RMS value envelope

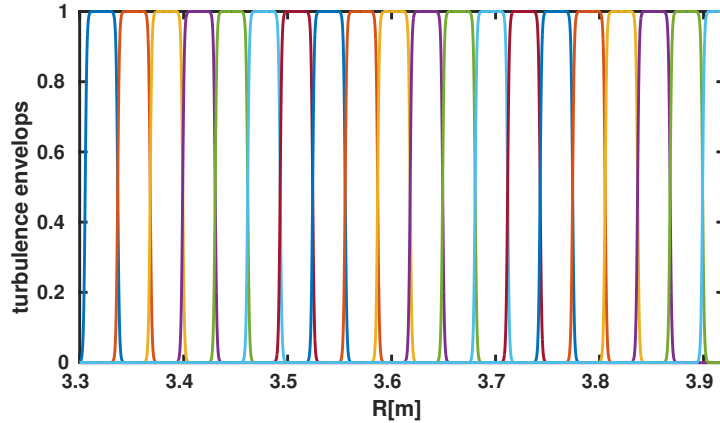


Figure 3.28: Inhomogeneous turbulence envelopes.

X-mode probing beam was used. Frequency sweep was covering the range from 79.5GHz to 96GHz. The probing beam width is equal to 12 cm. The reduced reciprocity theorem (RRT) approach was used under conditions of long probing wave propagation path. For extraordinary mode RRT expression for phase can be rewritten by replacing $\delta n/n_c$ by common for both modes, square refractive index variation $\delta(N^2)$. Modulus of the weighting function for E_y field maximum probing frequency within the frequency band is depicted on figure 3.30. Weighting functions for each frequency were computed using IPF-FD3D code.

One can see that the wave front of weighting function is almost flat and it allows us to use RRT approach. For comparison with common 1D technique 1D Helmholtz equation solver was used to compute phase variation spectrum. For one dimensional

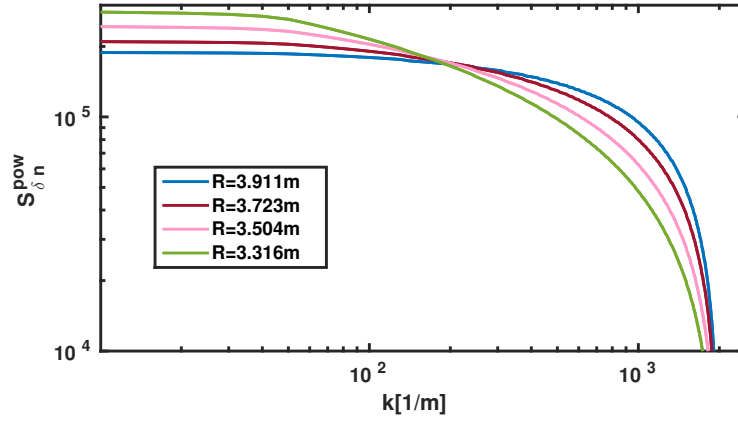


Figure 3.29: Turbulence wave-number spectra of inhomogeneous turbulence for different radial positions

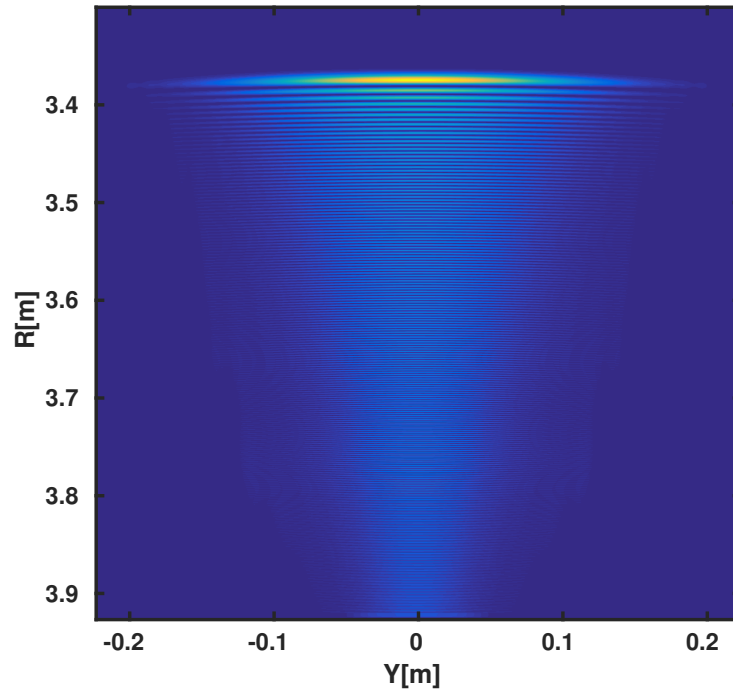


Figure 3.30: Modulus of the weighting function for y component of the electric field

computations 1D slices of 2D turbulence used in 2D computations were used. Results of computations can be found on figure 3.31. We can see that in the case of relatively large beam width and slab geometry and small turbulence the RRT approach gives very similar to 2D full-wave modelling result. However 1D computation results have higher amplitude and different wave-number slope. RRT approach can be used as synthetic diagnostic for closed loop algorithm in the case of small turbulence level.

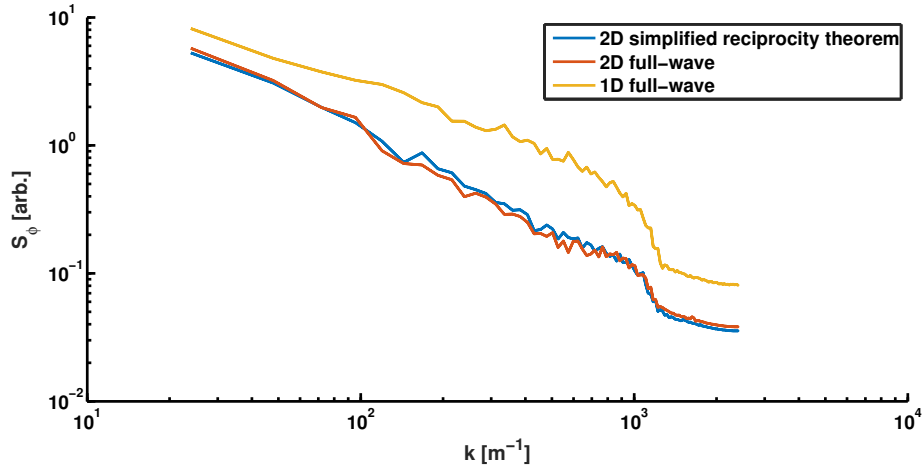


Figure 3.31: Phase fluctuation spectra: red - 2D IPF-FD3D computation results, blue - reduced reciprocity theorem approach computation result, yellow - 1D Helmholtz equation solver computation results

3.6 Discussions

Reflectometry signal dependencies are very complex. To process experimental data, inverse problem should be solved. Use of iterative algorithm is limited when dependences between phase fluctuation and density fluctuation are not local and not linear. Different computation methods can produce different results depending on what is taken into account. Stationary numerical solution can remove some of turbulence related artifacts from the signal. None of the described methods are able to precisely calculate reflectometer response. For this needs full wave time dependent 3D code with real frequency sweep should be used. However using the proposed methods, some characteristic behaviour of the reflectometer response can be studied. Results of such a study will be shown in next chapter.

Chapter 4

Strong edge turbulence effects on reflectometer plasma core measurements

In this chapter we will have a look on possible effects on reflectometer signal caused by a strong edge turbulence. First we will look at probing beam widening and phase change in turbulent plasmas. Then edge turbulence effects on phase variation will be investigated in slab geometry using separation of turbulence wave-numbers in the edge and core turbulences. Furthermore a case of more realistic turbulence spectrum in slab geometry will be studied and based on experimental data turbulence for Tore-Supra tokamak with 2D profile with poloidal curvature. To explore the limits of the reduced reciprocity theorem approach it will be also applied to the data and compared with full wave computation. However results of IPF-FD3D code in this case could be not comparable with experimental data due to different signal extraction and processing techniques (see section 3.6).

4.1 Probing beam propagation through turbulent plasma

Launched by the emitting antenna the probing beam suffers widening and changes of its phase. In this section we will have a closer look on loss of coherency process [83], and the wave widening process explained in [84].

First let us consider a 1D plasma with plan wave which can be described by 1D Helmholtz equation (3.4). Under WKB approximation let us introduce 1D density perturbation. The phase perturbation caused by turbulence with the first order accuracy

according to [85], [86] can be expressed as:

$$\delta\phi = -\frac{\omega^2}{2c^2} \int_0^{R_0} h_e \frac{\delta n}{n_c k} dR \quad (4.1)$$

Here k is the local probing beam wave-number, R_0 - phase observation coordinate, $h_e = 1$ in the case of ordinary mode. X-mode expression gives [87]:

$$h_e = \frac{(\omega^2 - 2\omega_{pe}^2)(\omega^2 - \omega_{ce}^2) + \omega_{pe}^4}{(\omega^2 - \omega_{pe}^2 - \omega_{ce}^2)^2} \quad (4.2)$$

According to [83] [84] the O-mode phase correlation function is given by:

$$\langle \delta\phi_i, \delta\phi_j \rangle = \frac{\omega^2}{4c^4} \int_0^{R_0} dR_1 \int_0^{R_0} dR_2 \frac{\langle \delta n_i(R_1), \delta n_j(R_2) \rangle}{k(R_1)k(R_2)n_c^2} \quad (4.3)$$

Where ϕ_i is the beam phase after propagation through plasma turbulence realization δn_i , $\langle \dots \rangle$ is a statistical averaging. In the case of homogeneous turbulence $\langle \delta n_i, \delta n_j \rangle$ is equal to density perturbation correlation function.

$$\langle \delta n_i, \delta n_j \rangle = \langle \delta n^2 \rangle K(R_i - R_j) \quad (4.4)$$

Where K is normalized turbulence autocorrelation function: $K(0) = 1$. The average electric field can be expressed as:

$$\langle E \rangle = E_0 e^{i\phi_0} \langle e^{-i(\delta\phi_i - \delta\phi_j)} \rangle = E_0 e^{i\phi_0} e^{-\frac{\langle \delta\phi_i, \delta\phi_j \rangle}{2}} = E_0 e^{i\phi_0} e^{-\frac{\kappa}{2}} \quad (4.5)$$

Using normalized correlation function expression (4.3) can be transformed to:

$$\kappa = \langle \delta\phi_i, \delta\phi_j \rangle = \frac{\omega^4}{4c^4} \int_0^{R_c} \frac{dR}{k^2} \left[\frac{RMS(\delta n)}{n_c} \right]^2 \int d\Delta K(\Delta) \quad (4.6)$$

Where Δ is equal to $R_i - R_j$.

The obtained simple expression allows us to estimate loss of coherency of the probing beam when it crosses turbulence layer. Effect on averaged field is stronger when $\int K d\Delta$ is larger. This corresponds to longer turbulence correlation lengths.

4.1.1 Beam properties change in turbulent plasma. Modeling examples

Full-wave modelling is a very good tool for basic processes understanding. Using numerical modelling one can look on some parameters that are not available in real

experiments. In this section we will check turbulence impact on the O-mode probing beam properties such as beam shape and phase change. According to (4.6) short correlation length turbulence is expected to influence more the waves phase change. As a result of past turbulence tokamak observation it was found that correlation length in the plasma edge region, where plasma turbulence amplitude reaches highest values, is usually smaller than in the plasma core region. However 2D effects caused by Bragg back scattering is more complex and in this section we will not focus on them. For further analysis we will use slab geometry density profile without wave reflection (figure. 4.1).

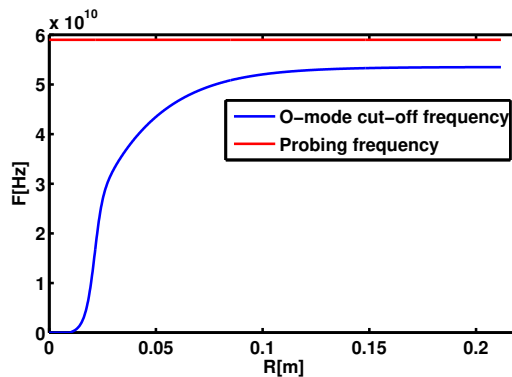


Figure 4.1: O-mode cut-off frequency profile (blue), probing wave frequency (red)

We will place a strong turbulence layer near $R = 6.3\text{cm}$. The turbulence is isotropic. It has a Gaussian shape amplitude envelop with half amplitude width of 4.2mm (figure 4.2). To avoid negative density formation due to the turbulence, a special algorithm was used to smoothly increase density in negative density areas.

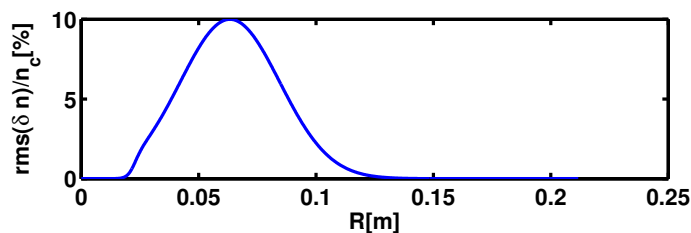


Figure 4.2: Turbulence root mean square amplitude envelop with a maximum of 10% of the critical density n_c

Spectral shape of the turbulence was taken flat in the middle cross-section of 2D spectrum with maximum k-number (k_{max}). The projection of this isotropic 2D spectrum is represented on figure 4.3. For a first computation we will use turbulence with $k_{max} = k_0$. One monochromatic wave will be launched with vacuum wavelength k_0 . Here the turbulence correlation wavelength is equal to 4.2mm . In the literature correlation length is defined differently [57, 100]. In our computations it is computed as

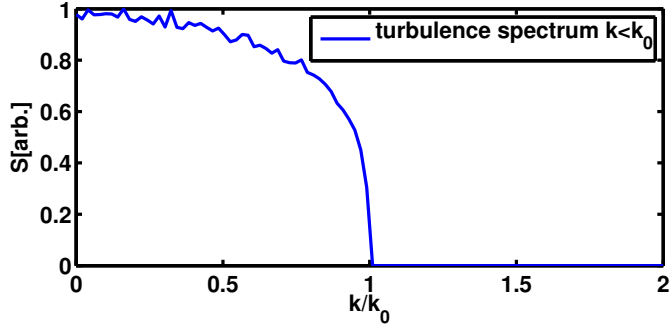


Figure 4.3: Turbulence spectrum. $k_{max} = k_0$

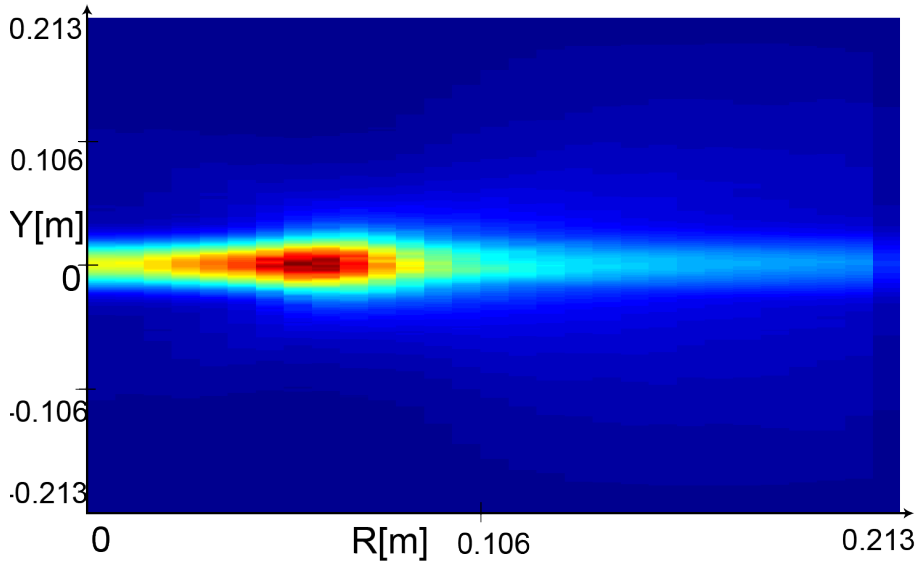


Figure 4.4: Electric field normalized power distribution

a turbulence autocorrelation function half width [57]. Such a correlation length is in the order of magnitude of measured correlation lengths on Tore-Supra Tokamak [57].

Averaged over different density fluctuation realizations, the electric field power distribution is depicted on figure 4.4. To obtain this 2D plot a thousand of computation samples were averaged. One can find a single electric field snapshot on figure 4.5. Let us look more closely on the poloidal cut of this 2D plot behind the turbulence layer (see figure 4.6). As one can see, the wave after propagation through a turbulent layer clearly separates into two Gaussian-like beams. More information on the beam can be obtained when field maps from computations with different turbulence realizations are superimposed with each other on the same poloidal cut and at the same time. This way, the field with oscillating phase part will be vanished out and with enough samples only the field with initial phase will remain (figure 4.7).

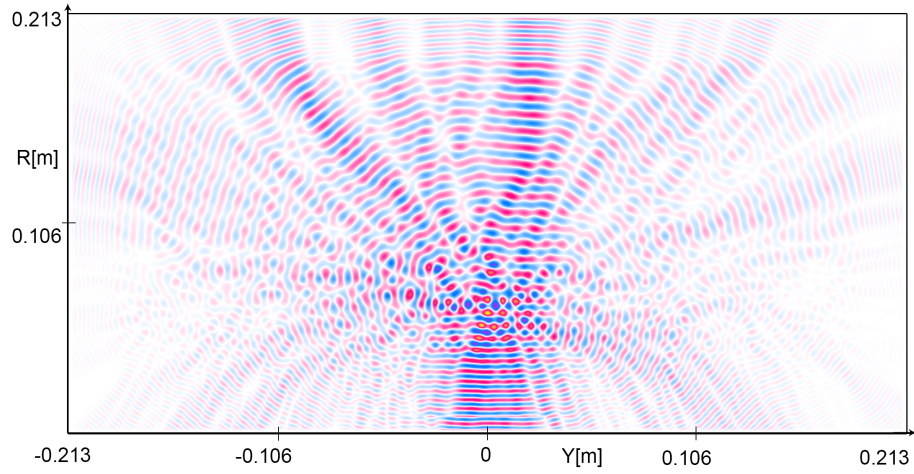


Figure 4.5: Electric field distribution snapshot. $k_{max} = k_0$

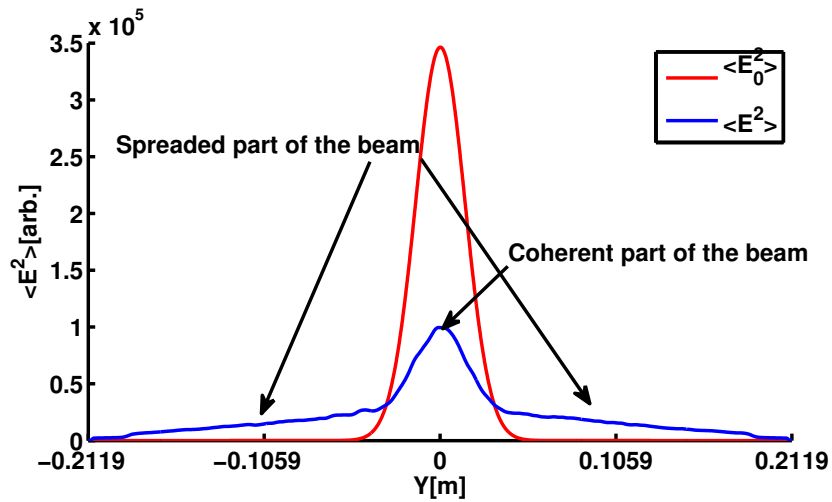


Figure 4.6: Electric field power distribution averaged over 1000 turbulence realizations. Computation without turbulence (red), and computation with turbulence (blue)

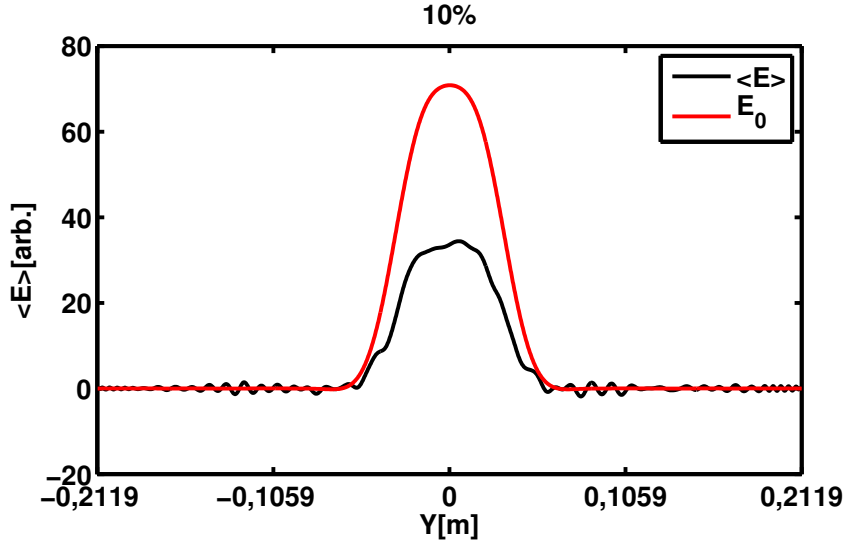


Figure 4.7: Electric field averaged over 1000 turbulence realizations (electric field coherent part)

With 10% turbulence amplitude maximum and correlation length of 4.2mm half of the beam loses its coherency and spreads in a wide range of directions. Next we will call this part of the beam the incoherent beam part. Other part of the beam does not change its phase and shape (coherent beam part). Using theory introduced in a section 4.1 with help of equation (4.5) one can calculate the coherent field part relative amplitude $e^{-\kappa/2} = \text{MAX}(\langle E \rangle) / \text{MAX}(E_0)$. Here E_0 is the field computed without turbulence layer. For both numerical and analytical solutions close results of attenuation around 0.5 were obtained. This example is very interesting in terms of understanding the physics but in the case of such turbulence not coherent part of the beam will not be seen by the reflectometer antenna as widening angle ($\alpha \propto 1/l_c$ [84]) is very big and only small part of not coherent signal will be received by the reflectometer. Except maybe in the cases when the antenna is situated very close to the plasma edge turbulence.

To decrease the coherent field part amplitude and the incoherent part widening angle, let us analyse the case when $k_{max} = 0.1k_0$. This turbulence has a correlation length of 3.6cm . Spectrum of such a turbulence is depicted on fig. 4.8. Electric field structure from one run is depicted on figure 4.9. As before we will analyse the electric field after the beam crosses the turbulence. Averaged power and averaged electric fields were calculated for turbulence profiles with maximum amplitude of 5%, 7% and 10% (see figures 4.10-4.12). From electric field averaging the coherent part attenuation coefficient was calculated, then permitting us to extract coherent beam part power from power plots $\langle E^2 \rangle - (\text{MAX}(\langle E \rangle) / \text{MAX}(E_0))^2 \cdot E_0^2$. The same coefficient was calculated using (4.5) (see figure 4.13). As a result we have obtained the incoherent

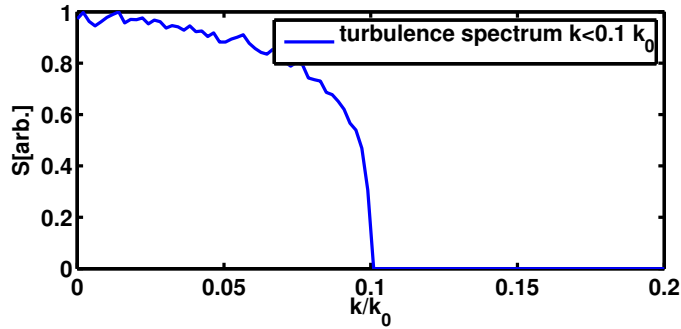


Figure 4.8: Turbulence spectrum. $k_{max} = 0.1k_0$

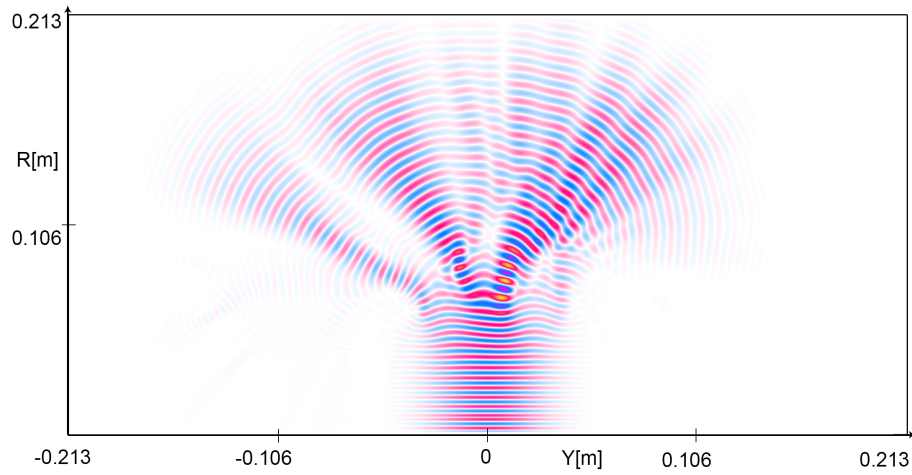


Figure 4.9: Electric field distribution snapshot. $k_{max} = 0.1k_0$

beam part power. One can admit that with full agreement to the simple 1D theory, the coherent part of the beam suffers attenuation caused by turbulence. This power profile was approximated with Gaussian function to estimate the beam widening. The incoherent beam size changes are depicted on figure 4.14. [h!] As one can see, after the coherent part of the beam be removed from the wave power distribution, the remaining incoherent beam is very close to a Gaussian shape. These examples are showing that 2 processes take place during beam propagation through the turbulent layer. The beam becomes wider and its phase suffers distortion. Part of the beam stays unchanged by the turbulence. An increase of turbulence correlation length enhances the coherent beam part attenuation but the incoherent part widening becomes weaker. These processes are well described by theory [83] [84]. However influence of edge turbulence on sweeping reflectometry signals is not well studied. In next section we will have a closer look on it.

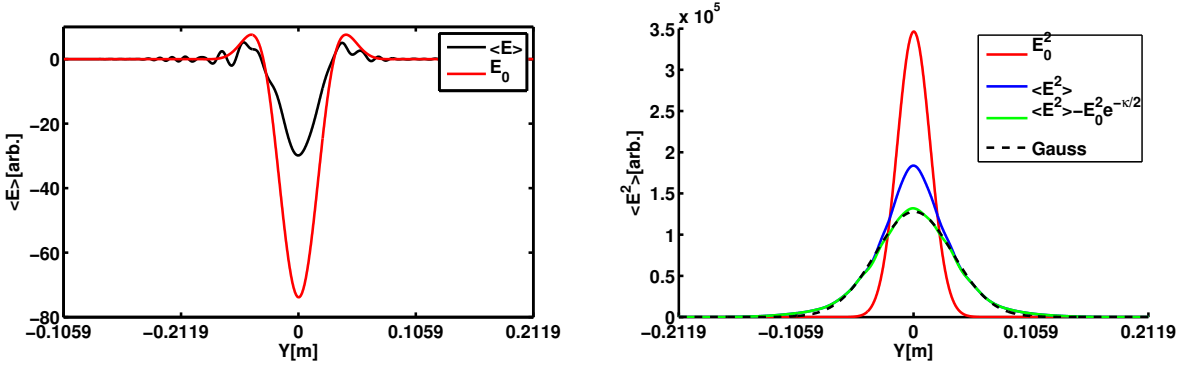


Figure 4.10: Maximum turbulence envelop amplitude equals to 5%.
left: Electric field averaged over computations with different density realizations (black),
Electric field computed without plasma turbulence (red).
right: averaged electric field power (blue), electric field power computed without plasma
turbulence (red), $\langle E^2 \rangle - (MAX(\langle E \rangle)/MAX(E_0))^2 \cdot E_0^2$ (green), Gaussian data
fit (black)

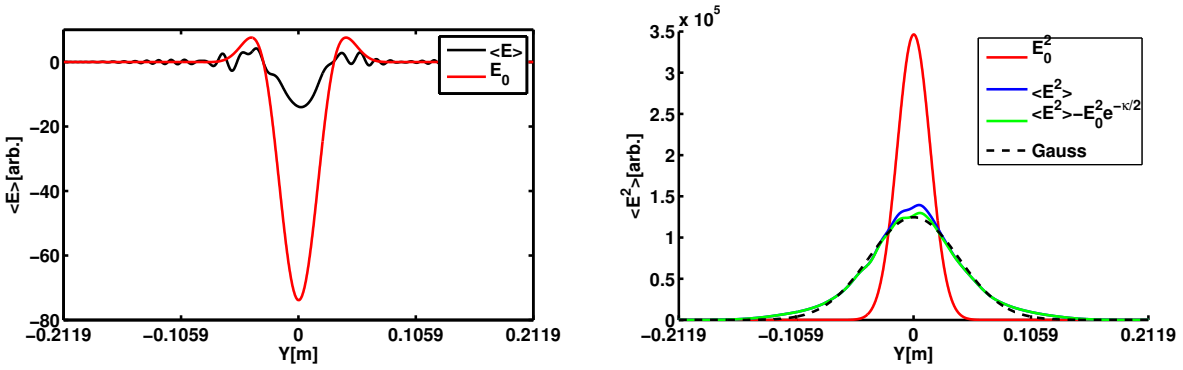


Figure 4.11: Maximum turbulence envelop amplitude equals to 7%.
The same as on figure 4.10

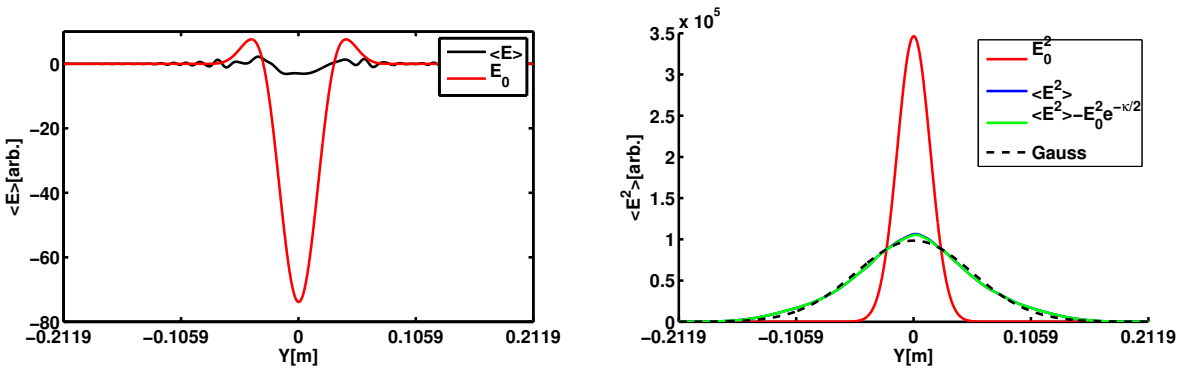


Figure 4.12: Maximum turbulence envelop amplitude equals to 10%.
The same as on figure 4.10

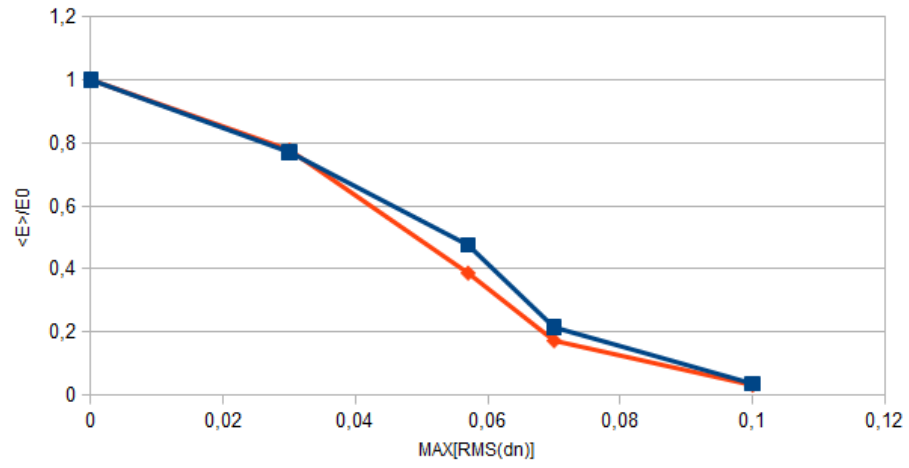


Figure 4.13: Coherent beam part attenuation computed with analytical formula(blue), and attenuation computed using IPF-FD3D code (orange)

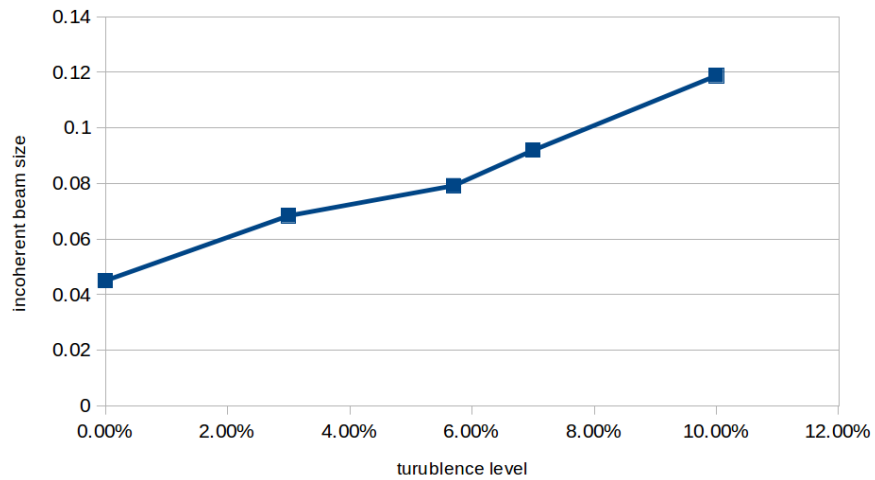


Figure 4.14: Incoherent part beam size

4.2 Study of edge turbulence effects on reflectometer signal

To study UFSR measurements in the presence of strong edge turbulence, we present a series of full wave calculations. We will focus on measurements when the cut-off position is located behind the edge turbulence layer. This will allow us to see the influence of beam widening and loss of coherency, caused by the turbulence, on the phase measurements. Few different cases will be highlighted. First, to separate the phase variations spectra produced by plasma edge and core turbulences we will show computation results where edge turbulence has only small wave-numbers and core turbulence has a gap in this region. As in the case of isotropic turbulence high k-numbers will be always projected on smaller ones, it is impossible to create a turbulence without small k-number part of the spectrum. In a second part Gaussian turbulence wave-number spectra will be processed in slab geometry. Methods to detect high edge turbulence will be investigated. Then the possibility to get information about single mode core turbulence in the case of strong edge turbulence will be studied. Using 2D geometry of Tore-Supra tokamak and experimental density and turbulence profiles we will look at effects of poloidal plasma curvature and Bragg back scattering.

4.2.1 Edge turbulence effects on reflectometer phase spectra using edge-core k-spectra separation

Here we have carried out swept reflectometry modeling with the "IPF-FD3D" full-wave code [65] for O-mode wave. The turbulence is assumed to be isotropic, homogeneous with small level (0.5% of cut-off density) of density perturbations in the plasma core and high level with Gaussian amplitude envelope in the plasma edge region (see figure 4.15). In order to discriminate the contribution from high level edge turbulence and from the core region we use mostly high wave-numbers for the core turbulence and only small wave-numbers for the edge turbulence (see figure 4.16).

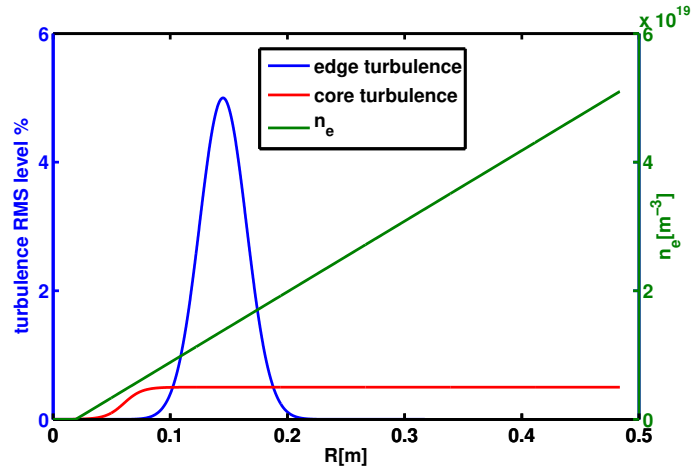


Figure 4.15: Density profile(green), edge turbulence RMS envelop with 5% maximum level(blue), core turbulence RMS envelop(red)

It is impossible to completely separate spectra of high and small wave-numbers for isotropic spectrum. Due to projection of modes to different directions each mode will have its trace in a direction of smaller wave-numbers (see appendix A). However we are still able to address phase variations spectra high k number to core turbulence. Computations were done for the same turbulence structure as in section 4.1.1 with $k_{max} = 0.1k_0$. The density profile depicted on figure 4.15. Unlike in last chapter, here we have wave cut-off positions.

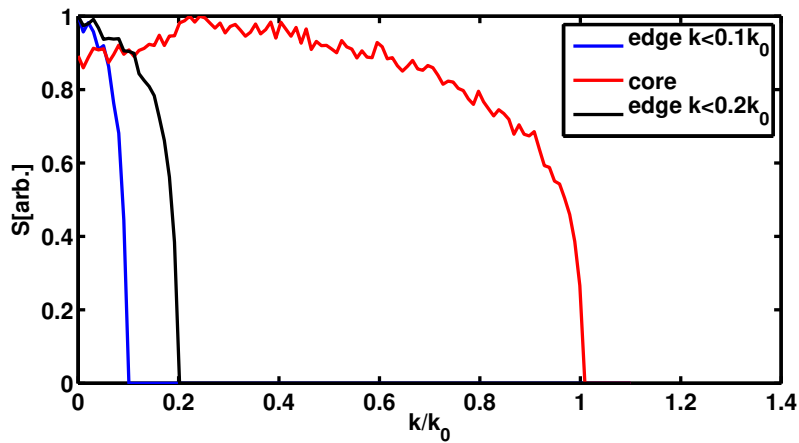


Figure 4.16: Core turbulence spectrum shape(red), edge turbulence spectrum shape for $k < 0.1k_0$ (blue), edge turbulence spectrum shape for $k < 0.2k_0$ (blue)

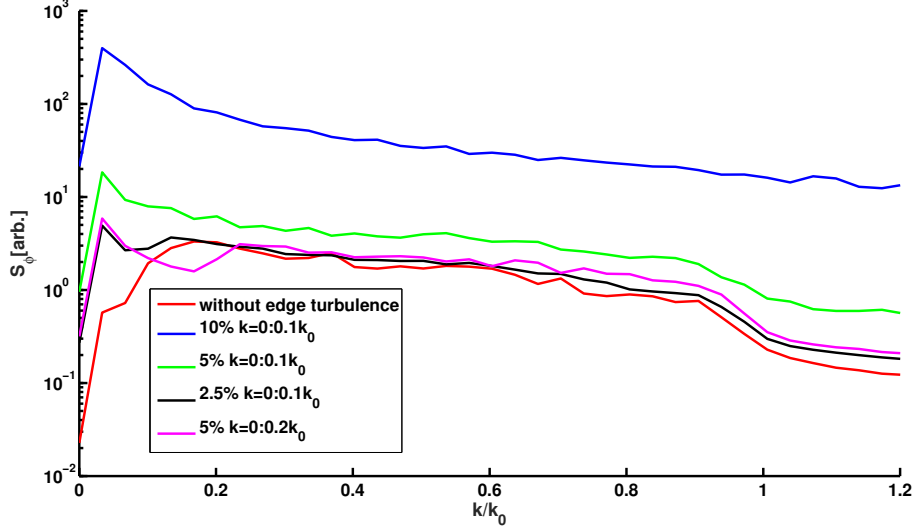


Figure 4.17: Phase fluctuation spectra: red - without edge turbulence, magenta - 5% edge turbulence level $k < 0.2k_0$, black - 2.5% edge turbulence level $k < 0.1k_0$, green - 5% edge turbulence level $k < 0.1k_0$, blue - 10% edge turbulence level $k < 0.1k_0$

One can see results of these full-wave computations on figure 4.17. As a result we notice that the reflectometry response from high k -numbers (plasma core) becomes higher when the edge turbulence level increases. Phase variation in Born approximation depends on scattered and unperturbed signals (see section 3.5). Strong small wave-number edge turbulence reduces unperturbed edge signal and introduces stronger scattered field. Moreover large scale turbulence structure can introduce phase gradient over a sweep (see figure 4.18). These phase gradients introduce a wide spectrum which decays in direction of high wave-numbers. More information can be found in appendix C. On figure 4.17 we can see that some effects start playing a role from very high values of turbulence amplitude. Non-linear effects with high values of density perturbations with long correlation length (3.6cm) result from the fact that widening of the incoherent part is quite small and major part of randomized phase signal can be received by antenna. However if the antenna position is far from the turbulence region, the incoherent beam becomes so wide that the antenna receives only a very small part of it. As the incoherent beam widening increases with shorter correlation length of the turbulence, wider spectrum of turbulence does not change the phase spectrum up to higher values of perturbations amplitude and thickness of the turbulent layer (magenta curve in figure 4.17). This means that in most of the cases, without back scattering regimes, edge turbulence does not break the linear approximation assumption when probing the plasma core region. In these cases we can use the analytical model (section 3.5) to determine the scattered field and the resulting phase variations. This result was found with relatively small thickness of turbulence layers (16 vacuum wavelengths). If the

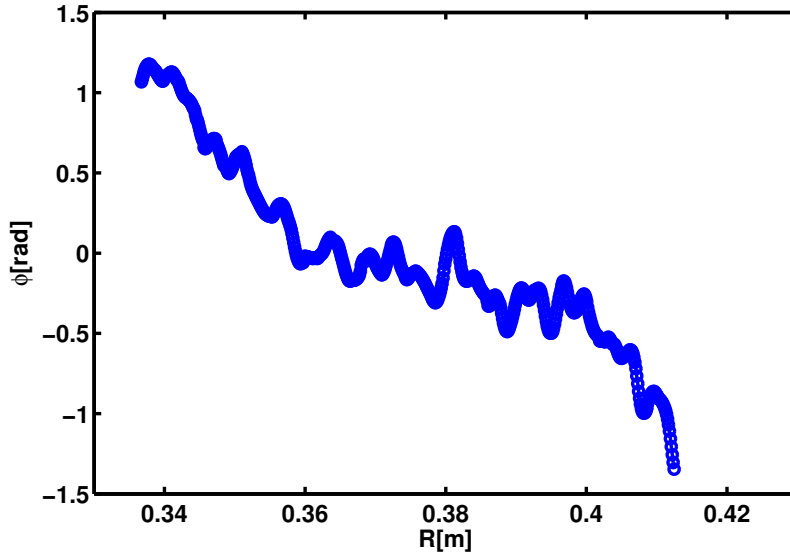


Figure 4.18: Phase variation sample for 10% edge turbulence level $k < 0.1k_0$

turbulence layer is thicker it decreases the limit of turbulence amplitude up to which the edge turbulence does not affect core measurements.

4.2.2 Edge turbulence effects on reflectometer signal in slab geometry

After crossing the edge turbulence region, the probing beam suffers some radial and poloidal change of the phase and widening. To investigate how the edge turbulence region affects core reflectometry measurements and find a way to identify in which cases the edge turbulence plays a role, we will study the reflectometer responses for a linear plasma density profile (see figure 4.19) and realistic density fluctuation spectrum and amplitude in slab geometry. Computations were performed using ordinary mode wave. In these computations the density fluctuations are created by superimposing two different turbulence maps. First there is background turbulence (red curve in figure 4.19) which is distributed everywhere in the plasma. This turbulence is homogeneous, isotropic and has a Gaussian k-spectrum with a correlation length of 6.8cm^1 . The RMS amplitude of these perturbations equals to 0.5% of the maximum swept frequency cut-off density n_c . An edge turbulence map with a Gaussian amplitude envelope centred in the edge region is added to the background turbulence (blue curve on fig.4.19). The edge turbulence spectrum also has a Gaussian shape. Its correlation length is of 3.4cm. The correlation length values were chosen in agreement with the range of possible correlation lengths typically measured in Tore-Supra plasmas [57]. Turbulence maps are

¹correlation length definition is different from Zadvitskiy PPCF **60** 025025 (2018)

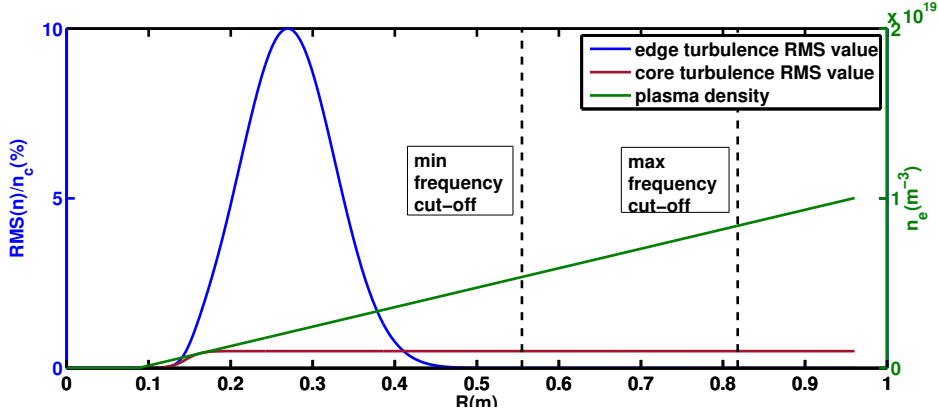


Figure 4.19: Radial plasma density profile (green) and turbulence level, composed of edge turbulence root mean square value (blue) and background turbulence root mean square value (red)

generated using inverse Fourier transform of a 2D spectrum with random phase for each mode. To adjust 2D wave-number spectra of isotropic turbulence to the desired 1D turbulence spectrum, an iterative method was used (see appendix A). To see the effect of the edge turbulence level, the reflectometer response was computed in 2D poloidal cross-section with the IPF-FD3D full wave code [65] for different edge turbulence levels. The same signal was computed with the simplified reciprocity theorem approach (presented in section 3.5.2). Here we probe the region around $R = 75\text{cm}$, with maximum frequency $F_{max} = 26\text{GHz}$. A snapshot of the electric field distribution with slab geometry density profile is depicted on figure 4.20. First, we will compute the phase fluctuations spectrum. On fig.4.21 one can see the phase fluctuation spectrum which is specifically analysed for turbulence k-spectrum reconstruction.

The spectra were averaged over 50 computations with different turbulence realizations. The number of 50 was chosen as a good compromise to extract the relevant information while keeping the computation time acceptable. We can see that the phase fluctuation spectrum carried out with the simplified reciprocity theorem approach doesn't change very much as long as the edge turbulence peak amplitude is below 7.5%. When the maximum of the edge turbulence reaches 10% of the cut-off density, the phase fluctuation spectrum amplitude computed with the full-wave code is more than two times higher than without edge turbulence. However the shape of the spectrum doesn't change significantly and the simplified reciprocity theorem method reproduces it well. Here one can see that nonlinear edge turbulence effects play a major role in the signal phase variations, and the simplified reciprocity theorem method is unable to describe these effects. This result means that assuming that the phase spectrum is connected only to cut-off vicinity leads to an overestimation of the turbulence level and the impossibility to see any signature of the strong edge turbulence.

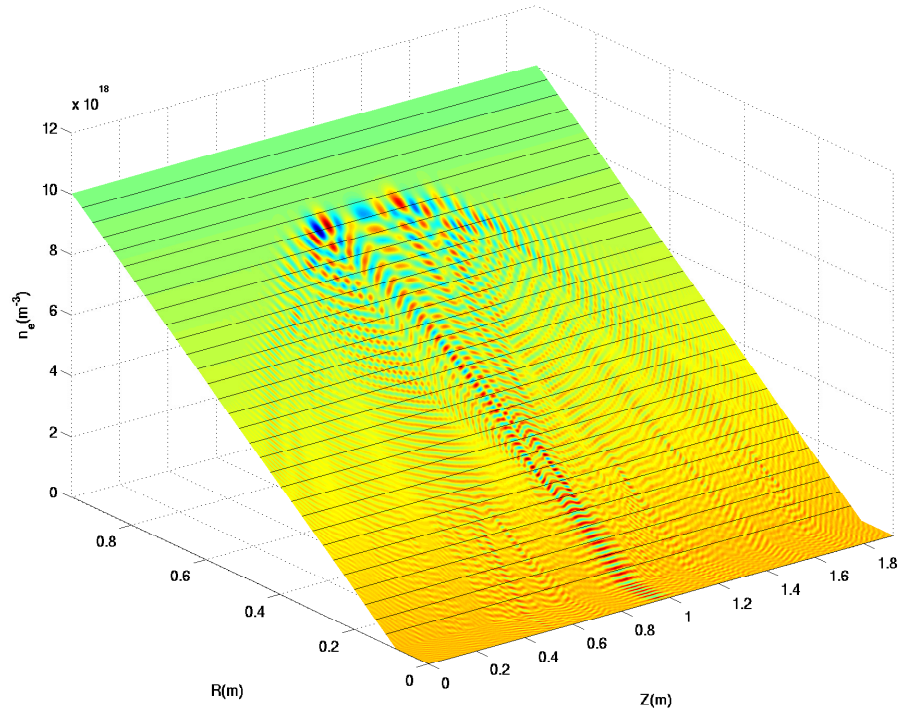


Figure 4.20: Probing beam electric field map computed with turbulence printed on density profile ($rms(\delta n) = 10\%n_c$) (computed with FD3D full-wave code)

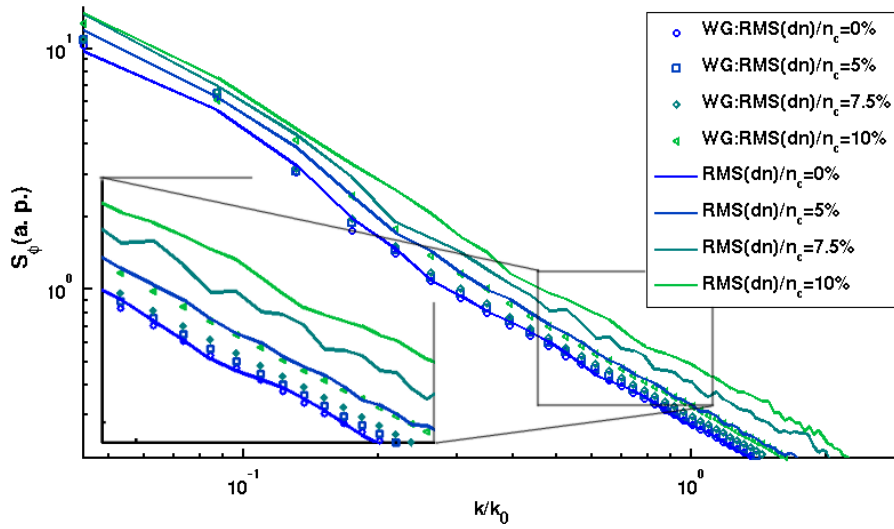


Figure 4.21: Phase fluctuation spectrum computed using the simplified reciprocity (spread points) and the full wave code (continuous lines), k_0 is the maximum frequency vacuum wave-number

Using USFR signal amplitude "A" analysis it is possible to extract more information about turbulence level and correlation length. For these analyses we use a technique based on receiving the signal simultaneously in a poloidal array of antennas. Such a technique has been applied on TEXTOR and ASDEX-Upgrade tokamaks and new Wendelstein 7-X stellarator for the measurements of the poloidal plasma rotation and turbulence correlation time with a fixed frequency reflectometry diagnostic [89,90,91]. With this setup we can look on the average received signal amplitude decay for the maximum swept frequency (as shown in fig.4.22). The widening of the probing beam

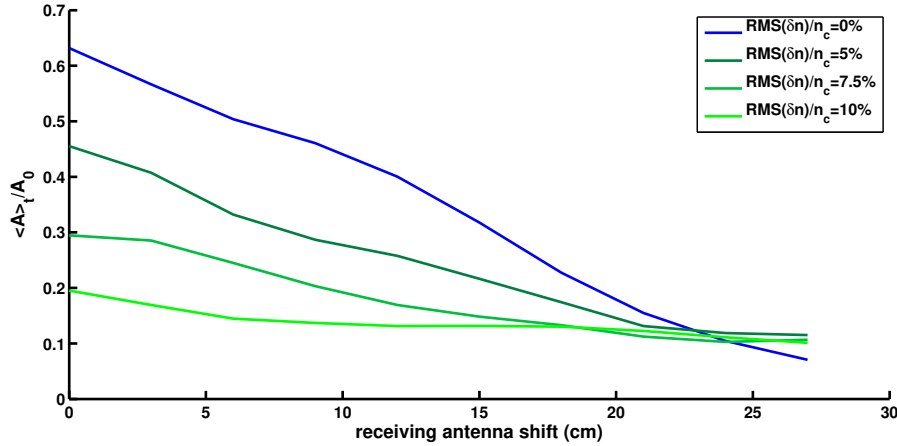


Figure 4.22: Averaged signal amplitude received by the receiver antenna as function of the poloidal antenna positions. A_0 is the emitting antenna amplitude

in that case can be estimated from the theory [84]. Another way to extract information about the edge turbulence using multi-antenna configuration is to look at the USFR signal amplitude variation spectrum.

$$S_A = \left| \left\langle \int [A - \langle A \rangle_R] \exp(-ikR) dR \right\rangle_t \right| \quad (4.7)$$

Where $\langle \dots \rangle_R$ and $\langle \dots \rangle_t$ are averaged over the radial cut-off position and over the time (in the case of computation, over turbulence realizations series). Such spectra are illustrated on fig.4.23. When the receiving antenna stays at the same place as the emitting one we can see a peak. (figure 4.23). This peak near $k = k_0$ is a signature of the edge turbulence effects. When edge turbulence is absent this peak is not observed. Following the Bragg rule $\vec{k}_a = \vec{k}_i + \vec{k}_{turb}$ we can see that the peak close to $k = k_0$ is connected to enhanced scattering in the edge region. With the receiving antenna shift we also see a shift of this peak in the direction of smaller wave-numbers. To efficiently receive the back scattering signal with a misaligned receiving antenna the probing beam should make a turn. As the beam propagates deeper through strong edge

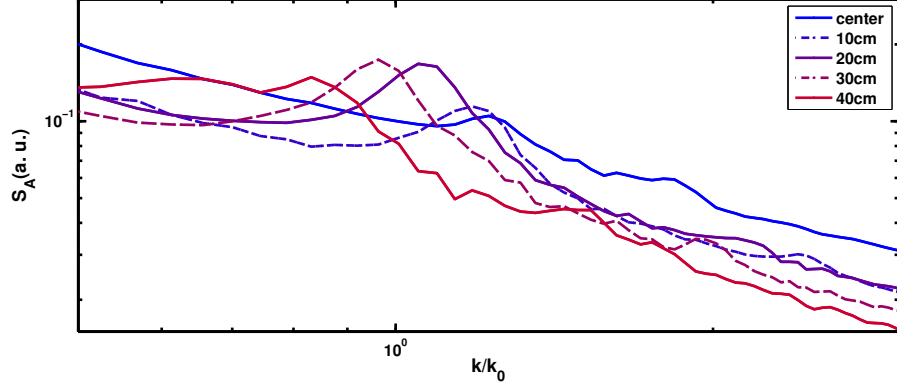


Figure 4.23: Signal amplitude variation spectrum at different receiver poloidal positions. The maximum RMS edge turbulence amplitude is 10% of the cut-off density

turbulence layer the probability to get stronger probing beam deviation from the edge turbulence poloidal spectrum increases. Deeper in the plasma means smaller probing wave-numbers, which we see with the antenna shift. These peaks also appear in the amplitude variation spectrum when the edge turbulence reaches a $RMS(\delta n)/n_c = 7.5\%$ but they are smaller and don't move much with the receiving antenna poloidal shift.

4.2.3 Mono wave-number mode observation through strong turbulence level

To understand how the wave behaves between the cut-off and edge turbulence layers and check the possibility to detect single mode structures such as GAM [93] or quasi-coherent mode [?] through strong edge turbulence ($RMS(\delta n)/n_c = 10\%$), simulations were carried out in the same conditions than in the previous section replacing the core turbulence by a localized single mode with Gaussian shape amplitude envelope with the same size as edge turbulence envelope and maximum value of 0.5%. It is situated between the highest frequency cut-off position and the edge turbulence with the center near $n = 0.75n_c$ (see figure 4.24). The turbulence has a single wave-number chosen to fulfil the Bragg scattering condition ($k = 0.9k_0$). This mode is tilted with an arbitrary angle of 15° with respect to the probing beam direction.

Figure 4.25 shows the phase variation spectrum. One can see that it is possible to detect the coherent mode through a strong turbulence layer in the edge region. To get a smoother curve here 100 runs with different turbulence realizations were used. It can be noticed from equation (3.57) that the diagnostic is more sensitive to core turbulence compared to edge turbulence with the receiving antenna shift. This is due to the fact that the receiving and emitting antennas electric fields have stronger overlap in the core region than at the edge when antennas are not aligned. The spectral peak associated

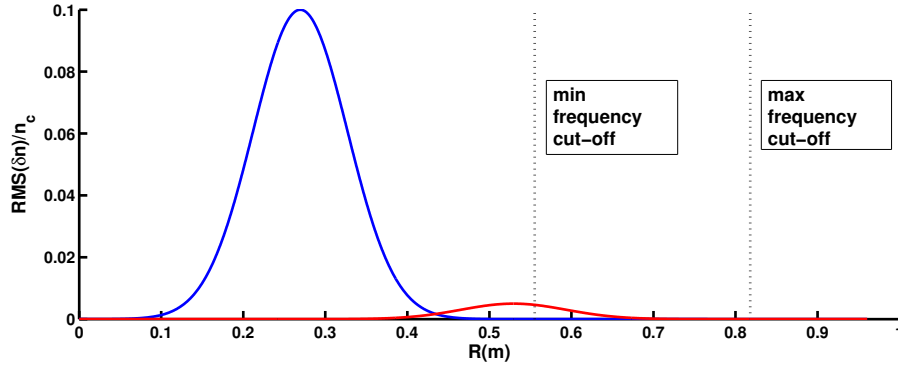


Figure 4.24: RMS value amplitude envelopes of Edge turbulence (blue), and core turbulence (red). Maximal and minimal frequency cut-off positions

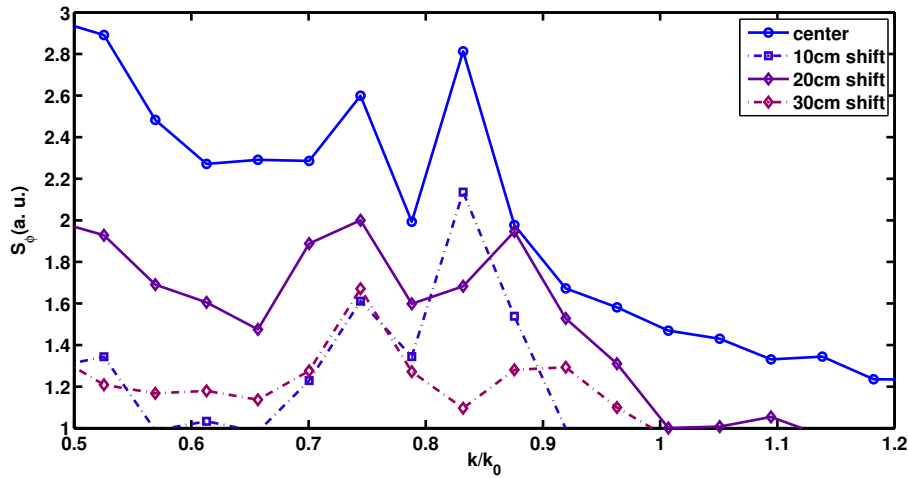


Figure 4.25: Signal phase fluctuation spectrum at different receiver antenna poloidal positions. The maximum RMS edge turbulence amplitude is 10% of the cut-off density

with the coherent mode is double. As we are looking on tilted mono mode turbulence wave-number projection on injection direction we see little bit smaller wave-number . Figure 4.26 shows the amplitude fluctuation spectrum for different receiving antenna position. We can see that the coherent mode is clearly observed on the spectrogram even through very high levels of edge turbulence. Some small peaks near $k/k_0 = 1.6$ can be seen. These peaks can be explained by second unstable zone of Mathieu equation. One can notice that the main peak in the amplitude variation spectrum ($k/k_0 = 0.8$) is doubled as well as for the phase variation spectrum. First, the smallest wave-number peak does not change much in amplitude and position with the antenna shift. Second, higher wave number peak decreases in amplitude and moves towards the direction of higher wave-numbers with the antenna misalignment. To analyse the nature of this

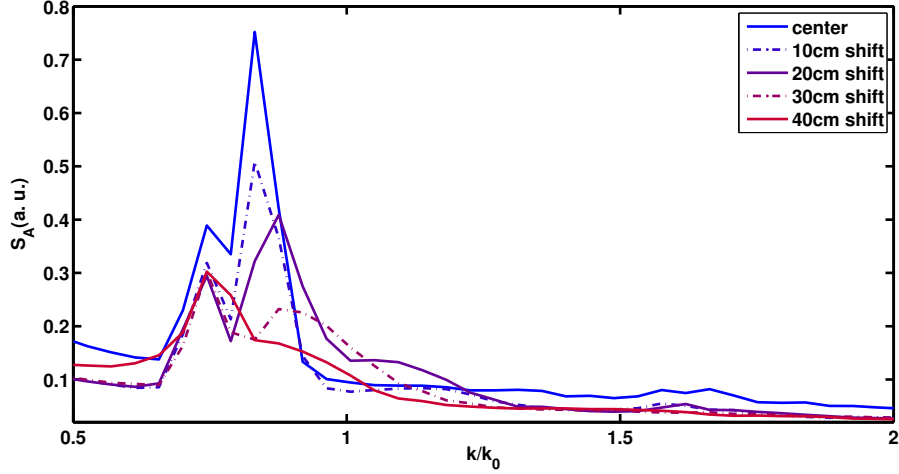


Figure 4.26: Signal amplitude fluctuation spectrum computed at different receiving antenna positions. The maximum RMS edge turbulence amplitude is 10% of the cut-off density

peak behaviour let us look at the complex signal spectrum:

$$S_c = \left\langle \left| \int A \cdot \exp(i\phi) \exp(-ikR) dR \right| \right\rangle_t \quad (4.8)$$

Such spectra are shown on figure 4.27. In the complex signal spectrum it is possible to discriminate signals corresponding to different time of flights. In the same way that the phase time slope $d\phi(\omega)/dt$ allows to measure poloidal plasma velocity by Doppler reflectometry, here $d\phi(\omega)/d\omega$ allows to separate signals by the time of flight as this value grows with the time of flight. The larger the time of flight of the component of the reflected signal, the smaller the associated wave-number k at which it is observed in the spectrum. On fig.4.27 we can see a large central double peak (1 on the figure 4.27) and 2 smaller ones on both sides (2 and 3 on the figure). The big peak corresponds to main scattering from the cut-off region. As the coherent turbulence is situated between the edge turbulence and the cut-off layer it generate smaller peaks on the sides of the spectrogram. The right peak (2 on the figure 4.27) results from the first time the probing beam crosses the coherent turbulent layer. It is also possible to see smaller peaks from the edge turbulence as in the previous section 4.2.2. The left peak (number 3) comes from scattering after reflection by the cut-off layer. This makes us understand the nature of the two peaks observed in the amplitude and phase variation spectra. It is clear that the peak at fixed position (on fig.4.26) corresponds to the second scattering and that the "moving" peak results from the first scattering. The peak displacement can be explained by the Bragg scattering rule. During the second scattering occurrence the probing beam has much wider direction range. This

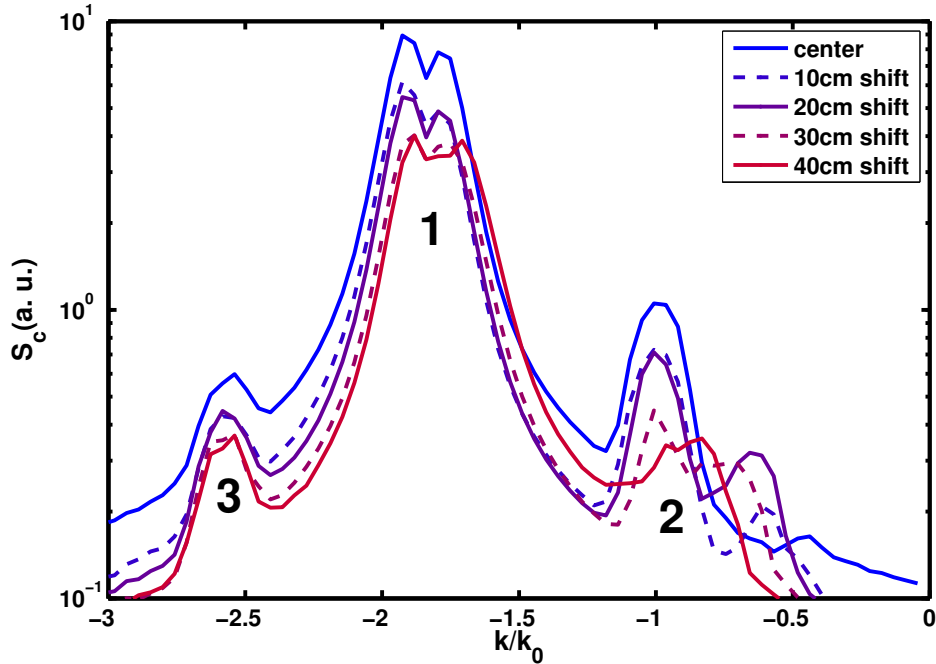


Figure 4.27: Complex signal fluctuation spectrum computed at different receiving antenna poloidal positions. The maximum RMS edge turbulence amplitude is 10% of the cut-off density

contributes to increase the wave scattering efficiency and makes the peak visible even when probing wave amplitude is much smaller after cut-off reflection. For the first scattering occurrence, as the turbulence wave-number is fixed, the Bragg scattering rule is satisfied for slightly higher wave-numbers. When the receiving antenna is shifted, the effective direction to receive scattered signal is changing and the scattering wave-number value is increasing. However, the absence of the unique beam direction after the cut-off reflection makes the second scattering spectral peak to be stationary.

4.2.4 Edge turbulence effects on reflectometer signal for Tore-Supra 2D profile

The poloidal plasma curvature and steeper density gradient in the edge region can change the typical influence of the edge turbulence on core radial wave-number measurements using UFSR. In this section instead of slab geometry we perform simulations with a realistic 2D geometry of the Tore-Supra tokamak (see figure 4.28). We use a typical experimental density profile, and the turbulence spectrum and amplitude used are based on the calculations done with a Helmholtz equation solver in a closed loop algorithm [94]. Figure 4.29 shows the turbulence spectrum that we used in these computations. To simulate realistic turbulence, three isotropic homogeneous turbulence

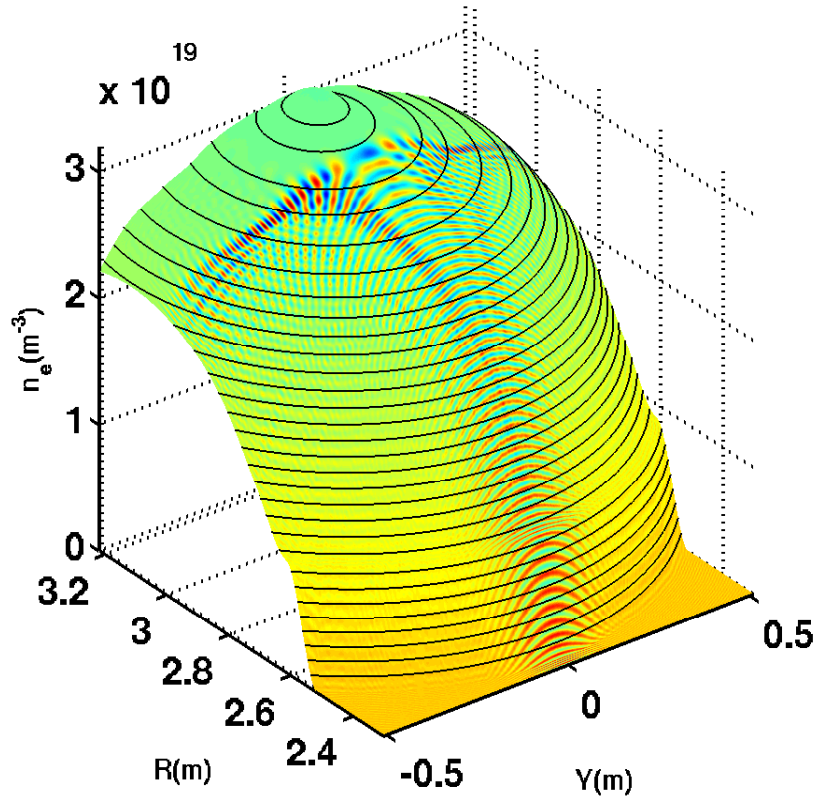


Figure 4.28: Contour maps of the probing wave field superimposed with a 3D plot of the density profile

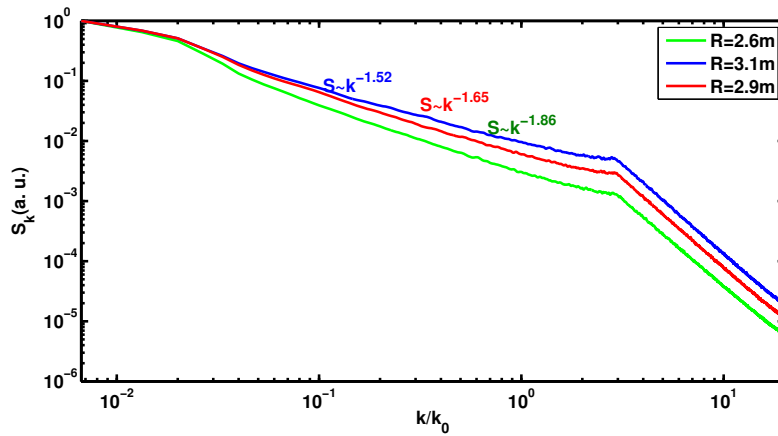


Figure 4.29: Turbulence spectrum at different radial positions

maps corresponding to different radial zones were mixed together using 2D shaped envelopes for a smooth spectral transition. The 2D turbulence amplitude envelop depicted in figure 4.30, is based on experimental estimations [94] and has been fitted with

the following function:

$$RMS(\delta n) = (a + b * \exp((x - x_m)^2/2\zeta)) * (0.5 * \tanh((x - x_t)/\zeta_2) + 0.5) \quad (4.9)$$

where a, b, ζ, ζ_2 are fitting constants. The fitting function (4.9) allows us to choose the edge turbulence amplitude by changing parameter b . In the simulation presented here

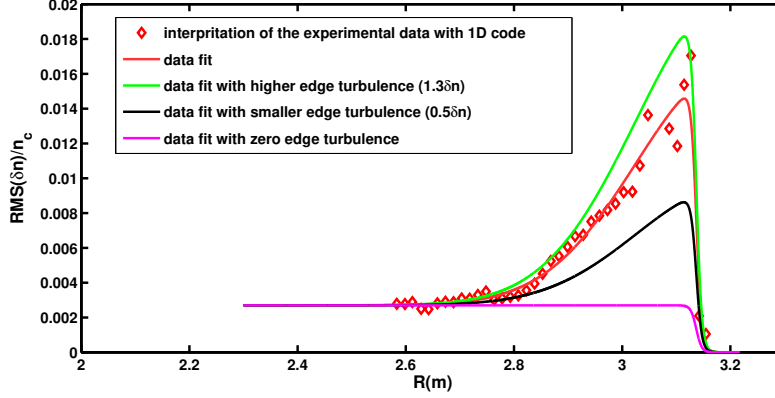


Figure 4.30: Spatial evolution of the density fluctuations profiles used as input for different cases of simulation [94]

the maximum edge RMS amplitude is equal to 1.9% of the highest probing frequency cut-off density. The frequency sweeping covers a radial zone of 12cm in the plasma core. Another difference with the slab geometry computations is the turbulence correlation length. Here the edge turbulence correlation length is 12mm. Such a small correlation length can cause strong Bragg back scattering. The poloidal plasma curvature makes the incident beam wider. The probing beam amplitude decays faster up to the cut-off vicinity region, which makes the diagnostic more sensitive to the edge turbulence than to the core turbulence. On future large scale devices such as ITER the probing beam attenuation will be more pronounced which will increase even more the sensitivity to the edge turbulence layer. On figure 4.31 is represented the signal phase variation spectrum for different edge turbulence amplitudes computed in a 2D toroidal cross-section both with the IPF-FD3D full-wave code and simplified reciprocity theorem approach. Here we have the case of strong Bragg back scattering. Scattering from the edge turbulence strongly changes the phase variation spectral amplitude. The simplified reciprocity theorem method fails to reliably describe the influence of the edge turbulence. Now let us see if it is possible to detect the presence of the edge turbulence amplitude peak in the reflectometer amplitude variation spectrum (see fig.4.32). We can note that even with small turbulence levels it is possible to see a strong edge turbulence signature (the k-spectral peak near $k/k_0 \approx 1$ observed in the spectrum) in the case of small turbulence correlation lengths and poloidal plasma curvatures. With a receiving

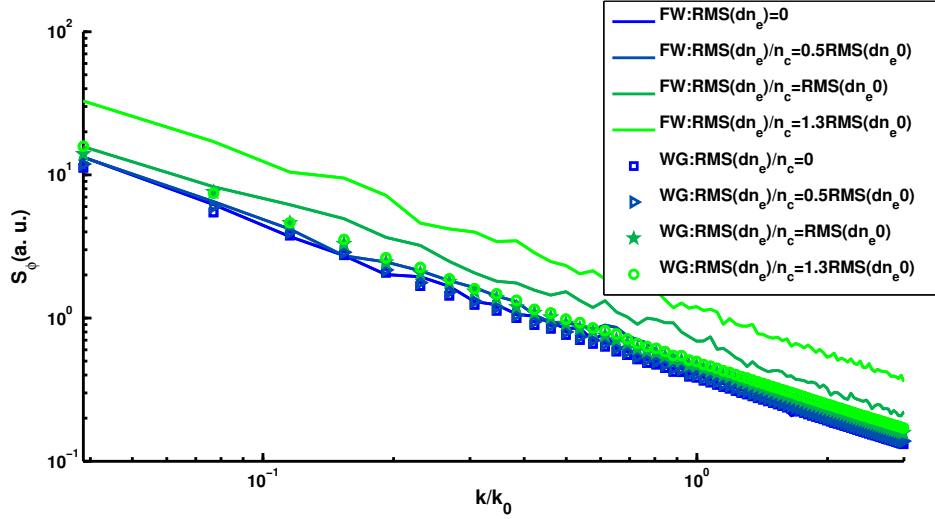


Figure 4.31: Signal phase variation spectrum computed for different edge turbulence amplitudes

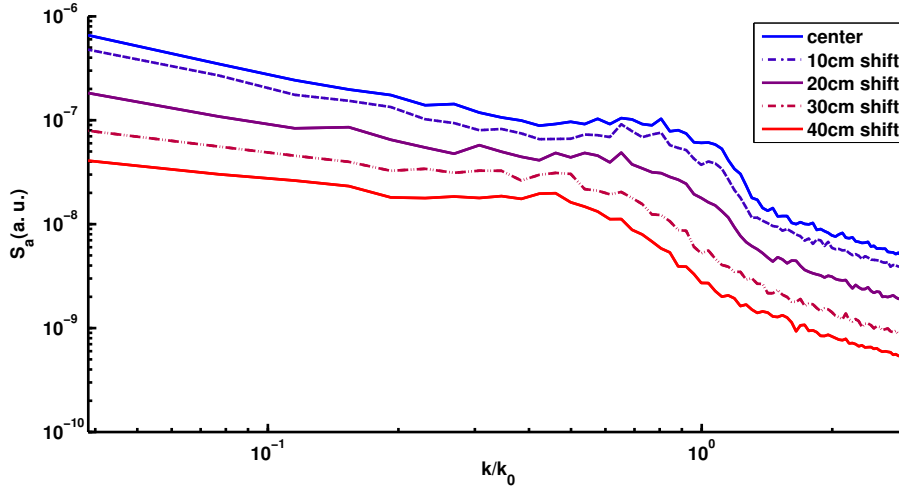


Figure 4.32: Signal amplitude variation spectrum computed at different receiving antenna poloidal positions in the case the highest edge turbulence level ($RMS(\delta n/n_c) = 1.8\%$)

antenna poloidal shift the k -spectral peak shifts towards the direction of smaller wavenumbers, as observed in previous cases. With such a correlation length and turbulence level, the beam widening is not significant. However the beam widening produced by the poloidal plasma curvature can have also the same effect on the peak movement than a widening of the turbulence poloidal spectrum. In this case it is not possible to measure turbulence properties by looking on the averaged receiving amplitude in antennas at different poloidal positions.

4.3 Discussions

Results obtained in this section show the potential of turbulence characterization with USFR. When the beam crosses a turbulent layer it can be represented as superposition of 2 beams: one for which the phase and shape are conserved and another one which has random phase. It was found that the phase variations spectrum is very sensitive to edge turbulence when core turbulence is measured. In the case of small turbulence correlation length, strong attenuation of the coherent beam part takes place, small correlation length turbulence generates Bragg-backscattering. These effects change phase variation spectrum in core measurements. It was found that analysing the reflectometer amplitude spectrum it is possible to get information about the edge turbulence. A new swept reflectometry detection method with multiple receiving antennas was proposed. Using this technique it is possible to see not just the amplitude variation spectral peaks but also see a change in the peak position. This change can be explained by Bragg-backscattering rule and beam propagation through the edge turbulent layer. However for good edge turbulence characterization in experiment, a series of modelling should be performed to investigate absolute values of the peak amplitude and spectral shift. Using spectral peak position shift it might be possible to calculate the position of the turbulent layer. However as scattering process in non-linear regime is hard to analyse analytically, a series of modelling possibly can help in these peak analysis. To recover absolute values of phase variation and amplitude in experiments, modelling should be done in 3D. This statement can be explained by Born approximation solution in the reciprocity theorem approach. Unperturbed signal's level will decrease in relation to scattered signal because of toroidal beam widening. This can change the amplitude of phase and amplitude variations.

Chapter 5

Application to gyro-kinetic simulations data and experimental measurements

In this chapter we will have a look at the applications of methods described in previous chapters. In the first section we will apply IPF-FD3D code on results of GYSELA gyro-kinetic code [95] computations for correlation length measurements in the Tore-Supra tokamak. In the second chapter, IPF-FD3D code will be applied to ASDEX-Upgrade density profile with experimental (discharge 31287) turbulence spectra.

5.1 Synthetic diagnostic application to GYSELA gyro-kinetic simulation

To validate gyro-kinetic codes their data should be compared with experiments. For this, synthetic diagnostic will be applied to get virtual multichannel fixed frequency reflectometer response. This data then can be compared directly with experimental results. Here GYSELA code data was used. This code was applied to Tore-Supra discharge number 45511. GYSELA is a flux-driven 5D gyro-kinetic code suitable to model typical features of plasma turbulence such as zonal flows or Ion Temperature Gradient (ITG) modes [96]. The turbulence from GYSELA (see figure 5.2) used as input of our full-wave simulations are typical of Tore Supra L-mode Deuterium discharges. X-mode waves were launched in the plasma. Cut-off frequencies and probing frequencies are presented in figure 5.1. The level of density fluctuations is ballooned in the mid-plane low field side region and larger in the mid-radius region ($2.55m < R < 2.95m$) (see figure 5.3). In this section we will focus on radial correlation length measurements.

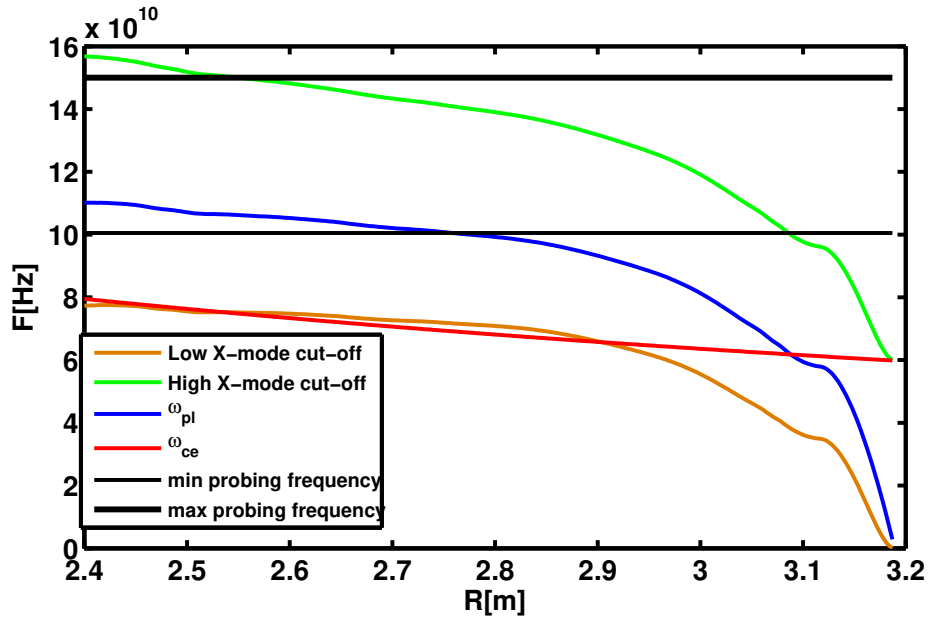


Figure 5.1: Cut-off frequencies for typical Tore-Supra discharge number 45511

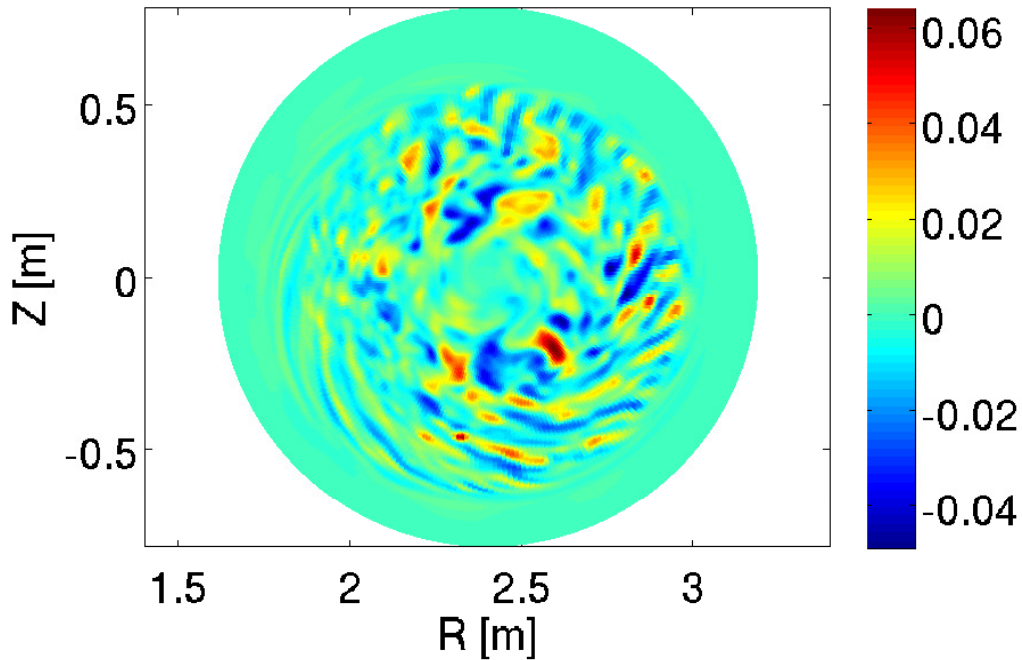


Figure 5.2: Turbulent density variation $RMS(\delta n)/n$ from GYSELA

Using IPF-FD3D code 100 frequencies were launched to the plasma (see figure 5.1). Unfortunately turbulence time step between turbulence realisations used in full-wave computations was too long to successfully follow the phase changes. However the signal

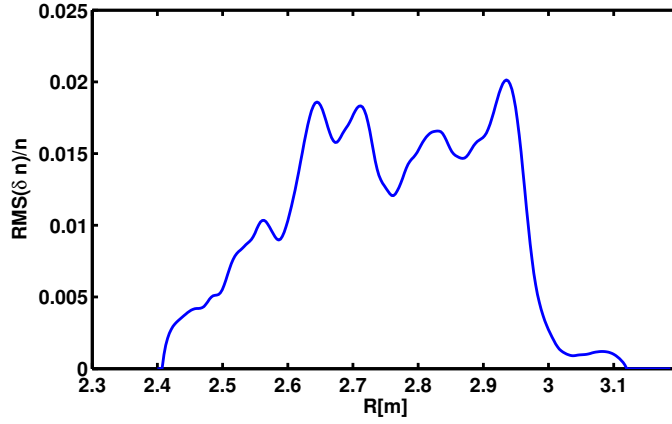


Figure 5.3: radial RMS turbulence amplitude profile $RMS(\delta n)/n$

amplitude doesn't need to be unwrapped and can be used for correlation length analysis.

Turbulence fluctuation time variation on the mid-plane low field side probed by the reflectometer is depicted on figure 5.4(left). The reflectometer signal amplitude varia-

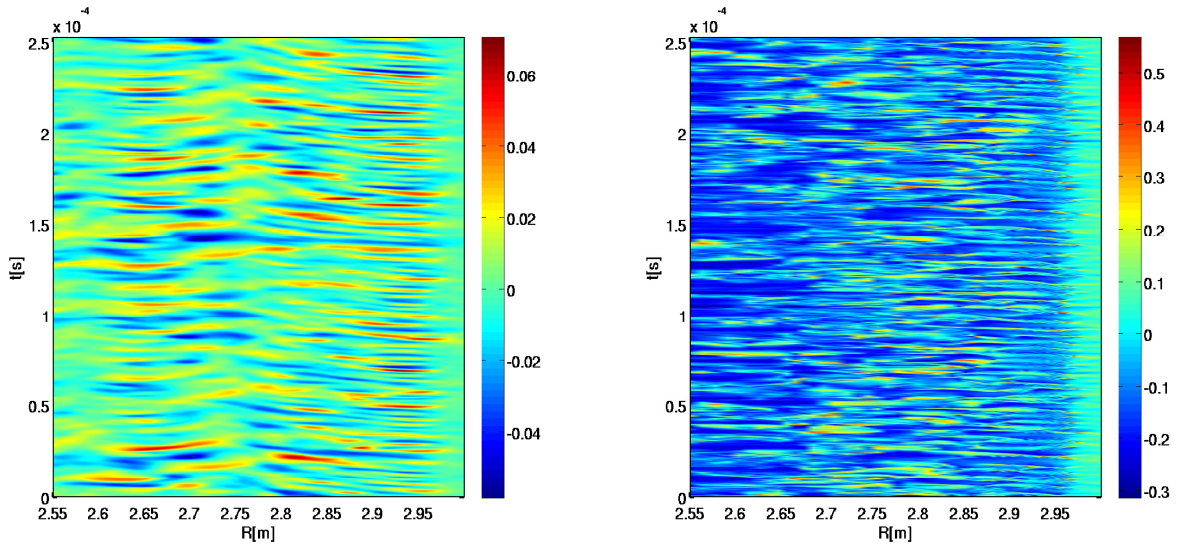


Figure 5.4: Turbulence density fluctuation time variation on mid-plane low field side probed by the reflectometer(left), Reflectometer signal amplitude variation(right)

tion A is shown on the figure 5.4. Using this signal cross-correlation function with zero time separation between signals were computed.

$$CCF(0, \delta R) = \frac{\int A(R, t)A(R - \delta R, t)dt}{\sqrt{\int A(R, t)^2 dt \int A(R - \delta R, t)^2 dt}} \quad (5.1)$$

As before, the correlation length is defined as full width of cross-correlation function half amplitude. Correlation function computed from density variation itself and reflectometer signal amplitude variation can be found on figure 5.5. Correlation function

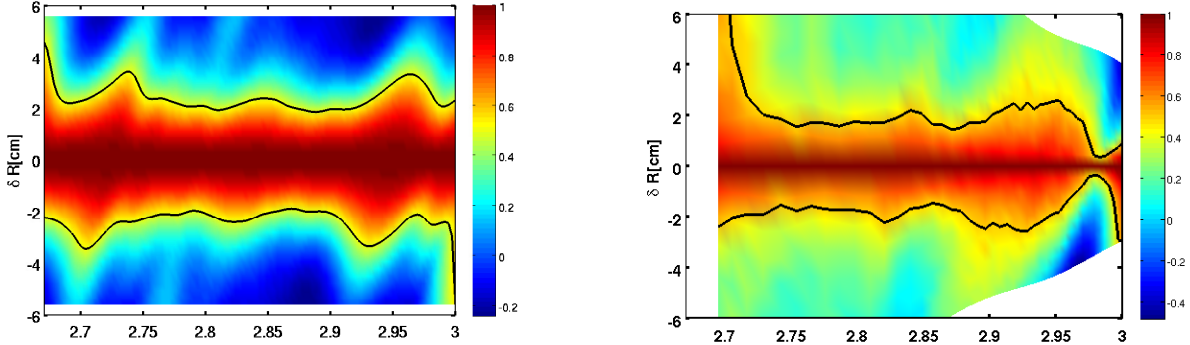


Figure 5.5: Cross-correlation function computed from turbulent density variation(left), signal amplitude variation(right) with half amplitude lines(black lines)

obtained from these plots shows a good agreement between turbulence correlation length and reflectometer signal amplitude variation correlation length (see figure 5.6). Reflectometer signal radial positions here were taken cut-off position computed with

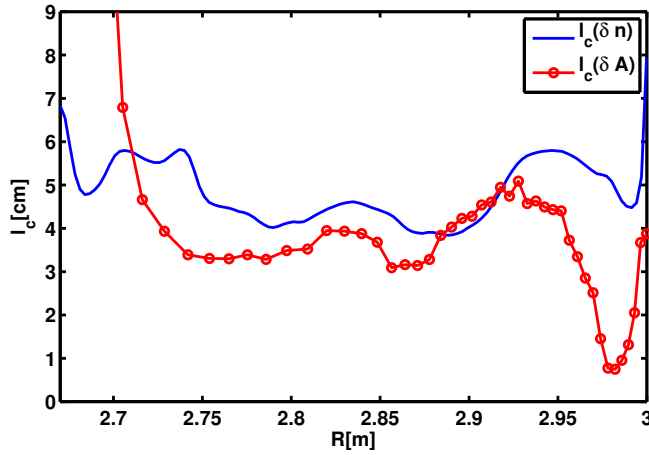


Figure 5.6: radial RMS turbulence amplitude profile $RMS(\delta n)/n$

the mid-plane density profile. In the reality, because of poloidal curvature and beam width, the cut-off layer is not limited by one point. Because of magnetic field X-mode cut-off doesn't curve enough to follow density isolines. Because of this, the reflectometer does not collect information from one radial position. This moves the effective cut-off position closer to the reflectometer antennas. On figure 5.6 we see some small, about 2 cm, displacement of the signals. Overall discrepancy between measured correlation lengths and turbulence ones is small. However this particular GYSELA simulation did

not include edge turbulence which may change the reflectometer response.

5.2 ASDEX-Upgrade UFSR synthetic diagnostic

USFR which was developed in Cadarache [97] was used in the ASDEX-Upgrade tokamak. The main advantage of this diagnostic is related to the sweeping time of $1\mu s$. Such a short sweeping time is smaller than turbulence characteristic time. That allows to measure the density profile and to get phase fluctuation with high spatial and temporal resolutions. USFR was used together with fixed frequency multi-channel reflectometry. This allows to get information on frequency spectra and density variation amplitude much easily using the theory presented in [83,98]. In this section we will use the results that were obtained by the closed loop algorithm for analysis of discharge number 31287. Here 1D Helmholtz equation solver was used as synthetic diagnostic. Cut-off frequency together with used probing frequencies are depicted on figure 5.7. To take into account realistic turbulence geometry one should create inhomogeneous

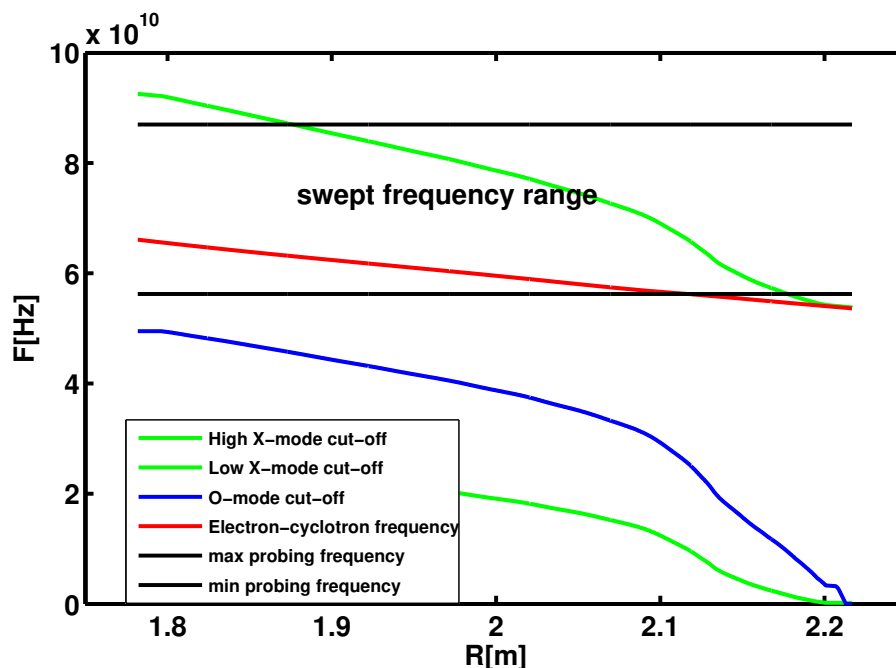


Figure 5.7: ASDEX-Upgrade cut-off frequencies profile for discharge number 31287, maximum and minimum probing frequency range

turbulence where turbulent spectra will be a function of magnetic surface. To approximate magnetic surfaces structure we used Miller equilibrium approximation [99] which takes into account Shafranov's shift, triangularity and vertical elongation of magnetic surfaces. Magnetic surface index ρ was divided on 15 parts corresponding to the radial turbulence windows positions. More details on the method can be found in appendix

B. Resulting 2D turbulence map superimposed with density profile can be seen on figure 5.8. The turbulence spectrum for all 15 radial positions can be found on fig-

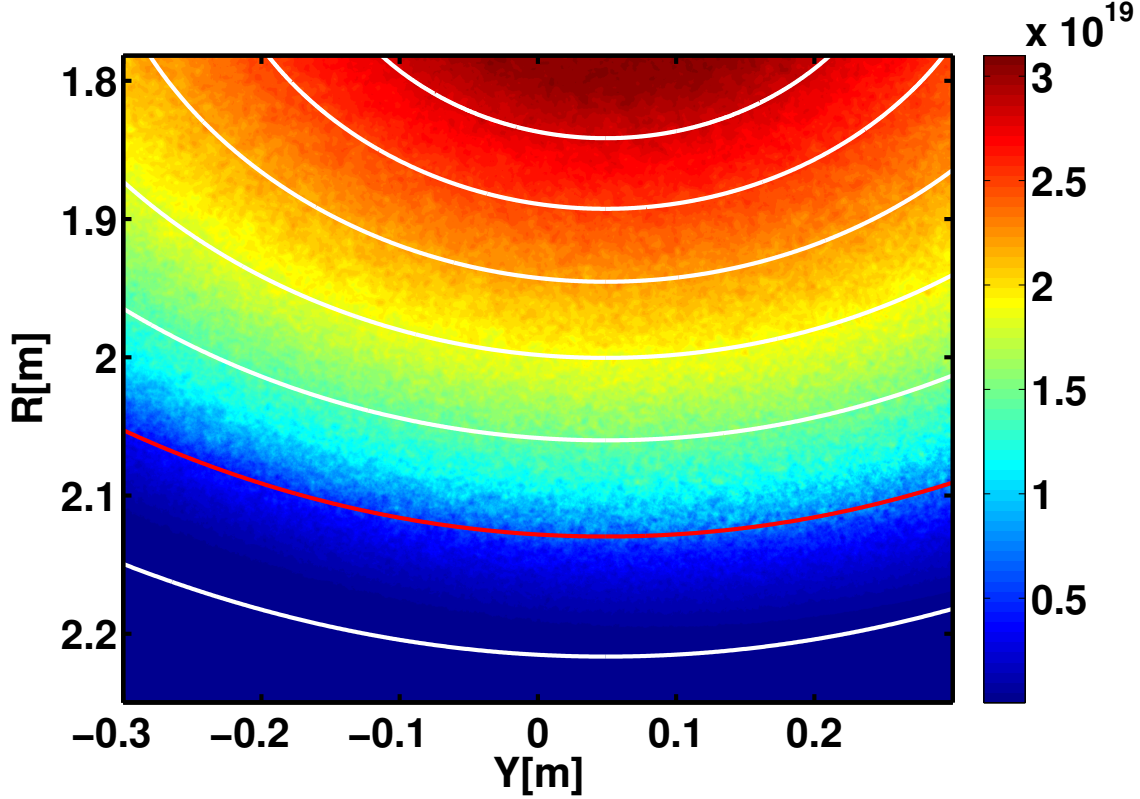


Figure 5.8: one of 2D density profile with the turbulence map used for computation (discharge number 31287). White lines are magnetic surfaces lines approximated by Miller equilibrium [99] with the last closed surface (red)

ure 5.9. This spectrum corresponds to turbulence with correlation length from 1 cm in the plasma core to 6 mm in the scrape-off layer region (SOL). Turbulence has an RMS amplitude envelop based on measurements with fixed frequency reflectometry (see figure 5.10). To calculate the phase variation spectrum 50 runs with different turbulence realization were used. Number 50 was chosen as a compromise between statistical error and computation time. As one can see density and turbulence profiles are not symmetrical with respect to the mid-plane. Receiving and emitting antennas are located at $R = 2.484m$, $Y = \pm 0.028m$. Both antennas are directed towards the position: $R = 1.937m$ and $Y = 0.000m$. The antennas beams have relatively long path inside the vacuum region. To reduce computational time we decreased the grid size and

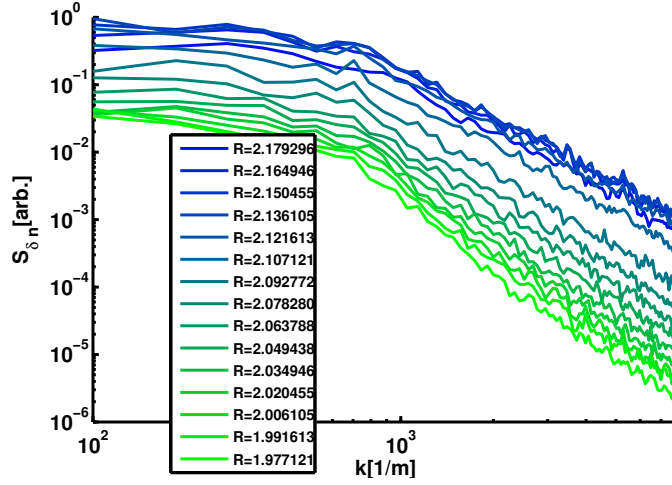


Figure 5.9: Turbulence spectra for different radial positions. Different amplitudes correspond to different RMS levels according to Parseval's theorem

introduced a shift in receiver Gaussian antenna pattern focus distance. It should be

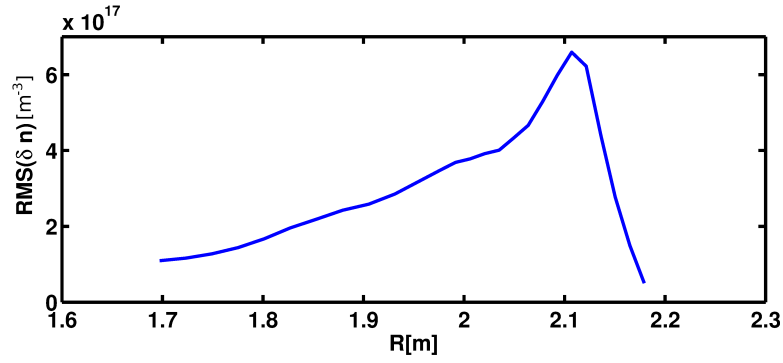


Figure 5.10: RMS value of density variation

admitted that even with density profile poloidal curvature, because of magnetic field, cut-off lines are almost straight. To compare computation methods in experiment case same computations will be performed using 1D Helmholtz solver and IPF-FD3D code.

5.2.1 Phase fluctuation and amplitude fluctuation spectra

The phase fluctuation power amplitude $\langle \delta\phi^2 \rangle$ computed using IPF-FD3D code is depicted on figure 5.11. Computations here were done using a given density perturbations level (figure 5.10) and using various reduced turbulence levels ($0.8\delta n$, $0.67\delta n$, $.05\delta n$, $0.33\delta n$, $0.2\delta n$). One can see that phase variation amplitude increases with turbulence level. However in some points, especially near the density perturbations amplitude peak ($R \approx 2.1$), the phase variation amplitude doesn't change with the turbulence level. Such a behaviour can be connected to statistical error due to a relatively small

number of density perturbation samples. One can find similar results of 1D Helmholtz solver on figure 5.12. Here we see much more pronounced phase variation amplitude in the edge region. With turbulence level drop, the phase variation level becomes flatter with the radius R . This means triggering of non-linear regime of 1D solution. The phase variation amplitude computed with 2D code is higher than the computed one using 1D code. This differs with our previous results (see section 3.5.3, figure 3.31).

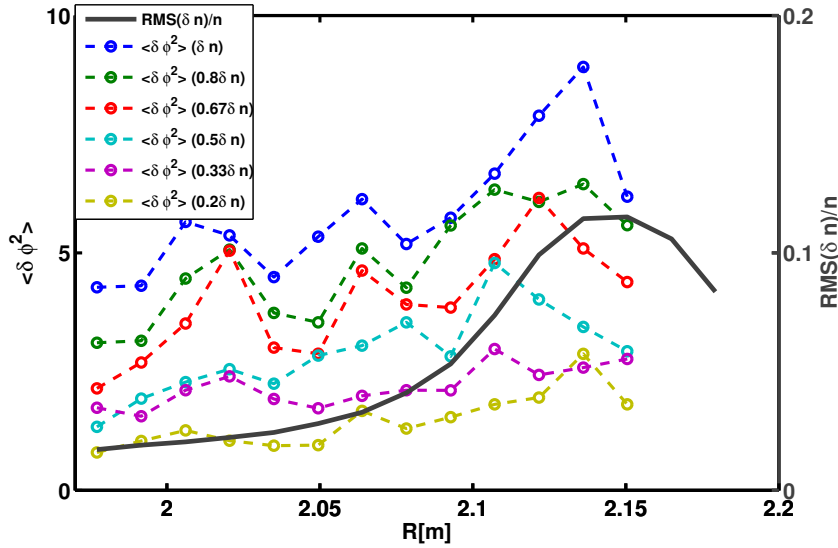


Figure 5.11: black - RMS relative density perturbation level, dashed lines - $\langle \delta \phi^2 \rangle$ computed in 2D with IPF-FD3D code for different turbulence levels

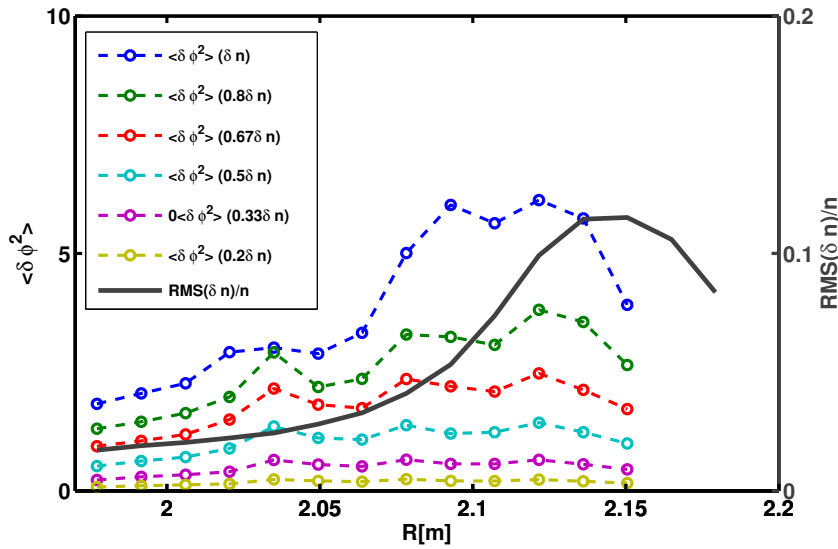


Figure 5.12: black - RMS relative density perturbation level, dashed lines - $\langle \delta \phi^2 \rangle$ computed with 1D Helmholtz equation solver for different turbulence levels

Due to high turbulence level, resonant wave trapping (see sections 3.2.2, 3.4) produces

π jumps in the reflectometer phase signal. To properly trace these jumps, very small frequency steps should be used. To do so we were facing some computational time limits and some phase jumps when we probe areas near and above edge turbulence amplitude peak are present in the computed signal. Phase jumps introduce very wide spectral noise which can hide wave-number spectral structure and affect correlation length measurements. The local phase gradient which was observed in section 4.2.1 also takes place here.

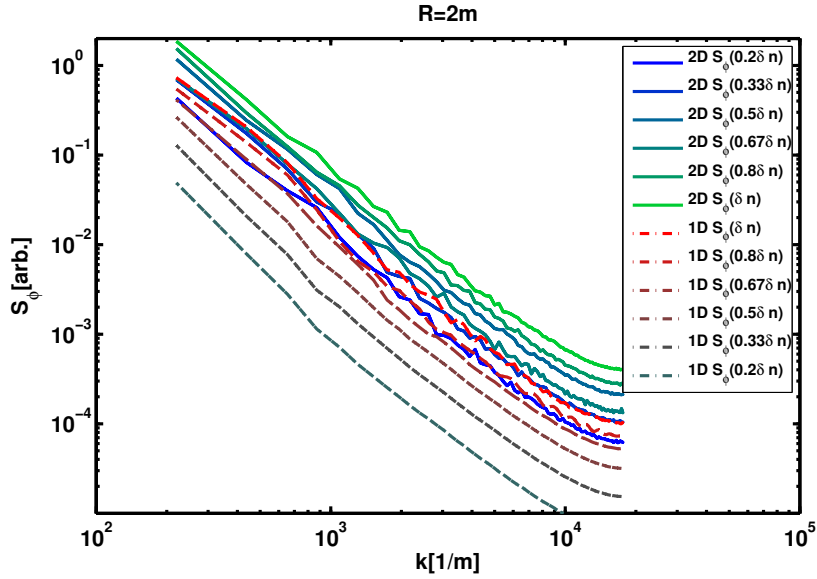


Figure 5.13: Phase variation power spectra obtained near $R=2m$ with different amplitude levels

Figures 5.13, 5.14 and 5.15 show phase variation power spectra computed in 2D with IPF-FD3D code and 1D Helmholtz solver for different δn . It can be noticed that 1D code is more sensitive to turbulence amplitude change. Spectral knee which is seen on the figure 5.9 is not present on spectra obtained using IPF-FD3D code. 1D Helmholtz equation solver phase fluctuation spectrum obtained near $R=2.07m$ has a knee near $k = 10^3 m^{-1}$, which is similar to turbulence wave-number spectra knee. This knee is more pronounced with smaller turbulence levels. Overall spectral shape is very similar for 1D and 2D computations. In the region behind the turbulence level peak ($R \approx 2.07m - 2.12m$) where strongest multi reflection takes place, the phase variations spectral shape and amplitude are almost identical for a given turbulence level. However in this region there are most frequent appearances of the phase jumps. The biggest differences in spectral shape between 1D and 2D computations were obtained near the relative turbulence level maximum (black curve on figure 5.11). On none of the phase fluctuation spectra we can see a spectral peak which would signify strong edge turbulence layer as it was observed in previous chapter with amplitude variations spectra. One can see

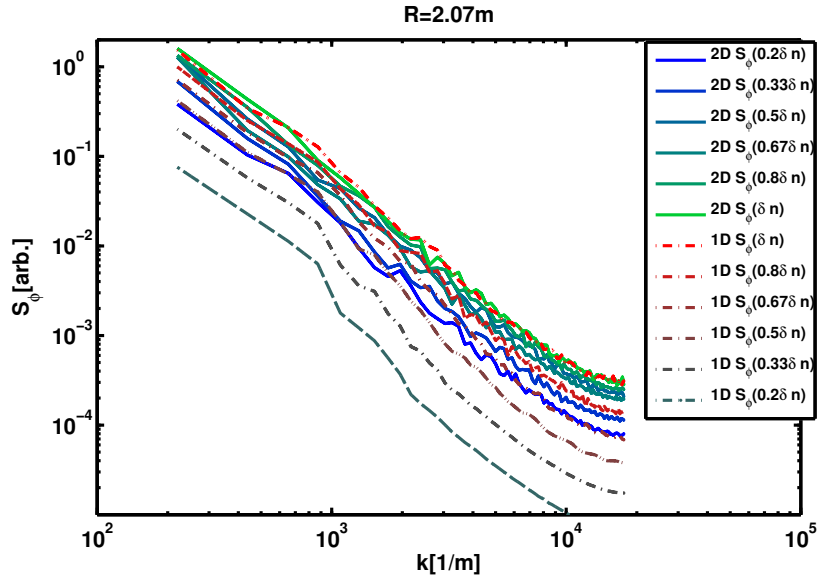


Figure 5.14: Phase variation power spectra obtained near $R=2.07m$ with different amplitude levels

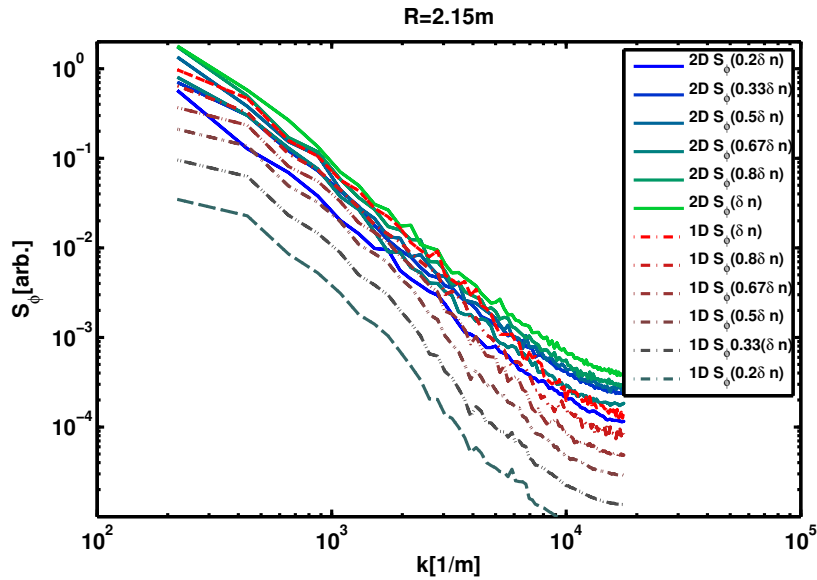


Figure 5.15: Phase variation power spectra obtained near $R=2.15m$ with different amplitude levels

amplitude variations spectra which were computed in 2D on figure 5.16. Because of energy conservation law it is impossible to obtain this amplitude variation in 1D with stationary solution code as 1D Helmholtz equation solver. The amplitude variation spectrum computed for a given amplitude level does not include any significant peak, it can be explained by much smaller ratio between the maximum turbulence level and the local (close to cut-off) turbulence level. Such turbulence amplitude profile cannot produce enough scattering from the plasma edge to be seen on the amplitude spectra.

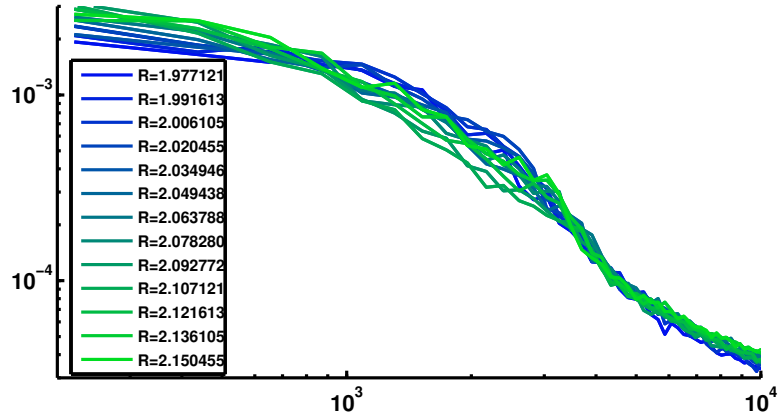


Figure 5.16: Amplitude variation spectra computed with IPF-FD3D code for various radial positions using a given turbulence

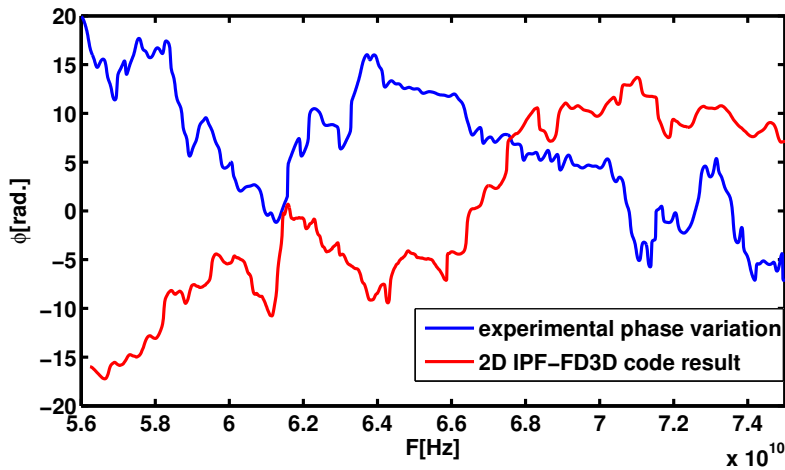


Figure 5.17: Phase variation computed with IPF-FD3D code (red) and experimental phase variation (red)

Experimental phase variations also suffer from phase runaway. Because of frequent signal amplitude losses, phase often jumps, and these jumps change the spectra. In such conditions it is often impossible to evaluate the phase variations spectrum properly. However phase variation from frequency sweep without efficient phase runaway can be visually compared with one of phase variations obtained using IPF-FD3D code (see figure 5.17). One can see that both signals behave very similarly.

5.2.2 Turbulence correlation length measurements

From USFR phase and amplitude variation spectra one can calculate the correlation lengths. To see the link between the correlation length of density perturbations and the correlation lengths of the amplitude and the phase variation, they were calculated

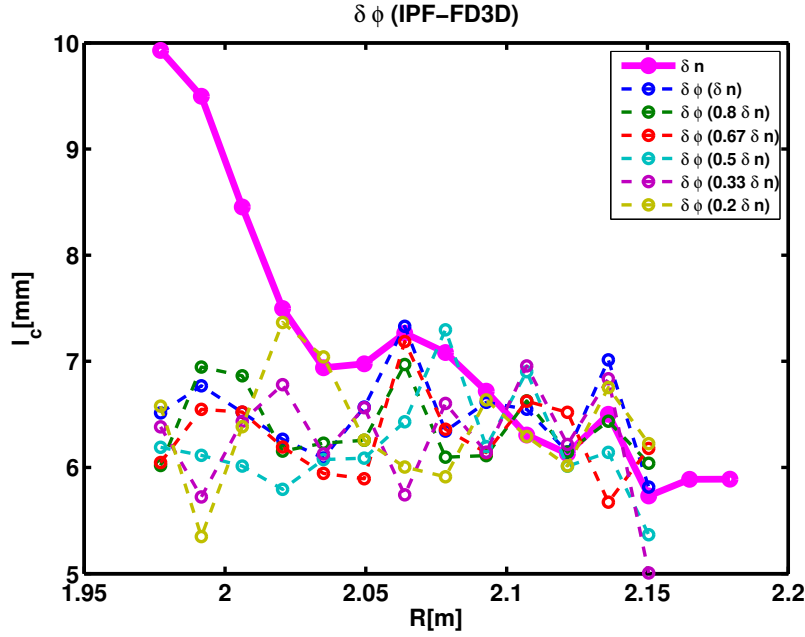


Figure 5.18: Magenta - turbulence correlation length l_c , Dashed lines phase variation correlation length computed with IPF-FD3D code with different turbulence levels

using 1D and 2D codes data.

To compute signal correlation length, first autocorrelation function was computed and correlation length was obtained as a full width of half amplitude of the correlation function.

As before will make calculations for different turbulence amplitudes. Figure 5.18 show the phase variation correlation length computed from results of 2D IPF-FD3D code. One can see that the phase correlation length does not change much with amplitude and probing position. It stays close to the edge turbulence correlation length value which is differ much with turbulence correlation length closer to the core. It can be connected to strong edge turbulence influence. It is an expected result taking into account that the phase fluctuation spectra does not differ much (see figures 5.13-5.15). The correlation length was also computed from 1D Helmholtz solver computation result. Because of smaller sensitivity to higher wave numbers one can expect overestimation of correlation length. Here due to limited analysed zone and finite statistics small wave-number values are not observed arr observed with small smaller amplitude. On figure 5.19 we can see that the phase fluctuation correlation length follows the change of the turbulence correlation length. Near $R = 2.1m$, where turbulence amplitude has a maximum phase variation, the correlation length computed for smaller turbulence level is smaller than the same value computed with higher turbulence level. However closer to the plasma core figure 5.19 shows opposite results. Overall in the vicinity of turbulence maximum, the phase variation correlation length

computed from 1D Helmholtz solver results is smaller than the turbulence one. On

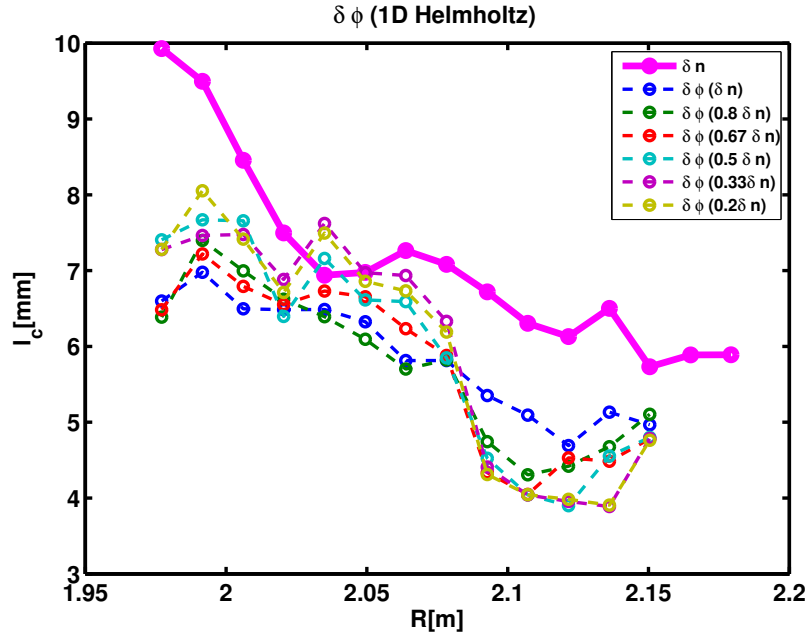


Figure 5.19: Magenta - turbulence correlation length l_c , Dashed lines amplitude variation correlation length computed with 1D Helmholtz equation solver with different turbulence levels

figure 5.20 one can find the reflectometer signal amplitude variation correlation length. A clear dependence on the density perturbation amplitude is seen. With increase of the turbulence level, the amplitude variation correlation length decreases. An unexpected radial behaviour was found, when turbulence correlation length increases in the direction to plasma core, amplitude variation correlation length decreases. The reason for this behaviour can be triggering of second unstable zone of Matieu equation which results in smaller wave number scattering that decrease correlation length.

It could be concluded that correlation length observation using UFSR signal demands some interpretation procedure. In past works theory was developed to process data from multi-channel fixed frequency reflectometry for correlation length calculations [100,101]. Different reflectometer sensitivity to different turbulence wave-number makes correlation length measurement not direct.

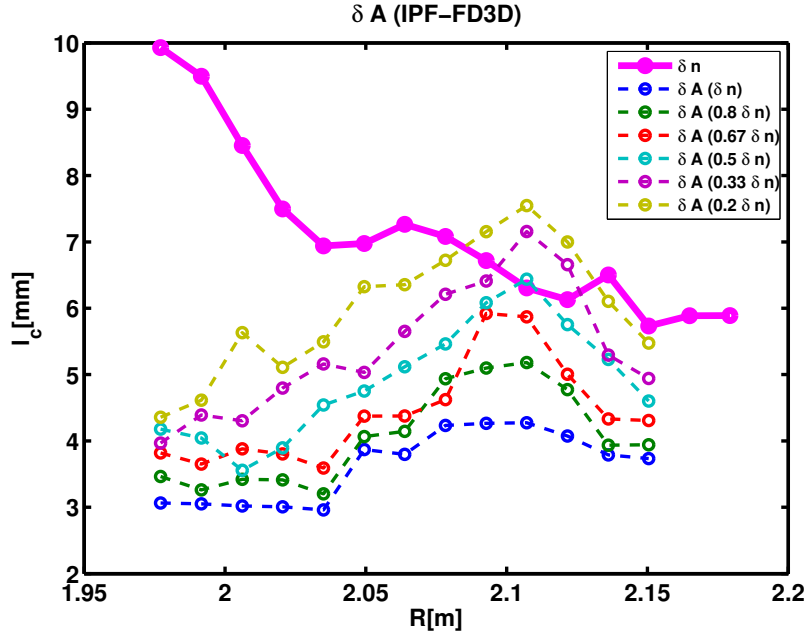


Figure 5.20: Magenta - turbulence correlation length l_c , Dashed lines signal amplitude variation correlation length computed with IPF-FD3D code with different turbulence levels

5.2.3 Conclusions and discussion

Resonance UFSR phase jumps can change the phase variation spectra and the density profile measurements and should be taken into account to calculate turbulence wavenumber spectrum with closed loop algorithms. Another change of phase variation spectra is caused by phase fluctuation gradient. This effect is connected to a slight change of the probing beam properties with frequency in the strong turbulence region. Taking into account all difficulties, phase variations samples inferred from simulations appear to be very similar to experimental phase variations.

Correlation lengths obtained using amplitude and phase variation for both 1D and 2D computations behave very differently. However all of them are the same order of magnitude than for turbulence data. Phase fluctuation correlation length computed using 1D Helmholtz equation solver behaviour is the closest to real l_c . Probably due to 2D effects IPF-FD3D code l_c computation results do not increase in the plasma core. It is clear that some more advanced processing has to be applied to reflectometer signal data.

Summary

*If any gentleman will say he
doubts the truth of this story, I
will fine him a gallon of brandy,
and make him drink it at one
draught!*

The surprising adventures of
Baron Munchausen.

Rudolf Erich Raspe

One of the crucial parameter for successful operation of MCF(Magnetic Confinement Fusion) machines is the energy confinement time. This time is mainly limited by particles and energy transport mechanisms, the good understanding of which is strongly connected to turbulence study. The validation of turbulence models relies on comparison with the experiment observations. Ultra-fast swept reflectometry is a good candidate for turbulence radial wave-number spectra measurements with good spatial and temporal resolutions.

The work carried out in the thesis deals with reflectometry interpretation for turbulence measurements by use of diagnostic modelling. A review of different simulation methods to reproduce reflectometer signal was done. Computations can be done with the help of 1,2 or 3 dimensional codes. In one dimension, using Helmholtz equation, it was shown both analytically and numerically that in the case of wave reflection before the main cut-off position resonance wave trapping can take place. In the presence of the noise, 1D steady state computations have shown that resonance does not disappear but becomes stronger. The fact that resonances can take place during reflectometry experiment both with fixed or sweeping frequency is very important because crossing resonance condition, a jump of the reflectometer signal phase can appear. Different computation techniques can interpret this phase jump differently, due to the wave behaviour in the trapping zone. If a frequency-sweep reflectometer is modelled using time dependent codes small amount of energy is transmitted in the resonance region.

However the wave reflection, in this case, can be seen with longer time of flight. Usually used filtering techniques are also able to change the resonant phase behaviour. In general phase jumps can be a source of very wide wave-number spectral noise. Another phase behaviour was detected in the presence of edge turbulence. Phase variation response in this case can contain a gradient effect. This is to say $\delta\phi_0 + k_g R$ where R is a radial position, $\delta\phi_0$ is the phase variation without the gradient effect, and k_g is a slope coefficient.

2D effects on reflectometry signal were investigated using the IPF-FD3D code. In the linear regime ($\delta(N^2) \propto \delta\phi$) the poloidal turbulence wave-number spectrum reduces the amplitude of phase variations as in this case signals from different poloidal lines mix-up together. However it almost does not affect wave-number spectra measurements. It was found that the poloidal curvature can partially cancel the effects of poloidal wave-number spectra, thus increasing the phase variations. This is due to the probing beam widening induced by the plasma density poloidal curvature, which leads to smaller number of rays received by the antenna. Not homogeneous 2D turbulence was generated using a set of different homogeneous turbulence maps with amplitude envelopes. In the case of inhomogeneous, isotropic, small level turbulence difference in phase wave-number spectral shapes were found between 1D and 2D computations.

Linear regime of the reflectometer signal behaviour is typical for turbulence parameters in the tokamak core region. However in the plasma edge vicinity one can usually find strong turbulence leading to non-linear behaviour of the reflectometer signals. Numerical computations have shown that when the probing beam crosses a turbulent layer it divides in two beams. One part stays unaffected by the turbulence and remains with the same phase and wave shape (coherent beam) whereas another part of the beam has a random phase due to the turbulence, and has its beam wave-front distorted and widened by turbulence poloidal wave-number (incoherent beam). The beam separation was studied by looking at the average beam power distribution and average field. The amplitude ratio between these 2 beams can be theoretically estimated with good accuracy using a simple WKB-based approach. Beside the dependence on turbulence amplitude the beam structure behind the turbulence layer depends also on the correlation length. Longer correlation length turbulences cause stronger coherent beam attenuation but lead to smaller incoherent beam widening. Shorter correlation length turbulences do not change much the probing beam and small amplitude incoherent beam spreads through a very wide angle. However turbulence with a very short correlation length can cause strong Bragg back-scattering which will change the reflectometry signal.

To shade some light on the edge turbulence influence on reflectometer core mea-

surements first O-mode computations were carried out in slab geometry and for a linear density profile. Turbulence in these computations was composed by 2 isotropic turbulence maps with different wave-number spectra. One of the maps together with Gaussian amplitude envelop was located in the edge region and another weak amplitude one was located everywhere. To study a challenging case for reflectometry interpretation, edge turbulence with long correlation length was chosen. In this scenario we were expecting to get more incoherent beam to be received by the antenna because of its high relative amplitude and small widening. Another reason to use long correlation length turbulence in the edge region is because it is then possible to have turbulence with only small wave-numbers and observe core turbulence high wave-numbers separately from the direct edge turbulence influence. Computations have shown that edge turbulence can affect the core measurements especially when its correlation length is smaller. Interaction between wave cut-off and edge turbulence can cause phase runaway and change the phase variation slope resulting in a wide additional spectrum. In the next step a more realistic Gaussian spectral shape turbulence was chosen. Computations have shown similar behaviour of the phase spectra with respect to previous computations. Additional information was obtained using amplitude variation spectra. Amplitude variations do not suffer from resonance phase jumps and contain more spectral information on the edge region turbulence. Turbulence amplitude peak in the edge region, according to Bragg scattering rule, is able to generate strong scattering which can be seen as a spectral peak near twice the local probing wave-number value. New technique was used to obtain experimental data. Poloidal reflectometry technique where receiving antennas are poloidally shifted from the emitting antenna was used with ultra-fast frequency-sweeping source. With the receiving antenna poloidal displacement this spectral peak can be observed slightly shifted to a smaller wave-number position. This is because in average scattering in the direction of shifted receiver antennas take place deeper in the edge amplitude envelope, corresponding to smaller probing wave-numbers.

To investigate the influence of the poloidal plasma curvature in the presence of edge turbulence swept reflectometry numerical simulation of core probing were done using the IPF-FD3D code. A typical 2D curved density profile of the Tore-Supra tokamak was taken as input data. Turbulence properties here were based on experimental observations. Varying the edge turbulence amplitude envelop it was found that the edge turbulence changes the plasma core reflectometry signal. Spectral peaks due to enhanced scattering signal amplitude variation were also observed. With the given turbulence parameters we do not see strong wave widening and the spectral peak displacement with the antenna shift might be connected to beam widening due to poloidal

plasma curvature.

The IPF-FD3D code was used as a synthetic diagnostic to calculate X-mode multichannel fixed-frequency reflectometer response with Gysela gyro-kinetic code simulation of Tore-Supra core turbulence. Given the turbulence time-step it was unfortunately impossible to track reflectometer phase variation, however it was possible to analyse the reflectometer signal amplitude. Using cross correlation between signals obtained from different radial positions, the signal amplitude correlation length was calculated. The result was compared with the turbulence correlation length, resulting in strong similarity in absolute values and general behaviours.

A next application of the X-mode UFSR synthetic diagnostic was done for ASDEX-Upgrade tokamak discharge number 31287. Turbulence parameters obtained by closed loop algorithm with 1D Helmholtz equation solver were used as input. Unlike the Tore-Supra tokamak ASDEX-Upgrade has non circular magnetic surfaces. Here to generate inhomogeneous turbulence, magnetic surfaces were approximated using Miller tokamak equilibrium approximation. This makes us able to create turbulence envelopes that follow the plasma geometry. IPF-FD3D code results were compared with 1D Helmholtz solver results. Both 2D and 1D computations have shown strong edge turbulence influence on the measured signal, which result in physical phase runaways. In such non-linear regimes USFR phase variation spectra computed with 1D and 2D codes were different. Phase variation amplitude computed using 1D code appeared to be more sensitive to turbulence amplitude changes. Correlation length was calculated from signal phase and amplitude from 2D computation and signal phase from 1D computation. It was found that correlation lengths computed with different methods behave differently. However all of the correlation length results are on the same order of magnitude.

Further work on UFSR data interpretation has to be done. Potentially the diagnostic can become a very good tool for turbulence wave-number spectra measurements. Strong edge turbulence which is usually present in the plasma edge vicinity drives the reflectometer response into the non-linear regime. In this case advanced signal filtering techniques should be developed and tested with time dependent 2D codes. To interpret the phase variation amplitude according to the turbulence level, additional information should be used as non-linear effects can change amplitudes and spectra of the phase variations. Each turbulence scenario has to be studied using full-wave codes to find the main dependencies and signatures, while analysing more data such as the signal amplitude, and using multi-antenna configurations.

Zusammenfassung

Ein entscheidender Erfolgsfaktor bei Operationen mit magnetischer Fusion ist die Energieeinschlusszeit. Hauptsächlich ist diese durch Teilchen- und Energietransportmechanismen beschränkt, was stark mit den von der Turbulenztheorie beschriebenen Prozessen verbunden ist. Die Verifizierung der Turbulenzmodelle basiert auf Vergleichen mit Experimentbeobachtungen. Die ultraschnell durchgestimmte Reflektometrie (USFR) ist ein guter Kandidat für die Messungen von turbulenten Radialwellenzahl-Spektren mit guter räumlichen und zeitlichen Auflösungen.

Diese Dissertation behandelt die Interpretation von Reflektometersignalen, die Turbulenzen messen, durch diagnostische Modellierung, wobei ein Überblick über verschiedene Simulationsmethoden gegeben wird, um das Reflektometersignal zu reproduzieren. Die Rechnung kann mithilfe ein-, zwei- und dreidimensionaler Codes vollzogen werden. In einer Dimension, unter Verwendung der Helmholtz-Gleichung, wurde sowohl analytisch als auch numerisch gezeigt, dass im Fall der Wellenreflexion vor der Haupt-Cutoff ein resonantes Wellen-Trapping stattfinden kann. Wenn das Dichteprofil gestört ist, haben 1D-Berechnungen im stationären Zustand gezeigt, dass die Resonanz nicht verschwindet, sondern stärker wird. Die Tatsache, dass Resonanzen während Reflektometriemessungen sowohl mit fester als auch variabler Frequenz auftreten können, ist sehr wichtig, da für die Resonanzbedingung ein Sprung der Reflektometersignalphase auftreten kann. Verschiedene Berechnungstechniken können diesen Phasensprung aufgrund des Wellenverhaltens in der Resonanzzone unterschiedlich sehen. Wenn ein Reflektometer mit Frequenzsweep unter Verwendung zeitabhängiger Codes modelliert wird, wird eine kleine Energiemenge in dem Resonanzbereich übertragen, was zu einer verzögerten Reflexion führt. Um Multireflexionen aus dem Signal zu entfernen, werden spezielle Filtertechniken verwendet. Sie können auch das Resonanzphasenverhalten ändern. Phasensprünge können eine Fehlerquelle bei der Bestimmung der Wellenlänge sein. Ein anderes Phasenverhalten wurde in Gegenwart von Dichteturbulenz am Plasmarand nachgewiesen. Die Phasenvariation kann in diesem Fall einen Gradienten enthalten. Dies bedeutet (Formel) wobei (Formel) eine radiale Position ist, (Formel) ist die Phasenvariation ohne den Gradienten (Formel) und (Formel) ist ein

Steigungskoeffizient.

2D-Effekte auf das Reflektometriesignal wurden unter Verwendung des IPF-FD3D-Codes untersucht. In dem linearen Bereich (Formel) reduziert das poloidale Turbulenzwellenzahlspektrum die Amplitude der Phasenvariationen, wie in diesem Fall Signale von verschiedenen poloidalen Wellenzahlen, die sich vermischen. Es beeinflusst jedoch fast nicht die Form des Phasenvariationsspektrums. Es wurde gezeigt, dass die poloidale Krümmung die Effekte des poloidalen Wellenzahlspektrums vermindert, durch die die Phasenvariationsstärke erhöht wird. Dies ist auf die Strahlverbreiterung zurückzuführen, die durch die poloidale Krümmung der Plasmadichte induziert wird, was zu einer geringeren Anzahl von der Antenne empfangenen Strahlen führt. Inhomogene 2D-Turbulenz wurde mit verschiedenen homogenen Turbulenzfeldern mit Amplitudenhüllkurven erzeugt. Im Fall von schwacher inhomogener, isotroper Turbulenz wurden Unterschiede in den spektralen Formen der Phasenwellenzahl zwischen 1D- und 2D-Berechnungen gefunden.

Der lineare Bereich des Reflektometer-Signalverhaltens ist typisch für Turbulenzparameter in der Tokamak-Kernregion. In der Nähe der Plasmaränder kann man jedoch eine starke Turbulenz finden, die zu einem nicht-linearen Verhalten der Reflektometersignale führt. Numerische Berechnungen haben gezeigt, dass wenn der Sondierungsstrahl eine turbulente Schicht kreuzt, er sich in zwei Strahlen teilt. Ein Teil bleibt von der Turbulenz unberührt und bleibt bei gleicher Phasen- und Wellenform (kohärenter Strahl). Während ein anderer Teil des Strahls aufgrund der Turbulenz eine zufällige Phase aufweist und seine Strahlwellenfront durch die poloidale Wellenzahl der Turbulenz verzerrt und aufgeweitet wird (inkohärenter Strahl). Die Strahlteilung wurde untersucht, indem die durchschnittliche Strahlleistungsverteilung und das durchschnittliche Feld betrachtet wurden. Das Amplitudenverhältnis zwischen diesen beiden Strahlen kann theoretisch mit guter Genauigkeit unter Verwendung eines einfachen WKB-basierten Ansatzes geschätzt werden. Neben der Abhängigkeit von der Turbulenzamplitude hängt die Strahlstruktur hinter der Turbulenzschicht auch von der Korrelationslänge der Turbulenz ab. Längere Korrelationslängen führen zu einer stärkeren Dämpfung des kohärenten Strahls, führen jedoch zu einer kleineren Erweiterung des inkohärenten Strahls. Kürzere Korrelationslängen ändern den Sondierungsstrahl nicht viel und inkohärente Strahlen mit kleiner Amplitude breiten sich über einen sehr großen Winkel aus. Turbulenz mit einer sehr kurzen Korrelationslänge kann jedoch eine starke Bragg-Rückstreuung verursachen, die das Reflektometriesignal ändert.

Um etwas Licht auf den Randturbulenzeinfluss auf Reflektometermessungen der Kernregion zu werfen, wurden erste O-Mod-Berechnungen in der Quadergeometrie und für ein lineares Dichteprofil durchgeführt. Die Turbulenz in diesen Berechnun-

gen wurde durch zwei isotrope Turbulenzfelder mit verschiedenen Wellenzahlspektren zusammengesetzt. Um das extremste Szenario zu reproduzieren, wurde eine lange Korrelationslänge der Randturbulenz gewählt. In diesem Szenario erwarteten wir, dass aufgrund ihrer hohen relativen Amplitude und kleinen Verbreiterung ein inkohärenterer Strahl von der Antenne empfangen wird. Ein weiterer Grund, Turbulenz mit langer Korrelationslänge im Randbereich zu verwenden, besteht darin, dass es dann möglich ist, Turbulenzen nur mit kleinen Wellenzahlen zu haben und Kernturbulenz mit hohen Wellenzahlen getrennt von dem direkten Randturbulenzeinfluss zu beobachten. Berechnungen haben gezeigt, dass Randturbulenzen die Kernmessungen beeinflussen können, insbesondere wenn ihre Korrelationslänge länger ist. Eine kurze Korrelationslänge der Randturbulenz kann jedoch eine starke Bragg-Rückstreuung erzeugen. Die Wechselwirkung zwischen der Hauptreflexion am Cutoff und der Randturbulenz kann zu einem Durchgehen der Phase führen und die Phasenvariationssteigung ändern, was zu einem breiten zusätzlichen Spektrum führt. Die Wechselwirkung zwischen Wellenhauptreflexion und Randturbulenz kann Phasensprünge verursachen und die Steigung der Phasenvariation ändern, was zu einem breiten zusätzlichen Spektrum führt. Im nächsten Schritt wurde eine realistischere Gaußsche Spektralform der Turbulenz gewählt. Berechnungen haben ein ähnliches Verhalten der Phasenspektren in Bezug auf frühere Berechnungen gezeigt. Zusätzliche Information wurde unter Verwendung von Spektren der Amplitudenvariation erhalten. Amplitudenschwankungen leiden nicht unter Resonanzphasensprüngen und enthalten mehr spektrale Information über die Turbulenz der Randregion. Die Spitze der Turbulenzamplitude im Randbereich kann gemäß der Bragg-Streuungsregel eine starke Streuung erzeugen, die als eine spektrale Spitze in der Nähe des Doppelten des Wertes der lokalen Abtastwellenzahl gesehen werden kann. Eine neue Technik wurde verwendet, um experimentelle Daten zu erhalten. Eine poloidale Reflektometrietechnik, bei der Empfangsantennen von der Sendeantenne aus poloidal verschoben sind, wurde mit einer ultraschnellen Frequenzabtastungsquelle verwendet. Mit der poloidalen Verschiebung der Empfangsantenne kann diese spektrale Spitze leicht verschoben zu einer Position mit einer kleineren Wellenzahl beobachtet werden. Dies liegt daran, dass die Streuung in der Richtung von verschobenen Empfangsantennen tiefer in der Randamplitudenhüllkurve stattfindet, was kleineren Abtastwellenzahlen entspricht. Um den Einfluss der poloidalen Plasmakrümmung in Anwesenheit von Randturbulenz auf die Reflektometrie zu untersuchen, wurde eine numerische Simulation der Kernuntersuchung unter Verwendung des IPF-FD3D-Codes durchgeführt. Ein typisches gekrümmtes 2D-Dichteprofil des Tore-Supra Tokamak wurde als Eingabe genommen. Die Turbulenzeigenschaften basierten hier auf experimentellen Beobachtungen. Durch Variieren der Randturbulenzamplitudenhüllkurve wurde gefunden, dass

die Randturbulenz das Plasmakernreflektometriesignal verändert. Spektrale Spitzen in der Signalamplitudenvariation aufgrund der verstärkten Streuung von der Kante wurden ebenfalls beobachtet. Bei den gegebenen Turbulenzparametern sehen wir keine starke Wellenverbreiterung und die spektrale Peakverschiebung mit der Antennenverschiebung könnte mit der Strahlaufweitung aufgrund der poloidalen Plasmakrümmung verbunden sein.

Der IPF-FD3D-Code wurde als eine synthetische Diagnostik verwendet, um die Antwort eines Mehrkanal-Festfrequenz-Reflektometers in X-Mode-Polarisation mit einer gyrokinetischen Turbulenzsimulation (GYSELA) der Tore-Supra-Tokamak-Kernturbulenz zu berechnen. Mit dem gegebenen Turbulenz-Zeit-Schritt war es leider unmöglich, die Reflektometer-Phasenvariation zu verfolgen, jedoch war es möglich, die Signalamplitude des Reflektometers zu analysieren. Unter Verwendung der Kreuzkorrelation zwischen Signalen, die von verschiedenen radialen Positionen erhalten wurden, wurde die Signalamplitudenkorrelationslänge berechnet. Das Ergebnis wurde mit der Turbulenzkorrelationslänge verglichen, was zu einer starken Ähnlichkeit der absoluten Werte und allgemeinen Verhaltensweisen führte. Eine nächste Anwendung der synthetischen X-Mode-UFSR-Diagnose wurde für die Tokamak-Schussnummer 31287 von ASDEX-Upgrade durchgeführt. Die Turbulenzparameter, die durch einen Regelkreisalgorithmus mit 1D-Helmholtz-Gleichungslöser erhalten wurden, wurden als Eingabe verwendet. Anders als der Tore-Supra Tokamak hat ASDEX-Upgrade nicht-kreisförmige magnetische Oberflächen. Um hier inhomogene Turbulenzen zu erzeugen, wurden magnetische Oberflächen approximiert, indem eine Miller-Tokamak-Gleichgewichtsnäherung verwendet wurde. Dies ermöglicht uns, Turbulenzhüllkurven zu erzeugen, die der Plasmageometrie folgen. IPF-FD3D-Code-Ergebnisse wurden mit 1D Helmholtz-Löser-Ergebnissen verglichen. Sowohl 2D- als auch 1D-Berechnungen haben starke Randturbulenzeinflüsse auf das gemessene Signal gezeigt, die zu physikalischen Phasensprüngen führen. In solchen nichtlinearen Regimes waren UFSR-Phasenvariationsspektren, die mit 1D- und 2D-Codes berechnet wurden, unterschiedlich. Die unter Verwendung von 1D-Code berechnete Phasenvariationsamplitude schien gegenüber Turbulenzamplitudenänderungen empfindlicher zu sein. Die Korrelationslänge wurde aus der Signalphase und der Amplitude aus der 2D-Berechnung und der Signalphase aus der 1D-Berechnung berechnet. Es wurde festgestellt, dass Korrelationslängen, die mit unterschiedlichen Methoden berechnet wurden, sich unterschiedlich verhalten. Alle Korrelationslängenergebnisse liegen jedoch in der gleichen Größenordnung.

Weitere Arbeiten zur UFSR-Dateninterpretation müssen durchgeführt werden. Potentiell kann die Diagnose zu einem sehr guten Werkzeug für Messungen von Turbulenzwellenzahlspektren werden. Starke Randturbulenzen, die üblicherweise in der Nähe

der Plasmaränder vorhanden sind, treiben die Reflektometerantwort in den nichtlinearen Bereich. In diesem Fall sollten hochentwickelte Signalfiltertechniken mit zeitabhängigen 2D-Codes entwickelt und getestet werden. Um die Phasenvariationsamplitude gemäß dem Turbulenzniveau zu interpretieren, sollte zusätzliche Information verwendet werden, da nichtlineare Effekte Amplituden und Spektren der Phasenvariationen ändern können. Jedes Turbulenzszenario muss unter Verwendung von Vollwellencodes untersucht werden, um die Hauptabhängigkeiten und Signaturen zu finden, während mehr Daten wie die Signalamplitude analysiert werden. Wenn möglich, können auch poloidale Reflektometrie-Konfigurationen mit mehreren Antennen verwendet werden.

Bibliography

- [1] "BP Statistical Review of World Energy", Review paper, 66th edition (www.bp.com, BP Statistical Review of World Energy, London, England, June 2017)
- [2] F. Wagner, "Electricity generation by intermittent sources", EPJ Web of Conferences **98**, 04006 (2015)
- [3] C. Moné et al., "2014 Cost of Wind Energy Review" Technical Report: NREL/TP-6A20-64281 October 2015 at National Laboratory of the U.S. Department of Energy (Lakewood, USA, 2015)
- [4] J. Twidell and T. Weir, "Renewable energy sources" (Routledge, Abingdon, England, 2015)
- [5] M. Melaina, "Wind Energy Biography: A Review of Wind Turbine Technology and Economics" Report: University of Michigan: Ann Arbor: 1-46. (Ann Arbor, USA, 2004)
- [6] "Air quality guidelines for Europe", Second edition. Chapter 7.1, European series, No. 91 (WHO regional publications, Geneva, Switzerland, 2000)
- [7] R. J. Norby and Y. Luo, New Phytologist **162**, 281 (2004)
- [8] F. Wagner, "Integration of variable electricity sources", (Slides from EPS-SIF energy summer school 21 - 26 July 2017 - VILLA MONASTERO - VARENNA, LAKE COMO, Italy)
<https://www.sif.it/media/1a64e083.pdf>
(entered on 12,06,2018)
- [9] R. Bryce, "Maintaining the Advantage: Why the U.S. Should Not Follow the EU's Energy Policies" Energy Policy and Environment, report: Center for energy policy and the environment at the Manhattan Institute (New York, USA, February 4, 2014)

- [10] J. Wesson, D. J. Campbell, "Tokamaks" 3d edition (Clarendon Press, Oxford, England, 2004)
- [11] F. F. Chen, "Introduction to Plasma Physics and Controlled Fusion" Volume 1, 2d edition (Plenum Press, New York, USA, 1984)
- [12] J. Ongena and G. Van Oost, "Energy For Future Centuries. Will Fusion Be An Inexhaustible, Safe And Clean Energy Source?" Fusion Science and Technology **45** 3 (2004)
<https://doi.org/10.13182/FST04-A464>
- [13] S. Brunner, "Waves and Instabilities in Inhomogeneous Plasmas", 3d circle course at Centre de Recherches en Physique des Plasmas, Association Euratom-Confédération Suisse, Ecole Polytechnique Fédérale de Lausanne, Switzerland,
<https://crppwww.epfl.ch/brunner/inhomoplasma.pdf>
 (entered 01.06.2018)
- [14] M. Wakatani, "Stellarator and Heliotron Devices" (Oxford University Press, Oxford, England, 1998)
- [15] M. Keilhacker and ASDEX Team, Nuclear Fusion **25**, 1045 (1985)
- [16] N. Bretz, Review of Scientific Instruments **68**, 2927 (1997)
- [17] D. W. Ross, Comments Plasma Phys. Control. Fusion **XII**, 155 (1989)
- [18] W. Horton, Rev. Mod. Phys. **71**, 735 (1999)
- [19] W. Horton, Nuclear Fusion **55**, 113021 (2015)
- [20] B. B. Kodomtsev and O. P. Pogutze, "Theory of electron transport in a strong magnetic field", JETP Lett. **39**, 269 (1984)
- [21] D. R. Thayer and P. H. Diamond, "Thermally driven convective cells and tokamak edge turbulence", Physics of Fluids **30**, 3724 (1987)
- [22] A. Н. Колмогоров, доклад академии наук СССР **32**, 16, (1941),
 A. N. Kolmogorov, USSR Academy of science report **32**, 16, (Moscow, USSR, 1941)
 (reprinted in Proc. R. Soc. Lond. A434 15 1991)
- [23] R. H. Kraichnan, Physics of Fluids **10**, 1417 (1967)
- [24] B. Coppi et al., Physics of Fluids **10**, 582 (1967)
- [25] S. C. Cowley et al., Physics of Fluids **B3**, 2767 (1991)

- [26] J. F. Drake, P. N. Guzdar and A. B. Hassam, Phys. Rev. Lett., **61**, 2205, (1988)
- [27] B. B. Kadomtsev and O. P. Pogutse, Plasma instability due to particle trapping in a toroidal geometry . Soviet Physics JETP, **24**, 1172, (1967)
- [28] R.R. Dominguez, Nuclear Fusion **31**, 747 (1991)
- [29] W. M. Tang, J. C. Adam and David W. Ross, Physics of Fluids, **20**, 430, (1977)
- [30] M. Tagger, G. Laval and R. Pellat, Nuclear Fusion, **17**, 109, (1977)
- [31] G.T. Hoang et al., Nuclear Fusion, **38**, 117 (1998)
- [32] N. Bonanomi et al., Nuclear Fusion **55**, 113016 (2015)
- [33] Li. Yandong et al., "Multi-scale turbulence experiment in HT-7 tokamak" 6 IFTS workshop slides, september 25-26 (Hangzhon, China, 2007)
<http://slideplayer.com/slide/9423416/>
 (entered 19.06.2018)
- [34] Grégoire Hornung, "Study of plasma turbulence by ultrafast sweeping reflectometry on the Tore Supra tokamak", Ph.D thesis, Aix-Marseille Université (Marseille, France, 2013)
- [35] N. Winsor et al., Physics of Fluids **11**, 2448 (1968)
- [36] A. V. Melnikov, Nature Physics **12**, 386–390 (2016)
- [37] C.P. Ritz et al., Nuclear Fusion **27**, 1125 (1987)
- [38] A. R. Field et al., Review of Scientific Instruments **83**, 013508 (2012)
- [39] ITER official website: www.iter.org
- [40] E.J. Doyle et al., "Reflectometry application to ITER, Diagnostics for Experimental Thermonuclear Fusion Reactors", 117-132 (Plenum Press, New York, USA, 1996)
- [41] C. Fanack, "Etude analytique et numérique de la réflectométrie dans un plasma fluctuant. Modeles á une et deux dimensions", Ph.D thesis (in French), Université Henri Poincaré, Nancy I (Nancy, France, 1997).
- [42] M. Colin, "Modélisation d'un réflectomètre mode X en vue de caractériser les fluctuations de densité et de champ magnétique : applications aux signaux de Tore Supra", PhD thesis (in French), Université Henri Poincaré, Nancy I (Nancy, France, 2001)

- [43] E. Mathieu, "Mémoire sur Le Mouvement Vibratoire d'une Membrane de forme Elliptique". Journal de Mathématiques Pures et Appliquées (in French), **13**, 137–203. (1868)
- [44] Reza N. Jazar et al., J. Braz. Soc. Mech. Sci. and Eng. **30** (2008)
- [45] D. Frenkel and R. Portugal, J. Phys. A: Math. Gen. **34**, 3541 (2001)
- [46] V. Udintsev et al, presentation for 1st Int. Conference on Frontiers in Diagnostic Technologies (Frascati, Italy, 25-27.11.2009)
<http://slideplayer.com/slide/10679612/>
 (entered on 12,06,2018)
- [47] E. Mazzucato, Review of Scientific Instruments, **69**, 2201 2 (1998)
- [48] Nazikian R, Kramer G J and Valeo E., Physics of Plasmas, **8**, 1840 (2001)
- [49] H. Bottollier-Curtet, Review of Scientific Instruments **58**, 539 (1987)
- [50] R. B. Morales et al., Review of Scientific Instruments **88**, 043503 (2017)
- [51] A. E. Costley et al., Review of Scientific Instruments **61**, 2823 (1990)
- [52] A. Silva et al., Review of Scientific Instruments **67**, 4138. (1996)
- [53] G. R. Hanson et al., Review of Scientific Instruments **63**, 4658 (1992)
- [54] V. Vershkov et al., Soviet Physics-Technical Physics (English Translation), **32**, 523 (1987)
- [55] R. Sabot et al., Review of Scientific Instruments **75**, 2656 (2004)
- [56] A. Medvedeva, "Experimental study of turbulence at the plasma edge of ASDEX Upgrade tokamak with an ultra-fast swept reflectometer", Ph.D thesis, Technische Universität München (Munich, Germany, 2017)
- [57] G Hornung et al., Plasma Phys. Control. Fusion, **55**, 125013 (11pp) (2013)
- [58] M E Manso et al., Plasma Phys. Control. Fusion, **43**, A73 (2001)
- [59] Y. Roh, C. W. Domier, and N. C. Luhmann Jr., Review of Scientific Instruments **72**, 332 (2001)
- [60] Bruce I. Cohen, Thomas B. Kaiser, and John C. Garrison, Review of Scientific Instruments **68**, 477 (1997)

- [61] H. Arnichand et al., Nuclear Fusion **54**, 123017 (2014)
- [62] E Z Gusakov et al., Plasma Phys. Control. Fusion **57**, 075009 (2015)
- [63] Holzhauser E. et al., Plasma Phys. Control. Fusion **40**, 1869 (1998)
- [64] M. Hirsch et al., Plasma Phys. Control. Fusion **43**, 1641 (2001)
- [65] C. Lechte et al. Plasma Phys. Control. Fusion **59** 075006 (2017)
- [66] D. Prisiazhniuk, "Development and application of poloidal correlation reflectometry to study turbulent structures in the ASDEX Upgrade tokamak" Ph.D thesis, TECHNISCHE UNIVERSITÄT MÜNCHEN (Munich, Germany, 2017)
- [67] A. Krämer-Flecken et al., Review of Scientific Instruments **81**, 113502 (2010)
- [68] E. Mazzucato et al., Physics of Plasmas **9**, 1955 (2002)
- [69] S. Zhongbing et al., Review of Scientific Instruments **85**, 11D816 (2014)
- [70] C. Fanack et al. Plasma Phys. and Control. Fusion **38**, 1915 (1996)
- [71] T. Gerbaud et al., "Density fluctuation measurements with fast-sweep X-mode reflectometry", IRW8 (St. Petersburg, Russia, 2007)
http://www.ioffe.ru/HTPPL/irw8/proceedings/Gerbaud_paper.pdf
 (entered 12.06,2018)
- [72] F. da Silva et al., J. Comp Phys **295**, 24 (2015)
- [73] V.V.Bulanin, A.V.Petrov, M.V.Yefanov, "Consideration Doppler reflectometry in Born approximation", IRW7 (Garching, Germany, 2005)
<http://www.aug.ipp.mpg.de/IRW/IRW7/papers/Bulanin-paper.pdf>
 (entered 12.06.2018)
- [74] М. А. Ирзак, Диссертация на соискание ученой степени кандидата физико-математических наук (Санкт-Петербург, Россия, 1997),
 M. Irzak, Dissertation for the degree of candidate of physical and mathematical sciences (St. Petersburg, Russia, 1997)
- [75] F. Clairet et al., Review of Scientific Instruments **82**, 083502 (2011)
- [76] F. Briolle, R. Lima and R. V. Mendes, Meas. Sci. Technol. **20**, 105502 (2009)
- [77] S. Heuraux et al., IEEE Transactions on plasma science, **38**, (2010)

- [78] Victorita Dolean, Pierre Jolivet, Frédéric Nataf, "An Introduction to Domain Decomposition Methods: algorithms, theory and parallel implementation" (Master, Paris, France, 2015)
<https://hal.archives-ouvertes.fr/cel-01100932v5>
 (entred 17.06.2018)
- [79] A. Medvedeva et al., "Density fluctuations measurements with an Ultra-Fast-Swept Reflectometer in ASDEX Upgrade" IRW12 (Jülich, Germany, 2015)
http://www.fz-juelich.de/SharedDocs/Downloads/CONFERENCES/IRW12/EN/MondayMorning_05_paper.pdf
 (entered 12.06.2018)
- [80] A. D. Piliya A. Yu. Popov, Plasma Phys. Control. Fusion **44**, 467 (2002)
- [81] L. Landau and E. Lifshitz, "Electromagnetic of Continuous Media" Volume 8 of A Course of Theoretical Physics (Pergamon Press, Oxford, England, 1960)
- [82] E. Holzhauser and J. H. Massig, Plasma Physics **20**, 867 (1978)
- [83] E Z Gusakov and A Yu Popov, Plasma Phys. Control. Fusion **44**, 2327 (2002)
- [84] E.V. Sysoeva et al., Nuclear Fusion **55** 033016 (2015)
- [85] V.I. Taranskiy et al., "Wave propagation in the turbulent atmosphere" (Nauka, Moscow, USSR, 1967)
- [86] E. Z. Gusakov and A. V. Surkov, Plasma Physics Reports **28** 827 (2002)
- [87] Gusakov E Z et al., Plasma Phys. Control. Fusion **57** 075009 (2015)
- [88] E. Gusakov et al., Plasma Phys. Control. Fusion **51** 065018 (2009)
- [89] D. Prisiazhniuk et al., Plasma Phys. Control. Fusion **59** 025013 (2017)
- [90] A. Krämer-Flecken et al., New J. Phys. **17** 073007 (2015)
- [91] T. Windisch et al., Plasma Phys. Control. Fusion **59** 105002 (2017)
- [92] P. Simon et al., Plasma Phys. Control. Fusion **58**, 045029 (2016)
- [93] H. Arnichand et al., Nuclear Fusion **54** 123017 (2014)
- [94] F. Clairet et al., "Plasma turbulence measured by fast sweep reflectometry on TORE SUPRA", 12th International Congress on Plasma Physics, 25-29 October (Nice, France, 2004)

<https://hal.archives-ouvertes.fr/hal-00003132>

(entred 17.06.2018)

- [95] V. Grandgirard et al., J. Comput. Phys. **217**, 395 (2006)
- [96] V. Grandgirard et al., Communications in nonlinear science and numerical simulation **13**, 81 (2008)
- [97] F. Clairet et al., Review of Scientific Instruments **81**, 10D903 (2010)
- [98] M. Schubert et al., "Full-wave test of analytical theory for fixed frequency fluctuation reflectometry", IRW9 (Lisbon, Portugal, 2009)
www.ipfn.tecnico.ulisboa.pt/irw9/abstracts/mschubert_abstract.pdf
(entered 17.06.2018)
- [99] R. L. Miller et al., Physics of Plasmas **5**, 973 (1998)
- [100] N. Teplova (Kosolapova) et al., Phys. Scr. **87** 045502 (2013)
- [101] G. Leclert et al., Plasma Phys. Control. Fusion **48** 1389 (2006)
- [102] T. Gerbaud et al., Review of Scientific Instruments **77** 10E928 (2006)
- [103] H. Arnichand, "Identification of trapped electron modes in frequency fluctuation spectra of fusion plasmas", PhD thesis, Aix-Marseille Université (Marseille, France, 2015)

Acknowledgements

These 3 and half years which I spent on my Ph.D. dissertation were very interesting and productive. I have learned a lot and grown in many ways. I want to thank people who helped me during this time and were supporting me along the way. First I want to thank Prof. Stephane Heuraux who directed and organized my work, solved all administrative issues which were completed by double degree between University of Lorraine and University of Stuttgart, and by co-financement from Cadarache. He showed me the world of reflectometry helped me with numerical tools has improved my knowledge during many hours of discussions.

I want to thank Prof. Günter Tovar for guiding and accelerating administrative process in University of Stuttgart. Also I want to thank Prof. Thomas Hirth for supervising me during first part of my work.

I am thankful to Dr. Carsten Lecte letting me to use his code, helping with computations and for technical support, Dr Sebastien Hacquin for his scientific advices and intensive editing of my poor English texts. Dr. Roland Sabot with who I had many discussions being in Cadarache and Dr. W. Kasperek who was leading meetings in Stuttgart University. I wish to thank Dr. Frederic Clairet for giving me his reflectometry interpretation results for JET tokamak.

This work would be not completed without my visit to IPP Garching. I am thankful to Dr. Garrard D. Conway who agreed my visit and gave me the possibility to work with ASDEX-U data, Dr. Anna Medvedeva who helped me with data extraction and shared her results for comparisons. I want to thank Dr. Dmitrii Prisiazhniuk for number of very useful discussions that has answered many of my questions.

Particularly I want to thanks Prof. E. Z. Gusakov for very important discussion related to theoretical models and data analysis. Also I want to thank Dr. Mikhail Irzak for useful mail exchange which allowed me to use reciprocity theorem.

Very big computations performed in this work would be impossible without help of bwUniCluster in Baden-Württemberg.

I wish to acknowledge the support and help of my friends: Mr. Dr. Jordan Cavalier, Artur Vander Sande, Dr. Antom Bogomolov, Dr. Rennan Marales. Jordan Ledig,

Homam Betar, Julien Médina, Oleg Krutkin, Liza Sytova, Richard Deutsch, Anton Kyyanytsa, Dr. Georgiy Kichin, Krishnan Srinivasarengan and others. If I forgot somebody it doesn't mean I don't appreciate your help, it is just my "good" memory.

I want to thanks members of the music bands where I was playing. These people helped me to mix my scientific work with some art and make it more interesting and productive. Dr. Yusuf Bhujwalla, Masha Usoltceva, Valentin Pascu, Aaron Ho, Marcella Tizo, Michal Kuczynski, Wojciech Trl and a cover band from Cadarache.

I want to thank my wife Vitalina for giving me the Daughter and supporting me all the time. My daughter Olivia which was my ray of light in the final part of the Ph.D.

In the end I want to thank my parents which always were always supporting my interest in physics and mathematics. Thanks you, you made me to be who I am.

Appendix A

Isotropic turbulence generation

Using inverse fast Fourier transform it is very easy to generate 1D turbulence. To create 2D isotropic turbulence with a given 1D spectrum the same way, first 2D spectral map should be created. Usually by turbulence spectrum people mean spectra of 1D turbulence from one line from 2D turbulence map. This spectrum corresponded to projection of 2D spectral map to the given direction taking into account phase of each mode. This results in spectral traces from each mode towards smaller wave-numbers.

to find 2D spectral map which results into given 1D spectrum special algorithm was used. Algorithm has 3 steps:

Using expression $S_1 = S_{given}^{1D} \cdot S_0 / S_0^{1D}$, first approximation of the spectrum is computed.

Where S_1 is the first approximation of the spectrum, $S_0 = S_{given}$

Second step: spectral traces increase slope of the spectrum. Here we will adjust the slope multiplying our function by k^n .

Third step: When the slope is adjusted final spectrum is generated as $S_n = S_{given}^{1D} \cdot S_{n-1} / S_{n-1}^{1D}$.

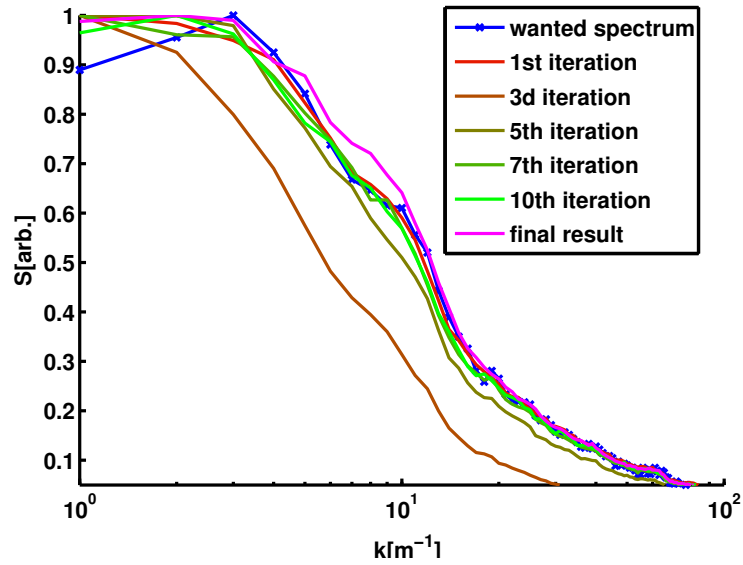


Figure A.1: Example of iterative algorithm to find isotropic spectrum central cut that will match wanted projection (1D spectrum)

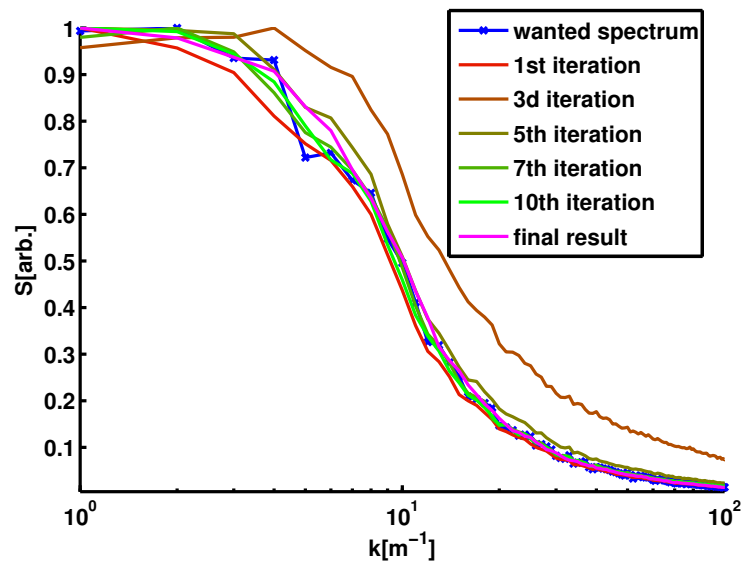


Figure A.2: Example of iterative algorithm to find isotropic spectrum central cut that will match wanted projection (1D spectrum)

Example of the matlab code:

```
1 %spectrum correction
2 function S=spec_corr_isotr(Swant)
3 %input test data
4 %k=linspace(1,3000,3000);
5 %Swant=k.^(-log(2));
6
7 %end of input test data
8 Swant=Swant/max(Swant);
9 k=linspace(1,numel(Swant),numel(Swant));
10 [kx,ky]=meshgrid(k,k);
11 ka=sqrt(kx.^2+ky.^2);
12 nit=10;
13
14 S2d=zeros(size(ka));
15 parfor i=1:size(ka,1)
16     S2d(i,:) = interp1(k',Swant',ka(i,:), 'linear');
17 end
18 S2d(isnan(S2d))=0.0;
19
20 parfor i=1:1000
21     Shb(i,:)=abs(sum(S2d.*exp(1i*2*pi*rand(size(S2d)))));
22 end
23
24 Sh=mean(Shb);Sh=Sh/max(Sh);
25
26 F1=Sh./Swant;%This is transfer function for 1st order shape of
    the spectrum
27
28 % now we will change slope of this transfer function
29
30 smin=-2;
31 smax=2;
32
33 figure('name','iteration')
34 hold on
35 loglog(k,Swant,'color',[0 0 1])
```

```

36
37 for i=1:nit
38     snew=(smax+smin) / 2.;
39
40     Fnew=F1.*(k.^(snew));
41     if (snew==0)
42         Fnew=F1;
43     end
44     Snew=Swant./Fnew;
45     Snew(~isfinite(Snew))=0.;
46     Snew=Snew/max(Snew);
47
48     parfor i=1:size(ka,1)
49         S2d(i,:) = interp1(k',Snew',ka(i,:), 'linear');
50     end
51     S2d(isnan(S2d))=0.0;
52     parfor i=1:1000
53         Shbnew(i,:)=abs(sum(S2d.*exp(1i*2*pi*rand(size(S2d)))));
54     end
55     Shnew=mean(Shbnew); Shnew=Shnew/max(Shnew(1:floor(numel(
        Shnew)/2.)));
56
57     if (mean(Swant(1:floor(numel(Shnew)/2.))-Shnew(1:floor(
        numel(Shnew)/2.)))>0.)
58         smax=snew;
59     else
60         smin=snew;
61     end
62     smin
63     smax
64     loglog(k,Shnew, 'color',[(1-0.1*i) (0+0.1*i) 0])
65 end
66 T=Snew./Shnew;
67 T(isnan(T))=0.;
68 Snew=Swant.*T;
69

```

```

70 %last iteration to make good input spectrum
71
72
73 S=smooth(Snew);
74 Snew=S;
75
76     parfor i=1:size(ka,1)
77         S2d(i,:) = interp1(k',Snew',ka(i,:), 'linear');
78     end
79     S2d(isnan(S2d))=0.0;
80     parfor i=1:1000
81         Shbnew(i,:)=abs(sum(S2d.*exp(1i*2*pi*rand(size(S2d))))
82             );
83     end
84     Shnew=mean(Shbnew);Shnew=Shnew/max(Shnew(1:floor(numel(
85         Shnew)/2.)));
86
87     loglog(k,Shnew, 'color',[1-0.1*i (0+0.1*i) 0], 'LineWidth',8)
88
89 end

```


Appendix B

Miller equilibrium for shaped turbulence

To generate 2D turbulence which will follow the shape of tokamak magnetic surfaces with elongated and triangular shape Miller magnetic surface approximation [99] can be used.

$$R(\rho_M, \theta_M) = R_{SH}(\rho_M) + r(\rho_M) \cos(\theta_M + \kappa_M \sin(\theta_M)) \quad (\text{B.1})$$

$$Z(\rho_M, \theta_M) = l_M r(\rho_M) \sin(\theta_M) \quad (\text{B.2})$$

In this formulation we are using 2 coordinate system of magnetic surface index coordinate ρ_M which is usually given as normalized poloidal magnetic flux, and related to the poloidal angle coordinate θ_M . Tokamak magnetic surfaces can be fitted using 4 functions: small radius r , triangularity κ_M , elongation l_M , and Shafranov shift R_{SH} . Conventional poloidal angle can be expressed as $\theta = \arctan(Z/(R - R_{SH}))$.

Inhomogeneous, isotropic turbulence which follows magnetic surfaces shape can be made using mix of homogeneous turbulence maps with amplitude envelopes shaped using Miller equilibrium.

$$\delta n = RMS(\delta n) \sum_i A_i \delta n_i \quad (\text{B.3})$$

Where A_i are merging amplitude envelopes. Depending on if we are interested in measure of High of Low field side, magnetic surface coordinate ρ_M have to be divided on areas corresponding certain radial positions. For this areas merging turbulence amplitude envelopes can be created as function of $r h o_M$ and then converted to R, Z coordinate space.

Example of magnetic surfaces reproduced using Miller approximation for ASDEX-upgrade tokamak discharge is illustrated in figure B.1

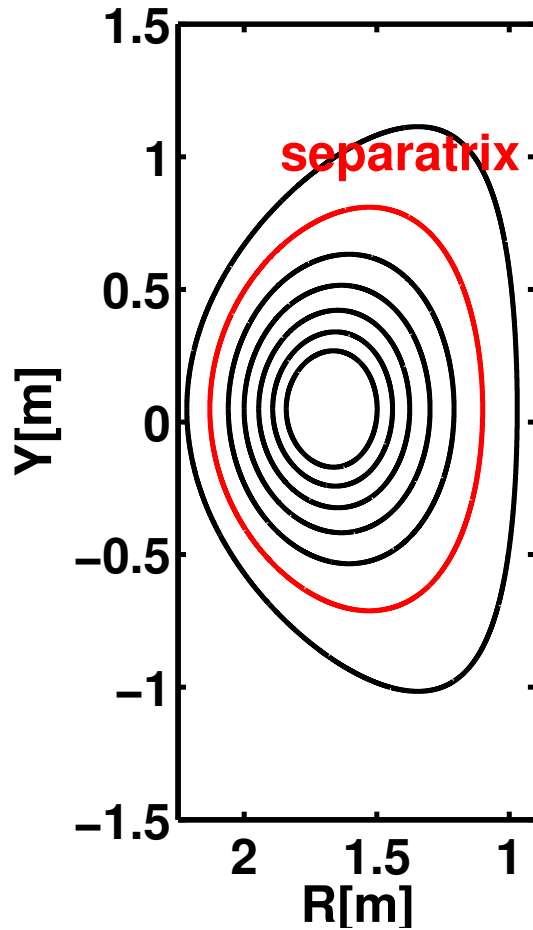


Figure B.1: ASDEX-Upgrade magnetic surfaces approximated with

Matlab function to generate isotropic turbulence following Miller equilibrium:

```

1 function [dnfull ,RI ,ZI ,window2D ,Ampg, dn]=isomillerturb(a ,Amp,r
   ,x ,R0 ,k ,Z0 ,S ,kr ,Rg ,Zg ,Rw)
2     %vars for test
   _____
3
4     phi=linspace(0 ,2*pi ,floor(numel(r)*2*pi));
5     window=zeros(numel(Rw) ,numel(r));
6     window2D=zeros(size(S,1) ,numel(r) ,numel(phi));
7     dn3Dap=zeros(size(S,1) ,numel(r) ,numel(phi));
8
9     %create grid
10    RI=zeros(numel(r) ,numel(phi));
11    ZI=zeros(numel(r) ,numel(phi));
12

```

```

13     parfor i=1:numel(r)
14         RI(i,:) = R0(i) + r(i) .* cos(phi + x(i) .* sin(phi));
15         ZI(i,:) = Z0 + k(i) .* r(i) .* sin(phi);
16     end
17
18     rfit = fit(RI(:,1), a', 'linearinterp'); %fit surface index to
19     R
20     aw = rfit(Rw); %find surface index of the window position
21     %create window which will be bended after
22     lt = [zeros(1,50) (1/2. + tanh(linspace(-pi, pi, 200))/tanh(pi)
23           /2.) ones(1,100) (1/2. + tanh(linspace(pi, -pi, 200))/tanh(
24           pi)/2.) zeros(1,50)];
25     %do first window
26     window(1,:) = interp1q(linspace(aw(1), aw(2), 300)', lt
27       (301:600)', a');
28     window(1, isnan(window(1,:))) = 0.;
29     window(1, 1:find(window(1,:) > 0., 1, 'first')) = 1;
30     %do all others
31     for i=2:(numel(Rw))
32         if (i==numel(Rw))
33             ll = [linspace(aw(i-1), aw(i) - (aw(i)-aw(i-1))
34               /299.5/2, 300) linspace(aw(i) + (a(numel(a))-aw(i))
35               /299.5/2, a(numel(a)), 300)];
36         else
37             ll = [linspace(aw(i-1), aw(i) - (aw(i)-aw(i-1))
38               /299.5/2, 300) linspace(aw(i) + (aw(i+1)-aw(i))
39               /299.5/2, aw(i+1), 300)];
40         end
41         window(i,:) = interp1q(ll', lt', a');
42         window(i, isnan(window(i,:))) = 0.;
43     end
44
45     %there is an error accomulated from interpolation. lets
46     make sum(window)=1
47     %probably do not need this error is lower then one %
48     %and put AMP here
49     Amp2D = Amp' * ones(1, numel(phi));

```

```

41 window2D=zeros(numel(Rw),numel(a),numel(phi));
42
43 parfor i=1:numel(Rw)
44     window2D(i, :, :)=window(i, :)'*ones(1,numel(phi));
45 end
46 %create grid meash
47 [Rgg,Zgg]=meshgrid(Rg,Zg);
48 %interpolate windows on cartesian greed
49 wing=zeros(numel(Rw),numel(Zg),numel(Rg));
50 dn=zeros(numel(Rw),numel(Zg),numel(Rg));
51 parfor i=1:(numel(Rw))
52     wing(i, :, :)=griddata(RI,ZI,squeeze(window2D(i, :, :)),
53         Rgg,Zgg,'linear');
54     dn(i, :, :)=turbgen_isotropic(kr,S(i, :),Rg,Zg);
55 end
56 Ampg=griddata(RI,ZI,Amp2D,Rgg,Zgg,'linear');
57 Ampg(isnan(Ampg))=0;
58 %when windows and turb are ready we start to do
59 dn(isnan(dn))=0.;
60 wing(isnan(wing))=0.;
61 dnfull=squeeze(sum(wing.*dn)).*Ampg;
62 end

```

Appendix C

Edge turbulence influence on the reflectometer phase

It was observed that during core turbulence observation with USFR in presence of strong edge turbulence reflectometer phase suffer phase jumps due to resonant multi-reflections and phase gradient. In this section we will have a look how these phenomena affect phase variation spectra.

Phase jumps: When wave trapping appear during USFR measurements can introduce phase jump of π . These phase jumps mathematically can be express as Heaviside functions. Spectra of these functions can be expressed analytically.

$$FFT(H(R)) = \frac{1}{2}(\frac{1}{\pi ik} + \delta(k)) \quad (C.1)$$

Here δ is the delta function. To evaluate influence on the total phase variation spectra let us consider arbitrary reflectometer phase variation with introduced phase jumps.

Phase gradient: During USFR core observation with the strong edge turbulence can introduce additional phase $\phi_G(F) = k_{PHI}F$. Analytically spectra of such expression can be found:

$$FFT(phi_G) = (\delta\phi)_{max}exp(i\omega t)[\frac{t}{i\omega} + \frac{1}{\omega^2}] \quad (C.2)$$

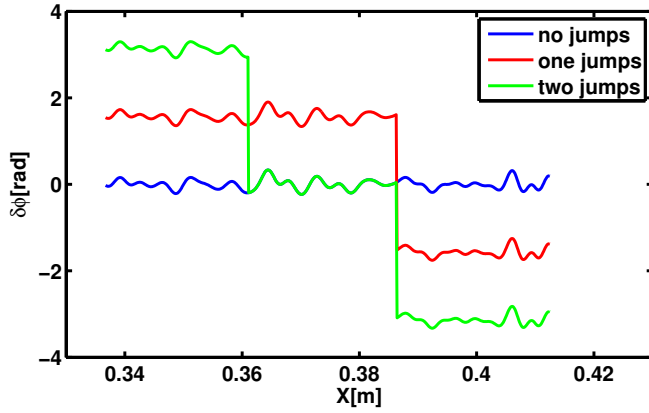


Figure C.1: left: Phase variation without phase jumps (blue), phase variation with one phase jump (red), phase variation with two phase jumps (green)

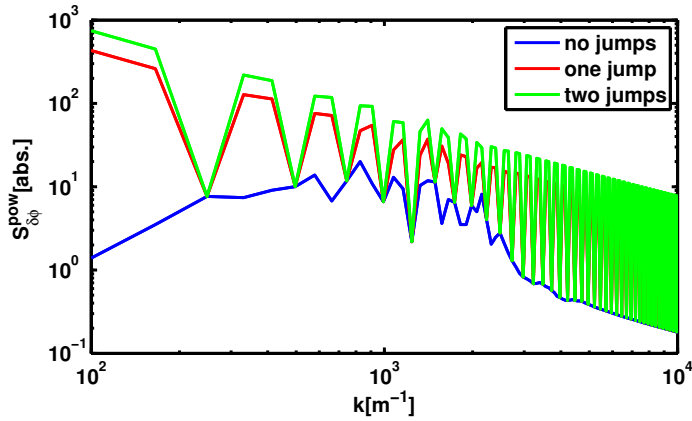


Figure C.2: left: Phase variation spectrum without phase jumps (blue), phase variation spectrum with one phase jump (red), phase variation spectrum with two phase jumps (green)

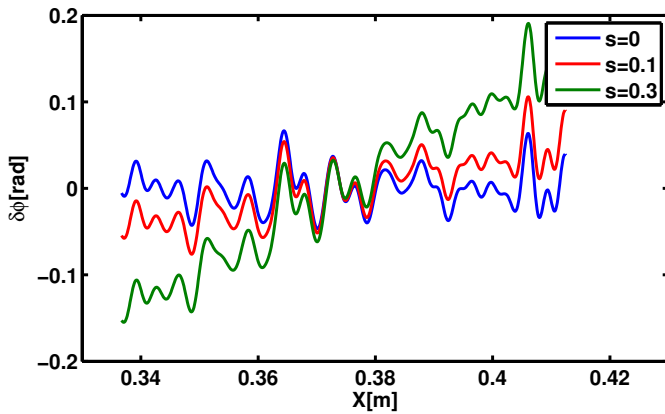


Figure C.3: left: Phase variation without phase gradient (blue), phase variation with gradient $(\delta\phi)_{max} = 0.1$ (red), phase variation with phase gradient $(\delta\phi)_{max} = 0.3$ (green)

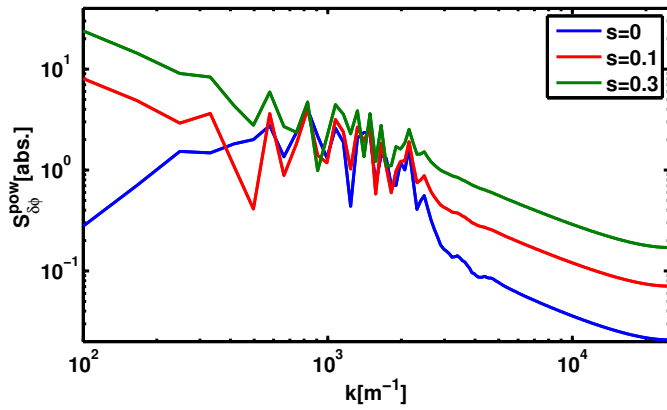


Figure C.4: left: Phase variation spectrum without phase gradient (blue), phase variation spectrum with gradient $(\delta\phi)_{max} = 0.1$ (red), phase variation spectrum with phase gradient $(\delta\phi)_{max} = 0.3$ (green)